AERODYNAMIC PERFORMANCE OF THE INBOARD ELEVON ON A BLENDED-WING-BODY AIRCRAFT

by

Alexander Gordon Jackson,
Bachelor of Engineering Aerospace, Ryerson University, 2001

A thesis

presented to Ryerson University

in partial fulfillment of the
requirement for the degree of
Master of Applied Science
in the Program of
Mechanical Engineering

PROPERTY OF
RYERSON UNIVERSITY LIBRARY

Toronto, Ontario, Canada, 2004
©Alexander Gordon Jackson, 2004

UMI Number: EC53411

INFORMATION TO USERS

The quality of this reproduction is dependent upon the quality of the copy submitted. Broken or indistinct print, colored or poor quality illustrations and photographs, print bleed-through, substandard margins, and improper alignment can adversely affect reproduction.

In the unlikely event that the author did not send a complete manuscript and there are missing pages, these will be noted. Also, if unauthorized copyright material had to be removed, a note will indicate the deletion.

UMI®

UMI Microform EC53411
Copyright 2009 by ProQuest LLC
All rights reserved. This microform edition is protected against unauthorized copying under Title 17, United States Code.

ProQuest LLC
789 East Eisenhower Parkway
P.O. Box 1346
Ann Arbor, MI 48106-1346

Proprietary Information

The research contained in this thesis was conducted in collaboration with Boeing Phantom Works, and as a result, contains proprietary information. Therefore, as a result, certain figures, and tables have been removed from the text for publication. They are as follows:

Figures: 2.1, 2.2, 3.9, 3.10, 3.11, 3.12, 3.13, 3.14

Tables: 5.2, 5.5, 5.6, 5.7, 5.11

Authors Declaration

I herby declare that I am the sole author of this thesis.

I authorize Ryerson University to lend this thesis to other institutions or individuals for the purpose of scholarly research.

Alexander Jackson — September 28 2004
Date

I further authorize Ryerson University to reproduce this thesis by photocopying or by other means, in total or in part, at the request of other institutions or individuals for the purpose of scholarly research.

Alexander Jackson — September 28 2004
Date

Borrower's Page

Ryerson University requires the signatures of all persons using or photocopying this thesis. Please sign below, and give address and date.

Name	Address	Date
Name	Address	Date
Name	Address	Date
Name	Address	Date
Name	Address	Date
Name	Address	Date
Name	Address	Date
Name	Address	Date
Name	Address	Date
Name	Address	Date

Abstract

Alexander Jackson

Masters of Applied Science in Mechanical Engineering

Ryerson University

September 27, 2004

Aerodynamic Performance Of The Inboard Elevon On A Blended-Wing-Body Aircraft

The objectives of this research are to examine the effects of trailing edge modifications of the inboard elevon of a blended-wing-body (BWB) aircraft, the goal being to try and reduce the hinge moment of the inboard elevon through selective aerodynamic design. A computational model was built for 60° and 70° beveled trailing edge modifications, as well as no modification. The inboard elevon was deflected positive 5° and negative 5°. The numerical solutions were obtained using an implicit solver and inviscid model. The results of this research showed that, through the use of a beveled trailing edge on the inboard elevon, a maximum of 112% reduction in the hinge moment could be achieved for the negative deflection case and a maximum of 88% reduction in the hinge moment for the positive deflection case. The results showed that there was a significant improvement in the hinge moments, with less than a 2% average change in the overall aerodynamic performance of the BWB for the inviscid models.

Acknowledgments

The author would like to thank Dr. Paul Walsh for all of his help during this research period, and for allowing the author to work on such a leading edge project. Also a thank you to Dino Roman of Boeing Phantom Works for allowing Ryerson University to continue the research in this subject. Thank you to Gerald Donaldson of Ryerson University and Hartmut Schmider of Queens University for their assistance with the computational resources. Finally, thank you to the technical support team and customer service team at Pointwise for all of their help during this work.

Dedication

I would like to dedicate this work to my parents and my fiancée, whose support has been unwavering during this research.

Table of Contents

List of Figures

List of Tables

Abbreviations

Abbreviation	*Description*
2D	Two Dimensional
3D	Three Dimensional
AFM	Advancing Front Method
ALM	Advancing Layer Method
AR	Aspect Ratio
BC	Boundary Condition
BCF	Background Control Function
BWB	Blended Wing Body
CAD	Computer Aided Design
CFD	Computational Fluid Dynamics
CG	Center of Gravity
CV	Control Volume
FCF	Foreground Control Function
GUI	Graphical User Interface
HPCVL	High Performance Computing Virtual Laboratory
IGES	Initial Graphics Exchange Specification
L/D	Lift to Drag Ratio
M	Mach Number
MByte	Megabyte
MTOW	Maximum Takeoff Weight
NASA	National Aeronautics and Space Administration
OEW	Operating Empty Weight
PDE	Partial Differential Equation
RAM	Random Access Memory
RANS	Reynolds Averaged Navier-Stokes Equations
S-A	Spalart-Allmaras
TANH	Hyperbolic Tangent
TFI	Transfinite Interpolation

Roman Symbols

Symbol	*Description*
A	Area
$\mathbf{a}$	Arbitrary Vector
C_L	Lift Coefficient
C_D	Drag Coefficient
C_M	Pitching Moment Coefficient
C_H	Hinge Moment Coefficient
D	Drag
E	Energy
f	Function
h	Enthalpy
$\overline{k}$	Turbulent Kinetic Energy
k_{eff}	Effective Conductivity
l	Length
L	Lift
M	Moment
N	Node
$\mathbf{n}$	Normal Unit Vector
p	Pressure
R	Gas Constant
S	Source Terms
S_h	Heat Due to Chemical Reactions
S_{ref}	Wing Reference Area
S_{wet}	Wetted Surface Area
T	Temperature
t	Time
u_T	Friction Velocity
V	Volume

x, y, z	Cartesian Co-ordinate system
u, v, w	Cartesian Velocity Components
y^+	Non-dimensional distance used in turbulent flow
y	Distance from wall to node

Greek Symbols

Symbol	*Description*
α	Angle of Attack/Under-Relaxation Parameter
τ	Shear Stress
τ_{ij}	Viscous Stress Tensor
θ	Angle
ρ	Density
μ	Viscosity
ϕ	Scalar Quantity
δ	Displacement
γ	Ratio of Specific Heats
κ	Von Kármán Constant
Γ	Diffusion Coefficient
∇	Gradient
Δ	Delta
ξ, η	Transformed Coordinates

Subscripts

Subscript	*Description*
∞	Freestream Values
eff	Effective
H	Hinge
i, j	Node indices

i, j, k	Tensor Notation
ref	Reference
T	Turbulence
w	Wall

Superscripts

Superscript	*Description*
‘	Fluctuating Component
n	Variable at Time t
o	Angular Degree

Overbars

Overbar	*Description*
–	Mean Component
→	Vector
=	Double Averaged

Chapter 1

Introduction

1.1 Revolution and Evolution

In 1903 the Wright Brothers made the first powered flight in the Wright Flyer, see figure 1.1. The 12 second flight marked mankind's venture into powered flight. Almost 5 decades later in 1947 the B-47 took flight, see figure 1.1. Comparing the two aircraft, there is a revolution in aircraft design. From the wood and fabric covered wings and open air cockpit of the Wright Flyer to the aluminum swept wings and pressurized cabin of the B-47, the design of aircraft had come a long way since that first powered flight. Another 5 decades and much hasn't changed in the design of aircraft. Compare the modern Boeing 777 (B777), see figure1.1, to the B-47 and there isn't as stark a change as the Wright flyer compared to the B-47. After the B-47, aircraft design had become an evolutionary process rather than revolutionary. The basic layout of an aircraft was set with the B-47, tubular fuselage, swept wings, empennage, and cockpit at the front. Of course, there have been major changes between the B-47 and the B777 but the basic layout hasn't changed.

Although the basic design of commercial transport has not changed, in practice, development has been ongoing into revolutionary design ideas, such as the Concorde, Tupolev Tu-144 and the new Boeing Sonic Cruiser design. In 1982 Northrop put into practice the advantages of a blended wing body (BWB) design with their B-2 stealth bomber, see figure 1.2. Even earlier blended wing concepts took flight in the form of the German AW-52 Horten, see below figure 1.3, in 1949 and the Northrop YB-49 in 1948, shown below in figure 1.3.

1903-Wright Flyer

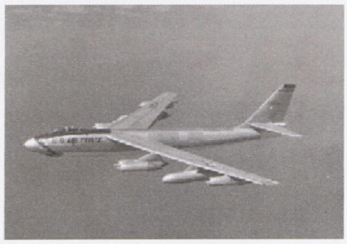

1947-Boeing B-47

1998-Boeing 777

Figure 1.1 Evolution of flight over the last 10 decades. [1, 2, 3]

Figure 1.2 Northrop B-2 Spirit. [4]

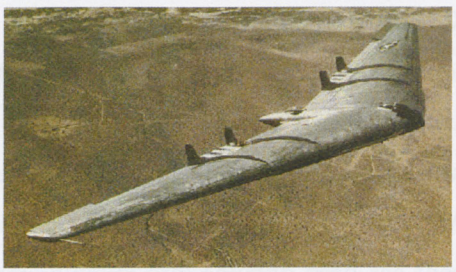

Figure 1.3 German AW-52 Horton, and Northrop YB-49. [5, 6]

In 1988, Dennis Bushnell of NASA Langley posed the question: "Is there a renaissance for the long-haul transport?"[7]. A preliminary design study was conducted by McDonnell Douglas to evaluate different configurations. The results of this work showed that by blending the wing into the fuselage, pictured in figure 1.4, the possibility of improved aerodynamic performance could be realized.

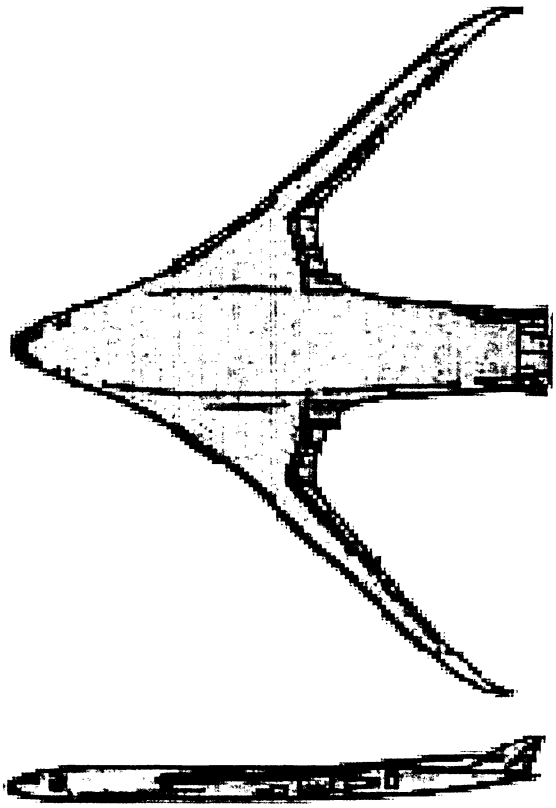

Figure 1.4 Initial design study results. [7]

The initial design study performed by McDonnell Douglas showed marked improvement in aircraft weight, lift to drag ratio and fuel burn with the BWB aircraft. Based on these improvements NASA Langley funded a study at McDonnell Douglas to develop the commercial use of the BWB configuration for a design mission of 800 passengers, a 7000 nautical mile range, and at a cruise Mach number of 0.85. The genesis of the BWB configuration and the resulting improvement in aerodynamic efficiency will be outlined next.

The genesis of the BWB begins with the selection of a fuselage shape for both the BWB and conventional aircraft. In figure 1.5 three potential fuselage shapes each of which can hold 800 passengers are shown. The sphere has minimum surface area; however, it is not a streamlined shape, which leaves the standard tubular fuselage and disc fuselage. Next, in figure 1.6, wings of equivalent 15,000 ft^2 surface areas are added to the tubular fuselage and disc fuselage. Due to the shape of the disk fuselage, a portion of the wing is masked, reducing the wetted surface area by 7000 ft^2. The wetted surface area of an aircraft is the surface area of an aircraft exposed to the airflow. The wetted surface area is used to compute the skin friction drag of an aircraft and therefore, by reducing this value, a designer can improve the aerodynamic efficiency of an aircraft.

In figures 1.7 and 1.8, engines and the required control surfaces are added to both configurations, and a further reduction in the total wetted area is realized in the BWB, resulting in a total difference of 14,300 ft², a reduction in total wetted area of 33%.

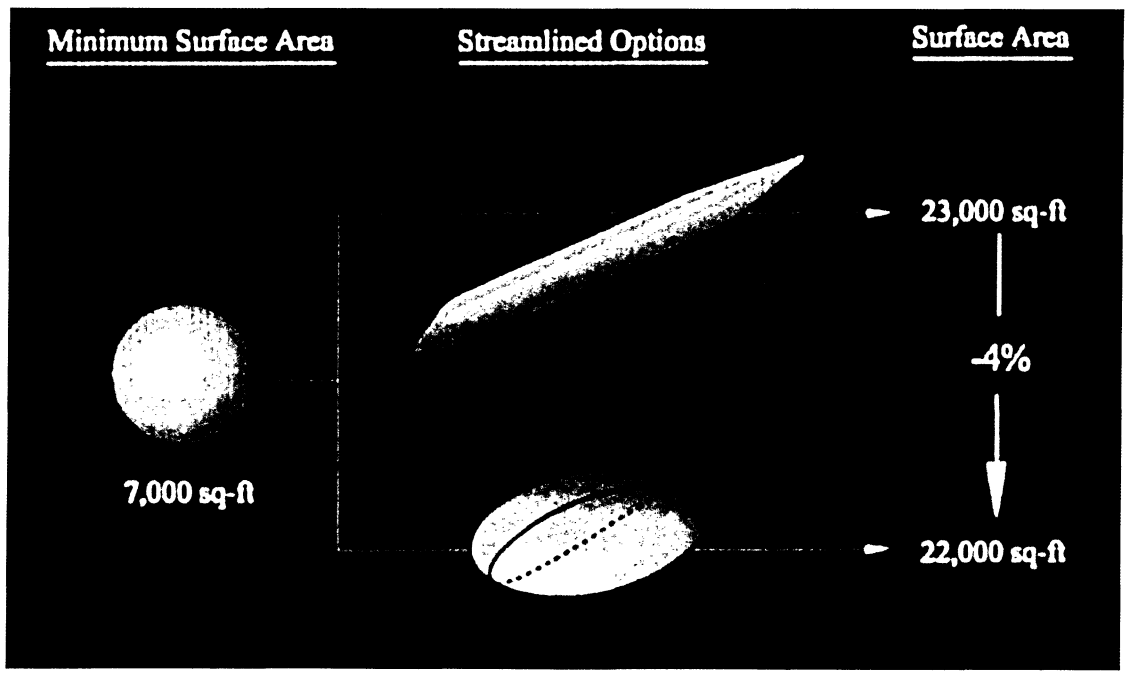

Figure 1.5 Fuselage geometry and its effects on surface area. [7]

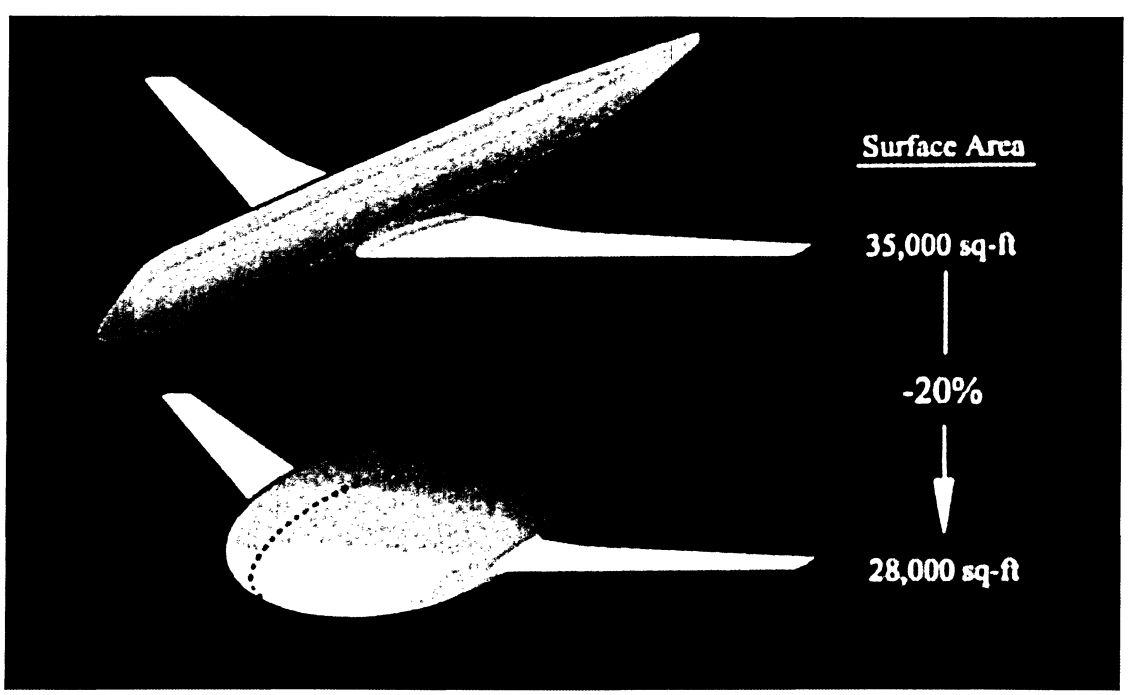

Figure 1.6 Addition of wings and its effects on surface area. [7]

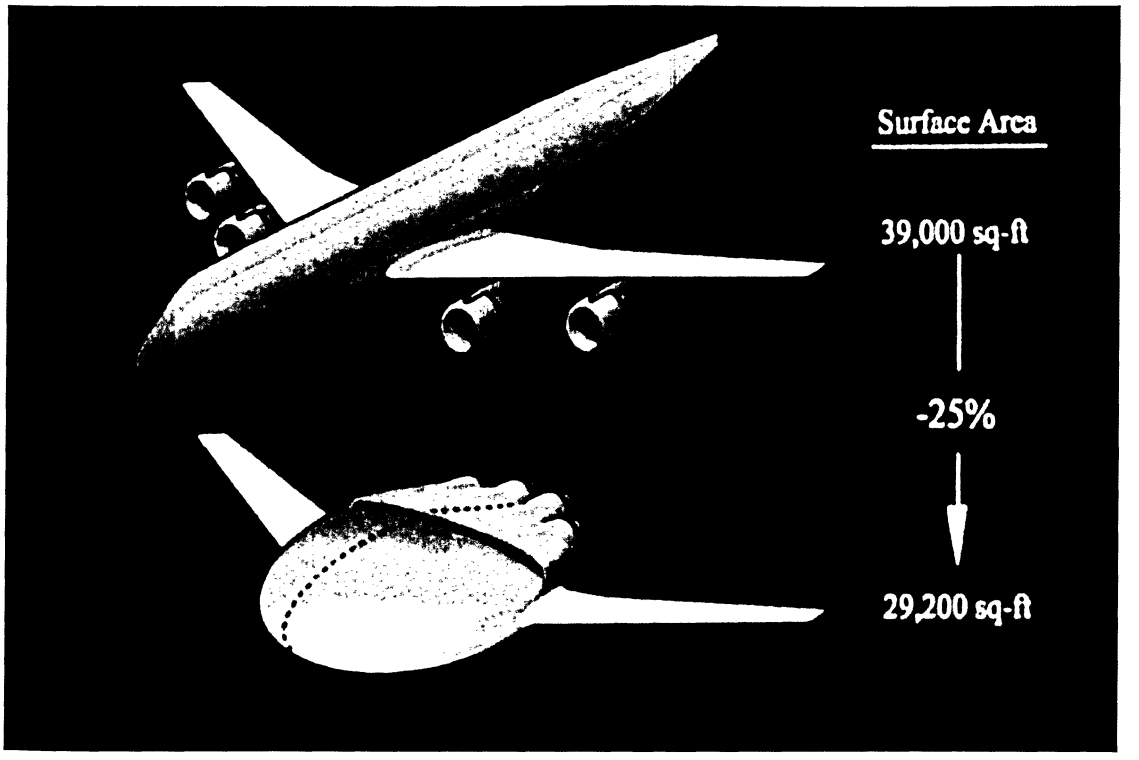

Figure 1.7 Effects of the addition of engines on surface area. [7]

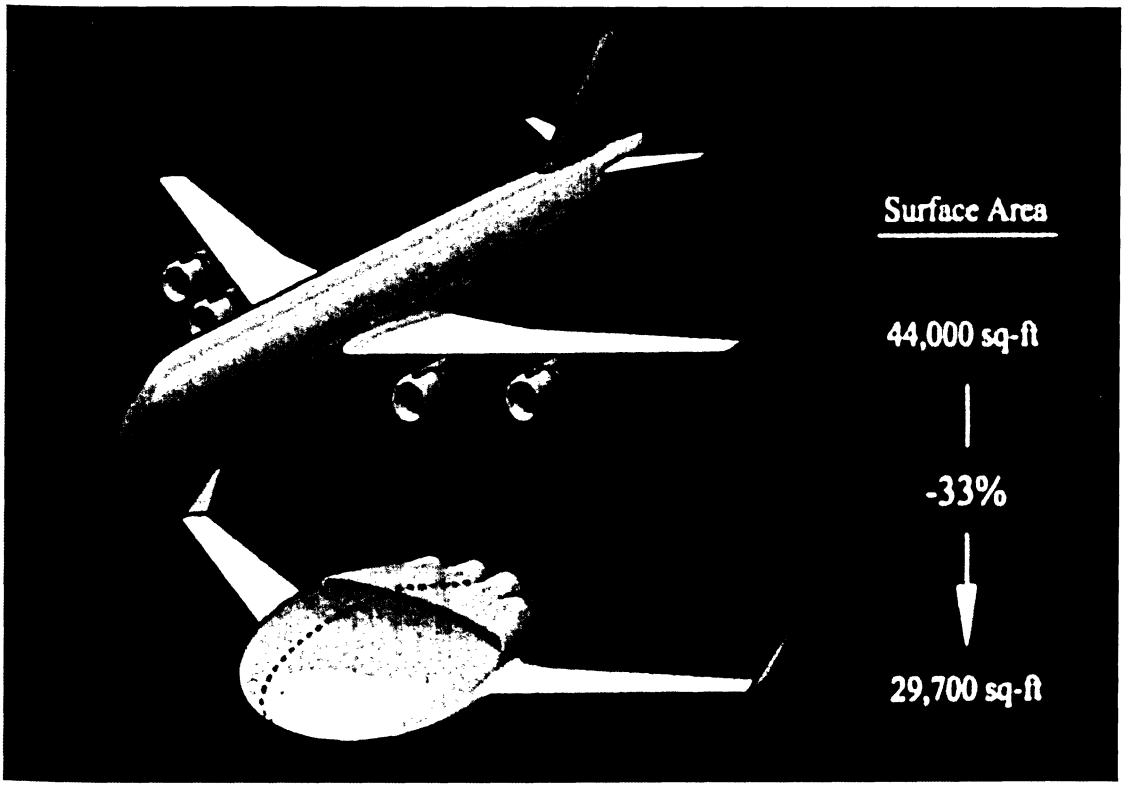

Figure 1.8 Effects of the addition of control surfaces on surface area. [7]

Figure 1.9 shows a plot of statistical data measuring aircraft lift to drag ratio and their respective wetted-aspect-ratio.

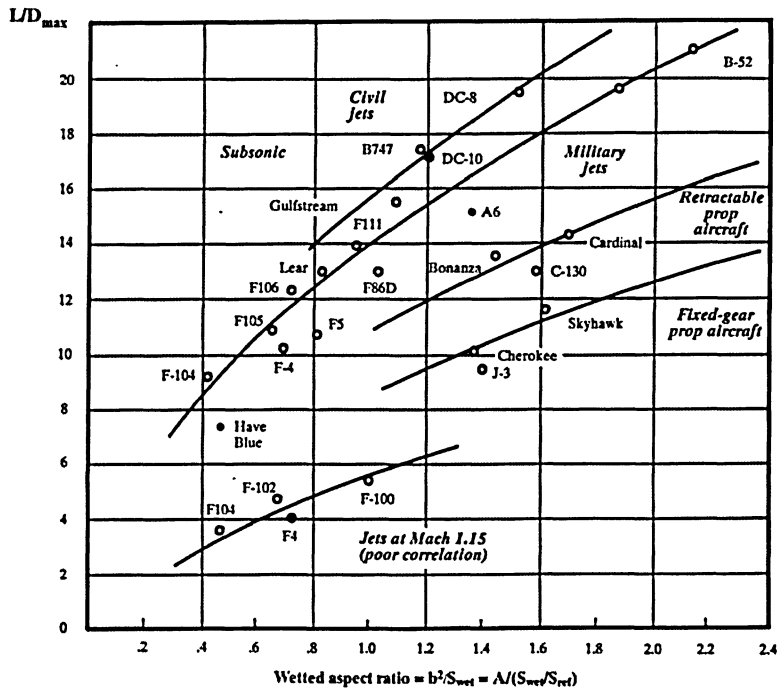

Figure 1.9 L/D ratio vs. Wetted Aspect Ratio. [8]

The wetted aspect ratio of an aircraft is given by the following equation:

$$\text{Wetted aspect ratio} = \frac{AR}{\left(S_{wet}/S_{ref}\right)} \tag{1.1}$$

Where:

$AR \equiv$ Wing Aspect Ratio

$S_{wet} \equiv$ Wetted Surface Area

$S_{ref} \equiv$ Wing Reference Area

Based on the outline given previously, S_{wet} is given as 44,000 ft² and 29,700 ft² for a conventional aircraft and the BWB configuration respectively. As outlined in the genesis of the BWB, both the conventional aircraft and the BWB have wing total surface areas of 15,000 sq. ft. This results in a wing reference area of 7,500 sq. ft. From figure 1.9, a Boeing 747 has a wetted aspect ratio of approximately 1.2. The Boeing 747 is a very similar aircraft to the conventional

aircraft used in the genesis of the BWB. Using this value in equation 1.1 an estimate of the wing aspect ratio for the conventional aircraft is calculated to be approximately 7. This value matches values of AR for aircraft of this nature found in literature. Further, assuming that this is the same value for the BWB configuration, an estimate of the wetted aspect ratio of the BWB can be calculated. Using the above values in equation 1.1, the BWB configuration has a wetted aspect ratio of 1.8, and using this value in figure 1.9 and following the statistical curve for conventional aircraft results in an L/D estimation of approximately 22, a substantial improvement over the conventional design.

The aircraft design in figure 1.4 was then refined into an actual aircraft by McDonnell Douglas. The disk fuselage and wing sections were blended into one another. The engines were merged with the fuselage at the rear, and a nose/cockpit bullet was added. The first generation of BWB aircraft is pictured in figure 1.10.

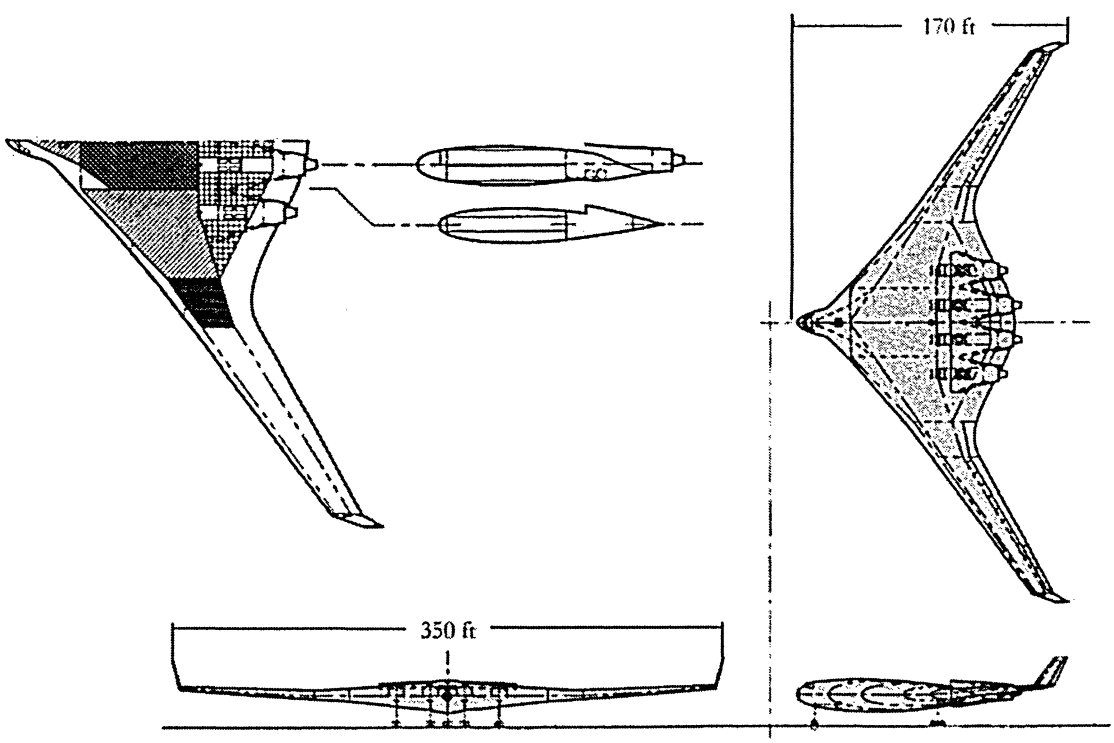

Figure 1.10 1st generation BWB. [7]

Realizing that the BWB configuration held definite potential, in 1994, the National Aeronautics and Space Administration (NASA) sponsored a three year industry/academic study of the BWB design. The results of this 3 year study are compared to a conventional aircraft design based on the same mission profile and are presented in table 1.1. Of particular note in table 1.1 is the

close approximation of the L/D value for the BWB based on the initial estimation. Figure 1.11 shows the conventional aircraft, and figure 1.12 shows the second generation BWB.

Model	BWB	Conventional
Passengers	800	800
Range (n. mi)	7,000	7,000
MTOW (lb)	823,000	970,000
OEW (lb)	412,000	470,000
Fuel Burned (lb)	213,000	294,000
L/D @ Cruise	23	19
Thrust (total lb)	3x61,600	4x63,000

Table 1.1 Comparison of conventional aircraft to 2nd generation BWB. [7]

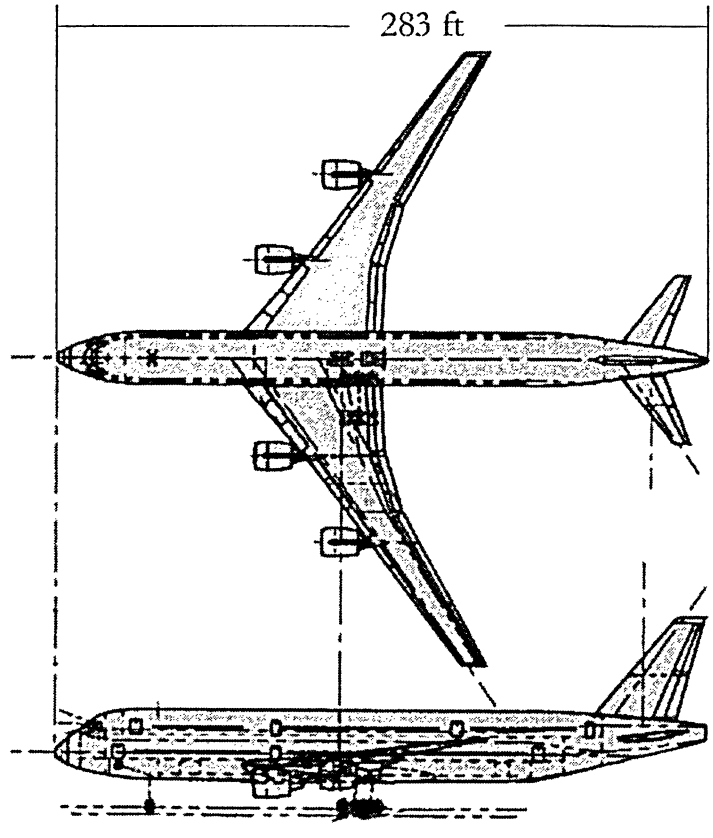

Figure 1.11 Conventional aircraft layout. [7]

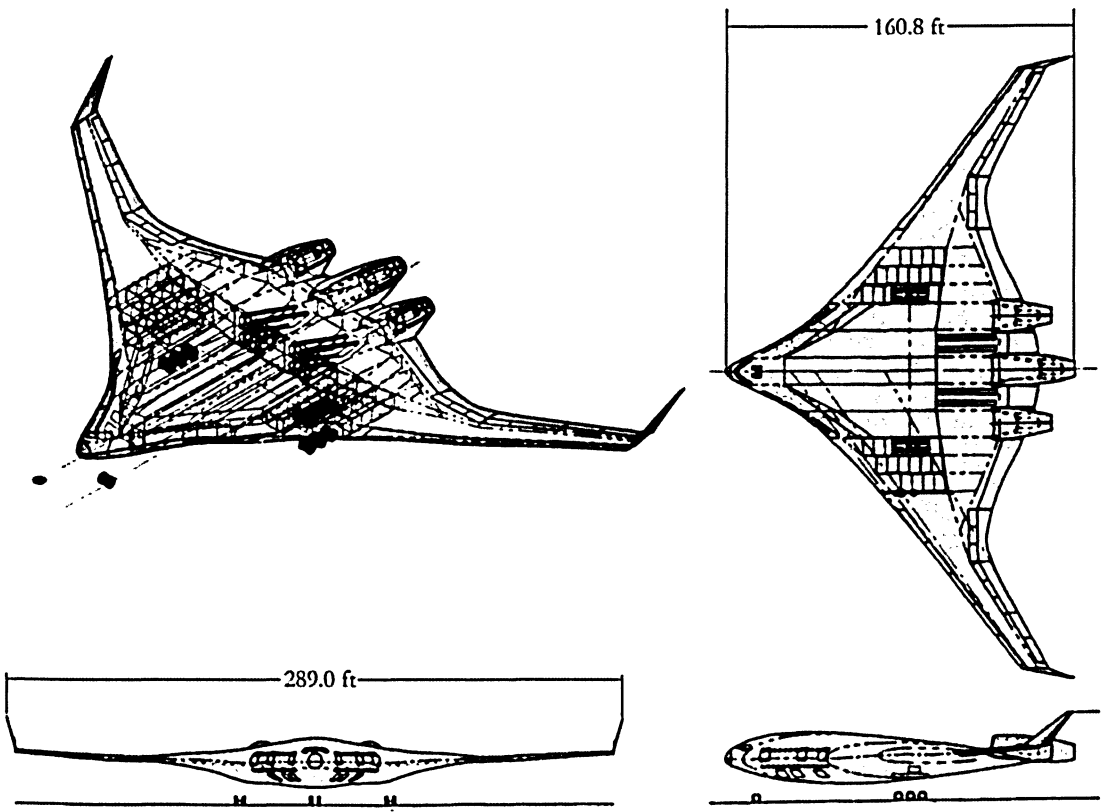

Figure 1.12 2nd generation BWB. [7]

In 1997, with the 3 year NASA sponsored study complete and demonstrating the performance and feasibility of the BWB, Boeing* decided to proceed with a preliminary design study of the BWB. The initial design mission of 800 passengers was deemed inappropriate and beyond the scope of market forecasts. The design mission was limited to 450 passengers; this offered the opportunity to compare the BWB with current and upcoming aircraft such as the B747, B777, A340 and upcoming A380. An additional requirement was added to the design mission which was the requirement for the aircraft to fit into existing airports. This required that the wingspan of the BWB be limited to 260 feet. Based on the new design mission and the design optimization described in references 7, 9, and 10 the BWB-450 baseline pictured in figure 1.13 was created.

The BWB-450 baseline design showed marked improvement in many areas, figure 1.14 compares the structural weight fractions of the BWB-450 with a conventional aircraft. A weight fraction is simply a way to compare the weight of two similar components. This allows for easy comparison of the two aircraft.

* In 1996 Boeing purchased McDonnell Douglas thereby acquiring all of its assets, including research into the BWB aircraft.

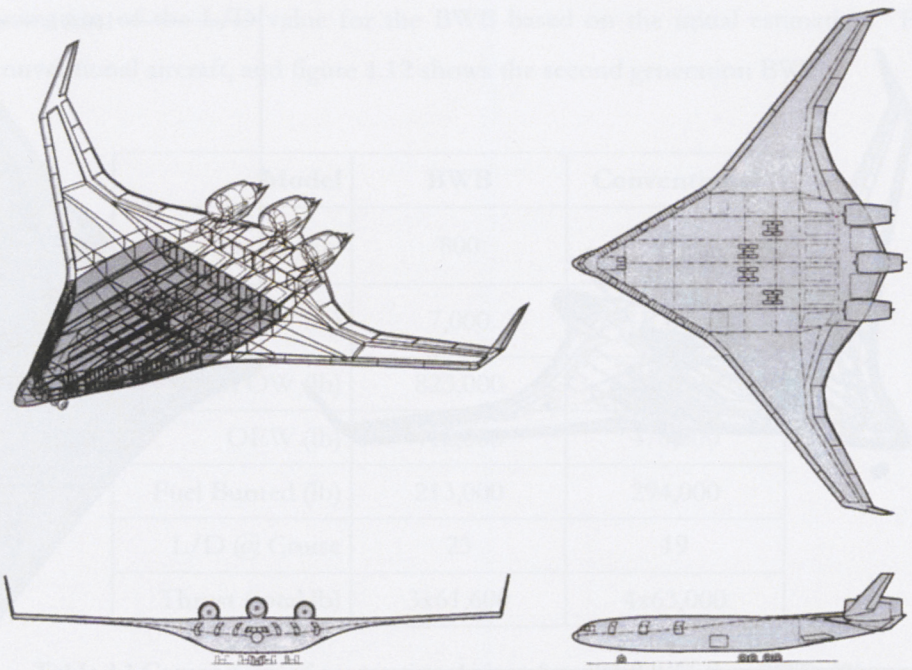

Figure 1.13 Baseline Boeing BWB-450. [7]

From figure 1.14 one could make the assumption that based on the BWB being lighter in both operating empty weight (OEW) and maximum takeoff weight (MTOW), as well as the fact that the BWB needs only 3 engines compared to the conventional aircrafts 4, that the fuel used by the BWB would be less than that of the conventional aircraft. This then translates to a lower fuel burn per seat, which can affect both the environment and an airline's economics

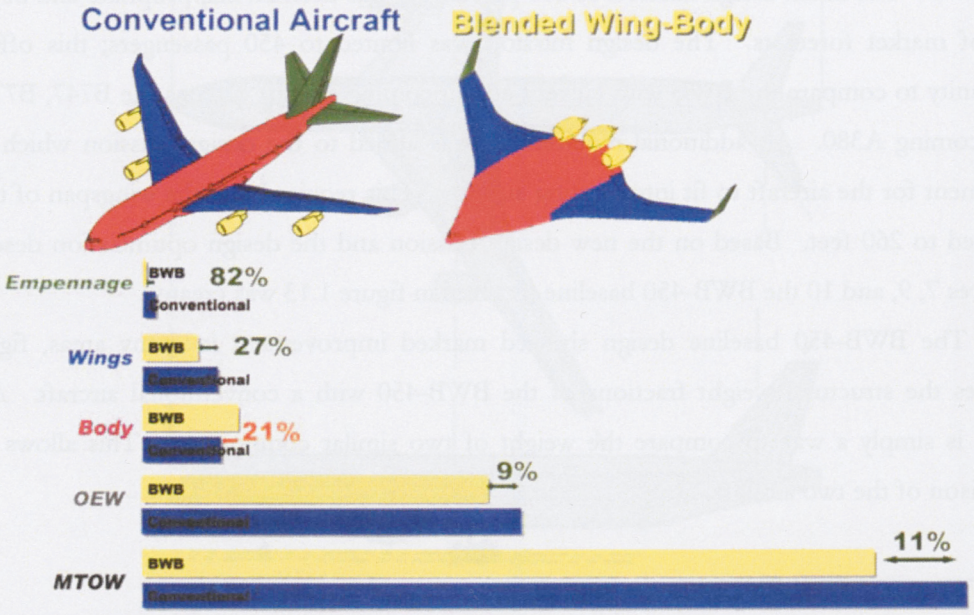

Figure 1.14 BWB and conventional aircraft structural weight fraction comparison. [7]

1.2 BWB Control Challenges

Many design challenges arise from the BWB configuration. From manufacturing to aerodynamics and passenger safety, the BWB presents many unique problems. One area of concern to designers and engineers is stability and control. Control of a flying wing design was one of the major issues which prevented the idea of a flying wing from proliferating in the aerospace industry in the early 50's when the AW-52 Horton and Northrop YB-49 were introduced.

In a conventional aircraft, the elevators located on the tail of the aircraft provide pitch control, the rudder controls yaw, and ailerons located on the wings provide roll control. With a flying wing design the tail is eliminated and therefore all aircraft controls have to be located on the wing. By moving all controls to the wing, the moment arms for pitch and yaw are greatly reduced. This requires that the aircraft have multiple large, rapidly moving, control surfaces. In the case of the BWB this comes in the form of trailing edge devices which perform multiple duties. The inboard elevons, a combination of elevator and aileron, provide pitch and roll control, while the outboard elevons have the added duty of being a drag rudder providing pitch, roll and yaw control. Winglets are also added to the wingtip to improve aerodynamic efficiency and provide yaw control. Figure 1.15 illustrates the control layout of the BWB.

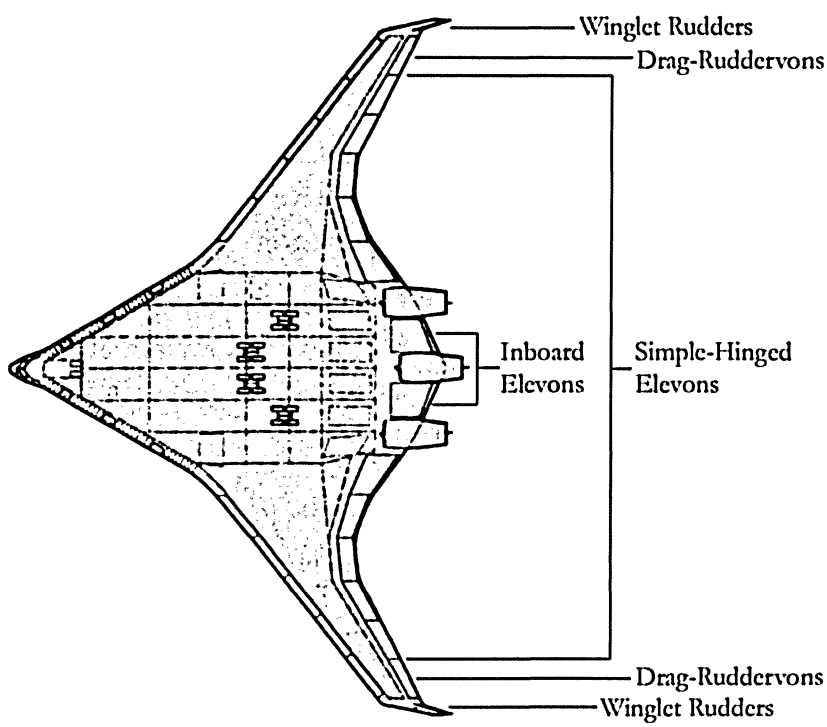

Figure 1.15 BWB control layout. [7]

Figure 1.16 demonstrates the use of the winglets as outboard ruddervons, a combination of rudder and aileron, in the event of engine out conditions. In this scenario the X marks the engine that has failed. With the far left engine inoperative, the aircraft will rotate counter-clockwise about the C.G. The left winglet is used as a ruddervon, producing lift force shown by the blue arrow causing a clockwise rotation. The right winglet is deployed as a drag rudder, producing a drag force indicated by the second blue arrow.

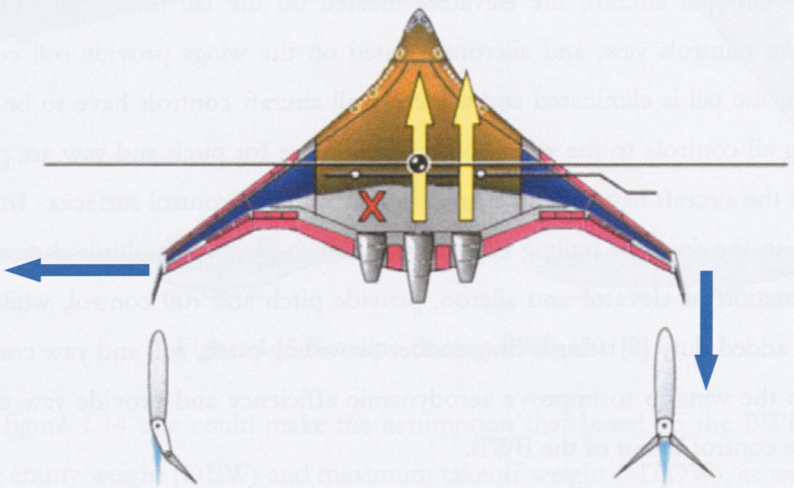

Figure 1.16 Yaw control in engine out condition. [4]

The reduction of an aircraft's control layout from the conventional wing and tail layout to the flying wing layout was outlined above. Aircraft such as the AW-52 Horton and YB-49 showed that a simple control layout for a BWB could be created with some degree of success. It wasn't until the advent of computers, fly-by-wire controls, modern avionics and the ability to write complex flight control laws that the flying wing concept went from merely being an aeronautical curiosity to being a perfectly reasonable configuration.

The control surfaces on a BWB aircraft tend to be larger than those control surfaces found on conventional aircraft and require the ability to rapidly change deflection angles. In the case of the inboard elevon on the BWB, the shear size of the control surface results in a large hinge moment. This hinge moment can be related to a representative length scale of the elevon control surface. The surface area of the elevon is proportional to the square of the representative length scale, while the hinge moment is proportional to the cube of this scale. The actuation power required then becomes a function of rate at which the control surface is moved.

$$\text{Power} = \text{Moment} \times \text{Rotation Speed} \tag{1.2}$$

$$\text{Moment} \propto \text{Length}^3 \propto \text{Area}^{\frac{3}{2}} \tag{1.3}$$

$$\text{Actuation Power} \propto \text{Area}^{\frac{3}{2}} \times \text{Rotation Speed} \tag{1.4}$$

A comparison can be made between the BWB and a commercial aircraft the MD-11 to illustrate the control surface actuation problem:

MD-11 inboard aileron:	41 ft^2 per side
BWB inboard elevon:	167 ft^2 per side

As mentioned previously, the loss of the tail of the aircraft and the resulting reduction in moment arms requires large rapidly moving control surfaces and thus the large difference between the control surface size of the MD-11 and BWB. Equation 1.4 can be converted to a ratio to allow a comparison between the required actuation power for the BWB and an MD-11. The area ratio of the control surfaces of the two aircraft is 4.07. Inserting this value into equation 1.4 results in an actuation power ratio of 8.2, if both control surfaces are deflected at the same rate. However, since the BWB requires a faster rate of deflection than that of a standard aircraft, the BWB will have a larger actuation power requirement. For example if the BWB requires twice the amount of control surface deflection from the inboard elevon, the BWB will require 16.4 times the amount of power required by the standard MD-11, meaning the power required to deflect the BWB elevon could deflect 16 MD-11 ailerons [12].

This poses a problem to the engineers and designers of the BWB. If all the control surfaces have large actuation power requirements, then this will severely hamper the efficiency of the control system and put a large strain on the design of this system. The question of hinge moment reduction through aerodynamic design is the main purpose of this work.

1.3 Previous Research

In 1942, the National Advisory Committee for Aeronautics (NACA), investigated the effects of several trailing edge modifications, and their effects on the hinge moments [13]. The research was initiated because of discrepancies between results found through potential flow theory and experimental results. It was found that the discrepancies in the values for hinge moments between experimental and theoretical values were dependent on the shape of the trailing edge and the deviation of the flow from the Kutta condition in potential flow theory. The work was conducted in

the NACA windtunnel using a model that spanned the entire span of the test section to model 2D flow. The results of the work showed a 50% decrease in the hinge moment when a beveled trailing edge was used. The research conducted was too general in nature to make any conclusions about the flow phenomena accounting for the change in hinge moment, but it was believed that it was a result of the change in the boundary layer thickness at the trailing edge as a result of the modification.

In 1947 and 1949, two papers were produced by the NACA summarizing research performed examining the lateral control qualities of an aircraft, and design considerations when making modifications to an aircrafts control layout that will provide suitable stability and control [14 and 15]. Part of the work investigated beveled trailing edges and again verified the fact that the modifications to the trailing edge had a significant affect on the hinge moment of the control surface. Again, no investigation into the flow phenomena that would account for this change was presented.

In 1954, the NACA investigated the effects of blunting the trailing edge of the ailerons on a 35° swept-wing airplane [16]. In this case, the standard aileron was replaced with a blunted trailing edge aileron as pictured in figure 1.18. The focus of the research was on improving the aircraft stability and control characteristics at high speed. The results showed improved performance of the aircrafts tracking and control at Mach numbers of 0.9 but with an associated increase in the aileron hinge moment. Studies at this time, however, were limited to basic experimental results and pilot input, and, although improvements were found in certain flight regimes, nothing further came of the studies.

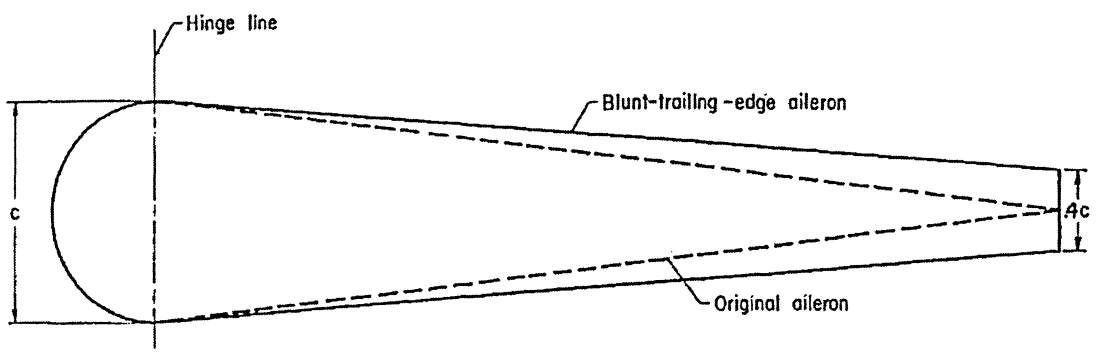

Figure 1.18 Modifications to trailing edge of aileron. [16]

Previous work performed by Harrison [17] investigated many different types of trailing edge modifications. The work was done in two dimensions and investigated beveled edges, rounded trailing edges, rounded beveled edges and a modified Frise nose modification. His work examined many variations to each of the above mentioned modifications, examining the effects each had on the flow over the control surface and the resulting lift, drag and moment coefficients. The results of his work showed that the beveled edge geometry held the most potential, specifically a bevel of anywhere between 60 and 75 degrees from the vertical provided the most gain.

Similar research was also carried out by Roman [18]. His work focused exclusively on beveled edge geometry and again was two dimensional only. The research showed potential in the beveled edge modification; however, it also revealed that this potential was significantly reduced at low speed.

The results of Harrison's and Roman's work showed that further research needed to be performed on a three dimensional level, at both high speed cruise and low speed cruise conditions. The work presented in this document will examine the effects of beveling the trailing edge of the inboard elevon using a three dimensional model.

1.4 Objectives

The objectives of this research are to build upon previous 2D work, and examine the 3D effects of trailing edge modification on the hinge moment. The ultimate goal being to suggest a way in which to alleviate the hinge moment problems of the BWB through selective aerodynamic design.

To accomplish this, a computational fluid dynamics (CFD) model was developed to investigate the flow over the BWB-450 model. The engine nacelles and wingtip winglets have been removed from the model in order not to complicate the grid generation process. The engine nacelles are mounted above the surface of the BWB wing and therefore there is little aerodynamic affect on the inboard elevon by excluding them from the CFD model. In the case of the winglets, they are a significant distance away to have any major affect on the aerodynamics of the inboard elevon. The primary goal is to investigate the effects of modification of the aft 15% of the trailing edge of the inboard elevon.

Three different geometries are examined at various flight conditions to investigate the three-dimensional effects of trailing edge modification. A baseline unmodified geometry acts as a reference for the other two models. These are compared to a 60^0 and 70^0 beveled edge modification. These modification values were selected based on the work performed by Harrison, which showed that the beveled edge modification produced improvement in this range. For each modification there is a neutral un-deflected state, a positive 5^0 deflection and a negative 5^0 deflection. In actual flight, the inboard elevons would see a maximum deflection of 10^o at high speed cruise values. All models are run at a typical cruise value of 0.85 Mach.

The structure of this thesis is as follows. Chapter 1 gives an introduction to the blended wing body aircraft, the advantages and challenges of the design, followed by chapter 2 which outlines the creation of the BWB CAD data. In chapter 3 discussions of grid methods and the process and challenges involved in building the grids are presented. Chapter 4 gives a brief discussion of the

mathematical concepts used by the flow solver and the settings involved. Chapter 5 presents the results obtained from this research followed by chapter 6, containing the conclusion of the thesis and ideas for the continuation of this work.

Chapter 2

Model Creation

2.1 Introduction

Section 2.2 outlines the data provided by Boeing. In section 2.3 the challenges of surfacing the BWB data is discussed followed by section 2.4 which outlines the creation of the wingtip cap. Section 2.5 discusses the creation of the deflected wing geometries and finally section 2.6 outlines the creation of the modifications of the trailing edge geometry.

2.2 Wing Data

The data for the BWB-450 was provided by Boeing Phantom Works in the form of x-y-z co-ordinates, mapping out 28 airfoil sections of the BWB-450, from the centerline out to the wingtip as shown in figure 2.1. The aircraft was split at the axis of symmetry which is common practice in the aerospace industry when modeling symmetrical aircraft using CFD. As no cross-flow situations will be modeled, a symmetry boundary condition will be applied on the symmetry plane. Modeling of half the aircraft in this situation allows for significant reduction in grid size and therefore a significant savings in computational resources. This data was imported into Gambit, a pre-processor software package produced by Fluent for the creation of computational grids for the use in CFD.

The next step in the creation of the model was to create splines through the data points. Manually creating the splines around each airfoil section, although possible, would have required a significant amount of time to accomplish. A small program written by Perera[19], was used to simplify this process. The program, which can be found in Appendix A, was written to take 2D x-y

co-ordinate data and add cubic spline data between each point. This program was modified to incorporate a third dimension and was used to create the geometry in figure 2.2.

Figure 2.1 removed due to proprietary reasons described on page ii.

Figure 2.1 BWB coordinate data.

Figure 2.2 removed due to proprietary reasons described on page ii.

Figure 2.2 BWB splined curves.

2.3 Wing Surfacing

With the BWB-450 airfoil sections splined, the next step was to create a surface over the splines forming the upper and lower wing surfaces of the geometry. Gambit was initially used to try to surface the model. Gambit requires that the user select 4 splines that makeup a complete face in order to produce a surface. The first method that was used to develop the upper surface of the wing, was to create a spline that was produced from the leading edge data points as well as a spline that was produced from the trailing edge data points. This would result in 4 splines that would encompass the whole of the upper wing surface. This however resulted in an inaccurate surface because the surface was produced using only the centerline and wingtip airfoil sections without any of the other 26 airfoil sections. Another method of surface rendering was tried, this time creating individual surfaces between each airfoil section of the BWB wing. The resulting surfaces were accurate, but did have problems which were encountered further on in the modeling process. Gambits modeling process is as follows;

1.) Create splines which outline the faces of the geometry
2.) Create faces from the splines created
3.) Create 3D solids from the faces created in step 2
4.) Fill the 3D solids with nodes and elements

The third step is what caused the problems in the second method when the BWB surface was approximated. By creating surfaces between the individual sections of the upper and lower surface of the BWB, gaps were left at the trailing and leading edges. Therefore Gambit could not correctly create a closed solid from the individual sections, and the modeling process could not continue.

An alternative method was devised using the surfacing capabilities of Catia. Catia, an advanced CAD program, was selected to surface the BWB-450 because of its ability to surface render the BWB-450 to the desired accuracy. Exporting the splined model pictured in figure 2.2 from Gambit as an IGES file and then importing the model into Catia, the surface of the BWB-450 was created using the spline surface command in Catia. The spline surface command allows the user to create a surface by selecting the splines that make up that surface. This process at first glance seems exactly the same as Gambits process; however in Catia the splines do not need to make up a closed face, instead the surface is created using only the splines of each airfoil section. A picture of the surfaced BWB-450 is shown in figure 2.3.

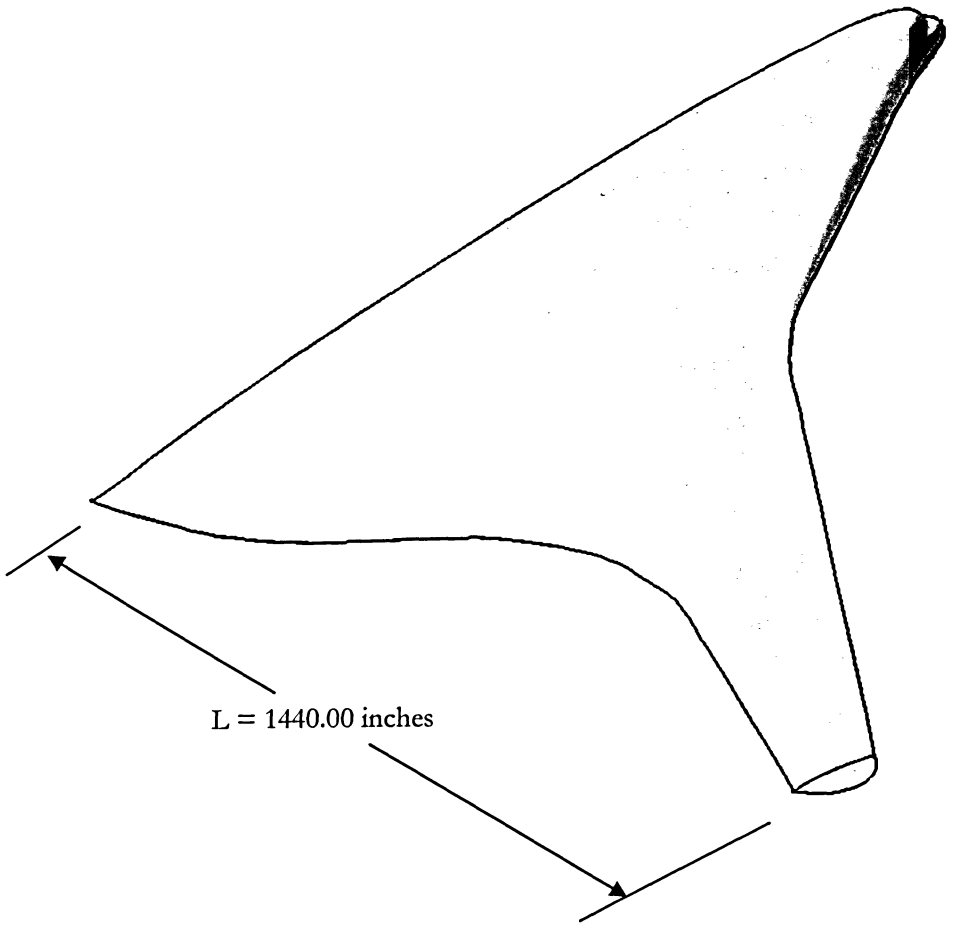

Figure 2.3 Isometric view of surface rendered BWB.

2.4 Wingtip Cap

The next step was to design a cap to cover the wingtip of the BWB-450. As mentioned previously in chapter 1, the winglets which would be found on the actual BWB-450 were not included in this model. However some form of wingtip cap was needed to alleviate the effects of wingtip vortices that would be produced by the abrupt cutoff. The cap placed on the wingtip was also designed to help with the grid generation process. The initial grid setup was to use a fully structured grid. This requires that the geometry be able to fit quad elements over the entire surface. The wingtip cap was designed so that it could be split into 4 distinct edges, the required amount to make a 2-D structured grid. Further details on this subject will be discussed in chapter 3. Figures 2.4 and 2.5 show surface rendered images of the top and isometric view of the wingtip cap respectively.

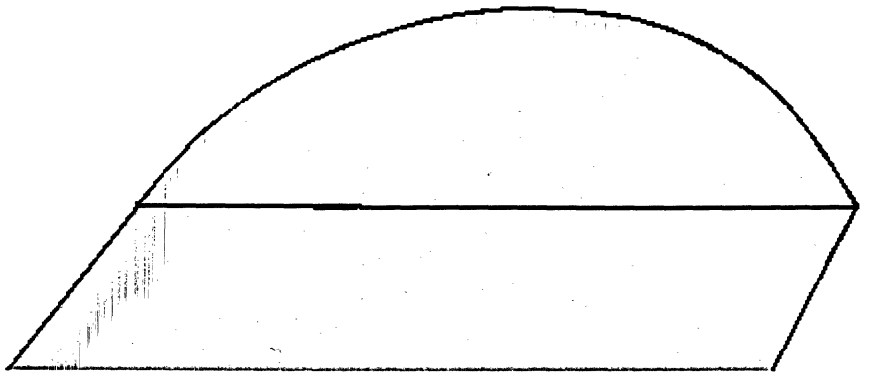

Figure 2.4 Top view of wingtip cap.

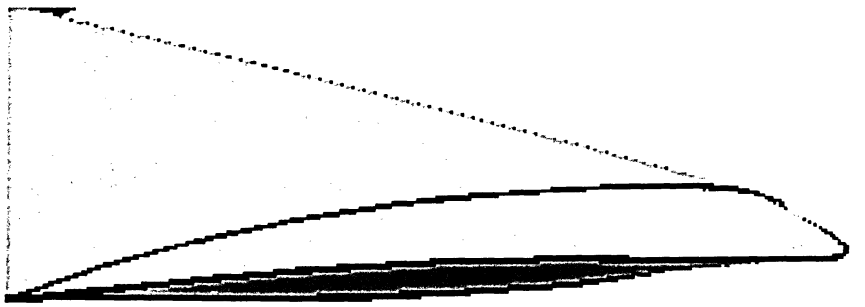

Figure 2.5 Isometric view of wingtip cap.

2.5 Deflected Geometries

With the baseline un-deflected model created, the next step was to create the deflected geometries. As mentioned previously in chapter 1, these would be a 5^0 positive and negative deflection. The location of the elevon was defined by the airfoil profiles located at 82.5 inches and 227.5 inches in the spanwise direction from the centerline of the aircraft and the airfoil profiles contained in between, with the total aircraft span being 1440.0 inches. The hinge line of the elevon is located at a constant longitudinal value of 1902 inches from the leading edge of the aircraft. To create the geometry of the deflected elevon, the data points of the elevon that were beyond this hinge line towards the trailing edge were rotated 5^o positive and negative. The deflected surface geometries of the baseline case, both positive and negative deflections are shown in figures 2.6 and 2.7 respectively. As can be seen in figures 2.6 and 2.7 gaps were left between the wing surface of the elevon and the surface of the wing. This was a done in order to assist with the grid generation process and is discussed in chapter 3.

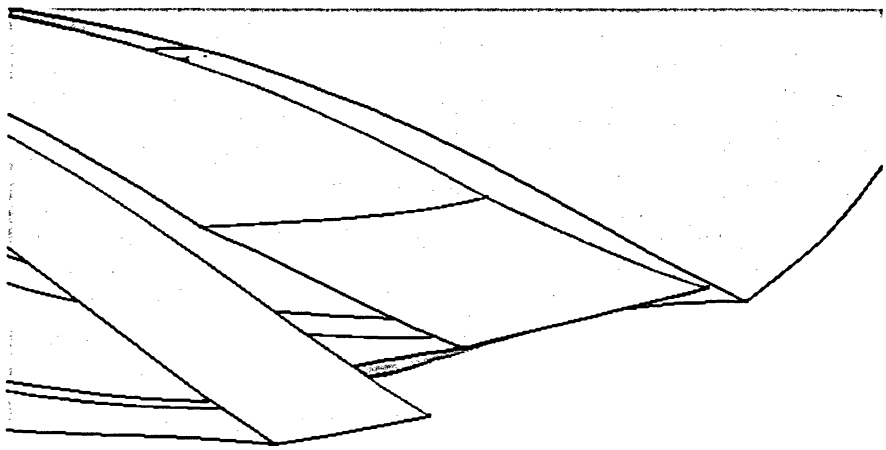

Figure 2.6 Isometric view of positive 5° deflection of inboard elevon.

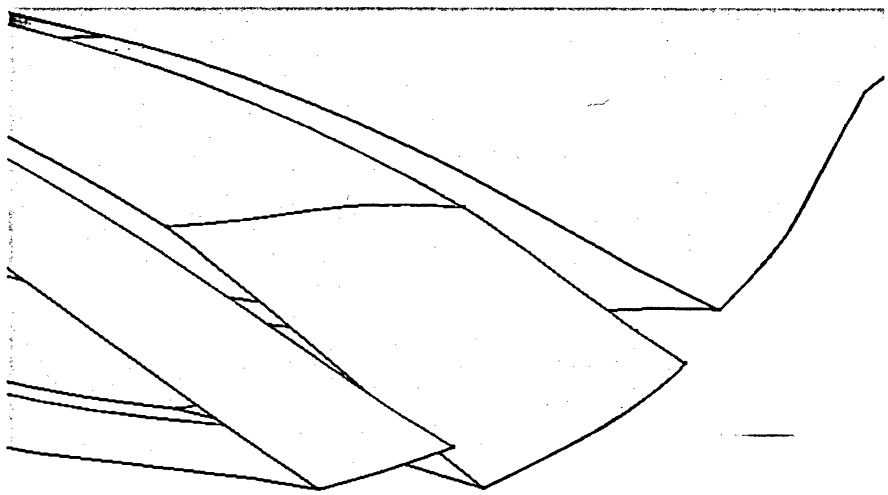

Figure 2.7 Isometric view of negative 5° deflection of inboard elevon.

2.6 Trailing Edge Modification

To create the beveled trailing edge geometry the last 15% of the elevon trailing edge was modified. This value was selected based on the work done by Harrison [17]. The modifications that were chosen for further analysis, based on the 2D analysis performed by Harrison [17], were 60 and 70 degree deflections from the vertical. To create these geometries, a vertical line was first created at a distance of 15% in from the trailing edge. A horizontal line was then created from the midpoint of the vertical line to the trailing edge. Using simple trig functions based on the 60 and 70 degree deflection angles required, the required length of the horizontal line is determined. This line is then trimmed to the required length. Next, a line is created joining the points at which the vertical line intersects the airfoil splines and the end point of the newly created horizontal line. Figure 2.8

illustrates this process. This process was repeated for each airfoil section which defined the elevon. This process was performed for both 60 and 70 degrees of bevel, and performed for all scenarios, un-deflected, 5° positive deflection and 5° negative deflection. With the new modified geometries created, the geometry was exported as an IGES file to Catia for surfacing. Figure 2.9 shows the completed modified geometry of the BWB inboard elevon for positive 5° deflection with 60° beveled edge modification.

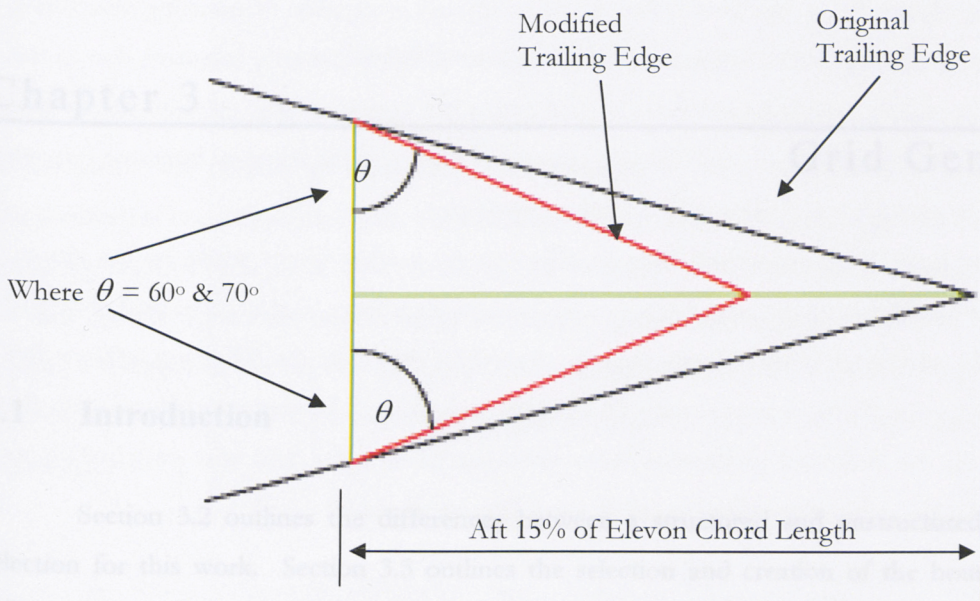

Figure 2.8 Modification of trailing edge.

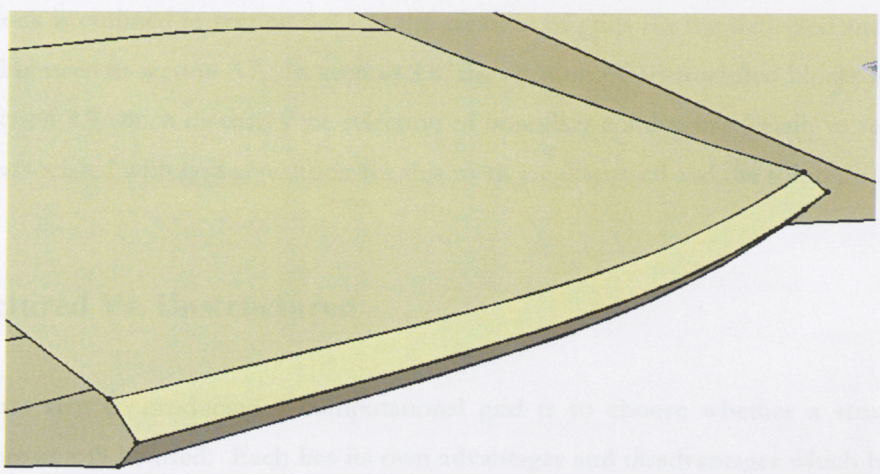

Figure 2.9 Isometric view of modified inboard elevon with 60° beveled trailing edge.

Chapter 3

Grid Generation

3.1 Introduction

Section 3.2 outlines the differences between a structured and unstructured grid and the selection for this work. Section 3.3 outlines the selection and creation of the boundary domain, followed by section 3.4 which outlines the creation of the grids. In section 3.5 techniques used to improve the quality of the grids is discussed with brief outlines of these techniques. The creation of a structured block is outlined in section 3.6 and the creation of grids for the deflected and modified geometries is discussed in section 3.7. In section 3.8, the creation of unstructured blocks is outlined, followed by section 3.9 which discusses the selection of boundary conditions. Finally in section 3.10 the challenges associated with grid generation for this work are discussed and the solutions found.

3.2 Structured Vs. Unstructured

The first step to producing a computational grid is to choose whether a structured or unstructured format will be used. Each has its own advantages and disadvantages which have to be assessed when producing a grid. The use of the terms unstructured versus structured can be misleading, as any grid that is produced must have some structure to it. These terms refer to the arrangement of the data structure of the grid. As an example, in a structured grid, the grid points $N_{i,j}$ and $N_{i+1,j}$ are direct neighbors, that is, non-boundary grid points have the same number of neighboring points. This leads to grids which are memory efficient computationally. In an

unstructured grid, each grid point requires a specific definition of its connectivity to neighboring grid points. This leads to the creation of connectivity matrices to define the grid and therefore an increase in memory usage. These two grids can be combined and used in conjunction to form a hybrid grid [20].

The factors which are involved when choosing what type of grid to use include model complexity (geometrical and flow field complexity) and the amount of computer resources available. For this problem, Fluent 6.0 is the flow solver being used, and is capable of handling structured, unstructured and hybrid meshes. Unstructured grids tend to be more memory intensive due to the added connectivity matrix required to define the grid form, but provide easier creation of the grid when complex geometries are involved. Whereas structured grids are less memory intensive but can become difficult to create when dealing with complex geometries.

Boundary layer development will have an effect on the surface forces acting on the elevon. In order to build a grid that would accurately model the boundary layer, a structured grid with grid clustering near the surface of the BWB was chosen. As will be shown in the following sections this method worked for the BWB geometry with an un-deflected elevon. However problems with the structured grid on the deflected geometries were encountered and the grid was switched to an unstructured grid. This will be discussed in full in the following sections.

3.3 Model and Domain Creation

Gambit is a pre-processor capable of both CAD production and grid production, however due to limitations in the software which were mentioned in chapter 2, the code Gridgen by Pointwise was selected to create the grid.

The first step in grid generation is to define the global boundaries of the model. This step involves either the direct creation of geometry using Gridgen's CAD capabilities or importing geometry that has been created in a separate CAD package. With the BWB model already created in Catia, the model was imported into Gridgen as an IGES file. Gridgen imports the individual elements of the model, i.e. splines, surfaces and volumes, as database elements. With the model imported into Gridgen, the next step was to create the connectors around the boundaries of the model. Connectors are Gridgen's most basic grid element. They are curves which then have grid points distributed over them. Gridgen has the ability to rapidly create connectors by placing them over defined database elements. In this case the connectors were created on the database entities that defined the shape of the BWB and are pictured in figure 3.1.

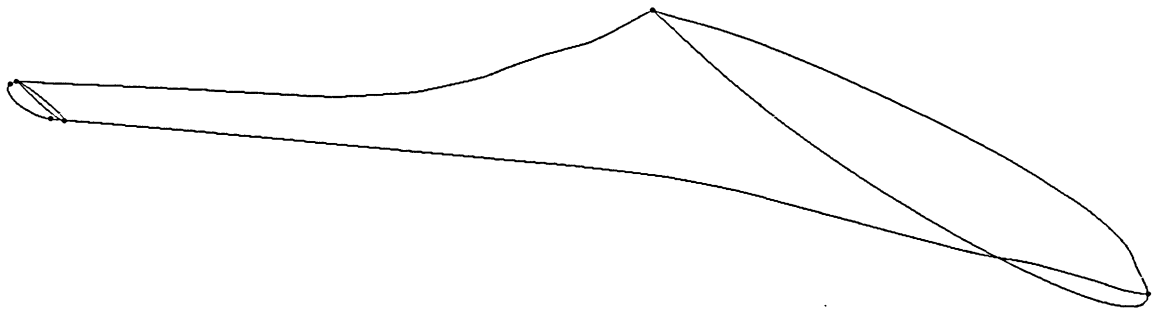

Figure 3.1 BWB baseline neutral case connector layout.

Next, geometry is created that will represent the boundary of the domain in which the model is contained. The boundary of the domain is dependent on the type of problem being examined. If the problem is one of internal flow, the boundary of the domain is defined by the constraints of the geometry itself. For external flow problems, the boundary of the domain is a model of the volume or area around the model that is being simulated. This could be a test chamber such as a wind tunnel, a room or in the case of this problem the air surrounding the aircraft during flight. For this type of boundary domain a common grid type is the C-grid, and an example of a C-grid is pictured in figure 3.2.

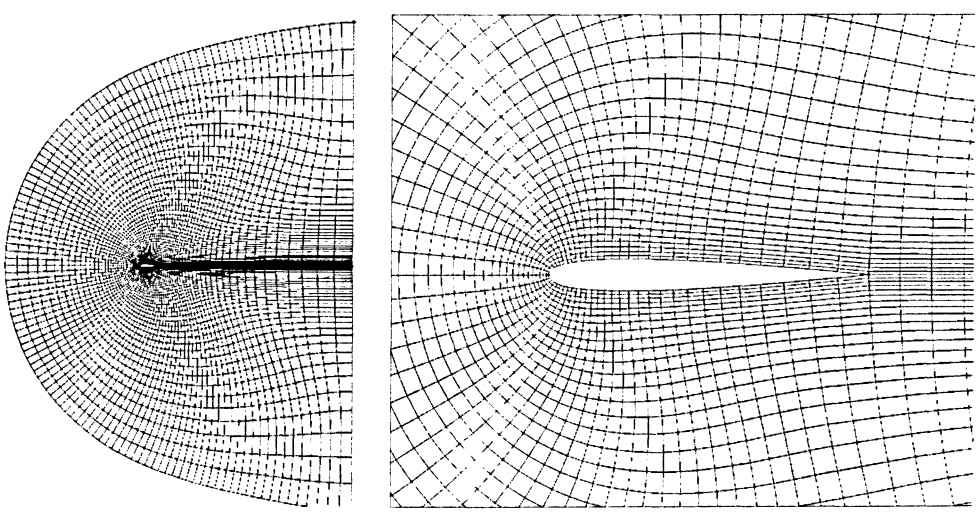

Figure 3.2 Example of a C-Grid around an airfoil.

The reason for selecting this shape can be seen in figure 3.2. The parabolic shape allows for the production of a smooth grid transition around the airfoil Geometry. The C-grid developed from structured grid generators that produce meshes which conform to the desired orthogonal nature of structured solvers. In figure 3.3 an example of a boundary fitted grid is shown, similar in nature to

the C-grid in figure 3.3. Figure 3.4 illustrates the mapping of the boundary fitted grid from the physical plane to the computational plane.

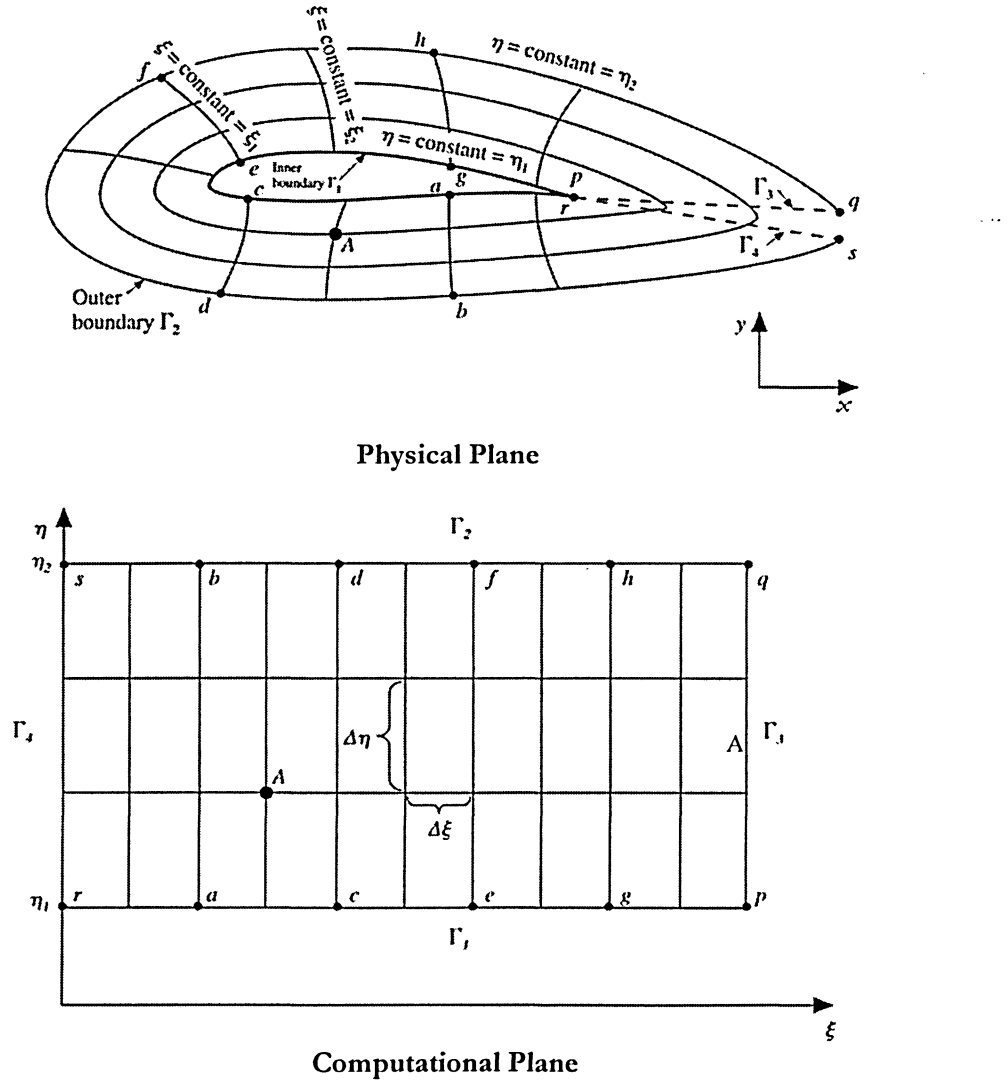

Figure 3.3 Boundary fitted grid mapped from physical plane to computational plane. [21]

This orthogonality is desired to accurately model the viscous effects on the surface of the airfoil. This type of domain however, becomes problematic past the end of the wingtip of the BWB. When the grid lines produced by a structured grid reach the end of the wing in the spanwise direction there is no longer any shape in the physical plane for the elements to wrap around as shown in figure 3.3. The resulting elements are skewed, having high aspect ratios or are malformed. One solution to this problem that was examined was to create a dome wingtip cap and rotate one side of the domain around the x-axis at the wingtip.

To achieve this, a structured grid was produced on the dome surface using what Gridgen calls a pole domain. This domain is a structured grid collapsed to a line and is necessary when dealing with singularities such as those that would be found at the sharp trailing edge of the dome surface and the curved portion at the leading edge. However the resulting grid was incapable of being exported to Fluent. This result was due to the fact that Fluent would not recognize Gridgen's pole domains and tried to replace them with tetrahedral elements which created difficulties. The solution to the problem was to change the shape of the outer domain and change the design of the wingtip. The shape for the outer domain that was chosen was a rectangular domain as pictured in figure 3.4. This domain does not suffer the same problems as the parabolic shape past the wingtip. In the case of a rectangular domain, grid lines are required to flow from the back of the block to the front, and flow over any object that is present, in this case an airfoil and simply create straight lines in the event that there is no object to map to.

In figure 3.4, the layout of the block structure used in the baseline neutral configuration is presented. The positive X, Y, and Z axis is labeled and the 4 blocks numbered one through four. The aircraft is highlighted by the red circle. Figure 3.4 will be referenced throughout the discussion of the grid generation process.

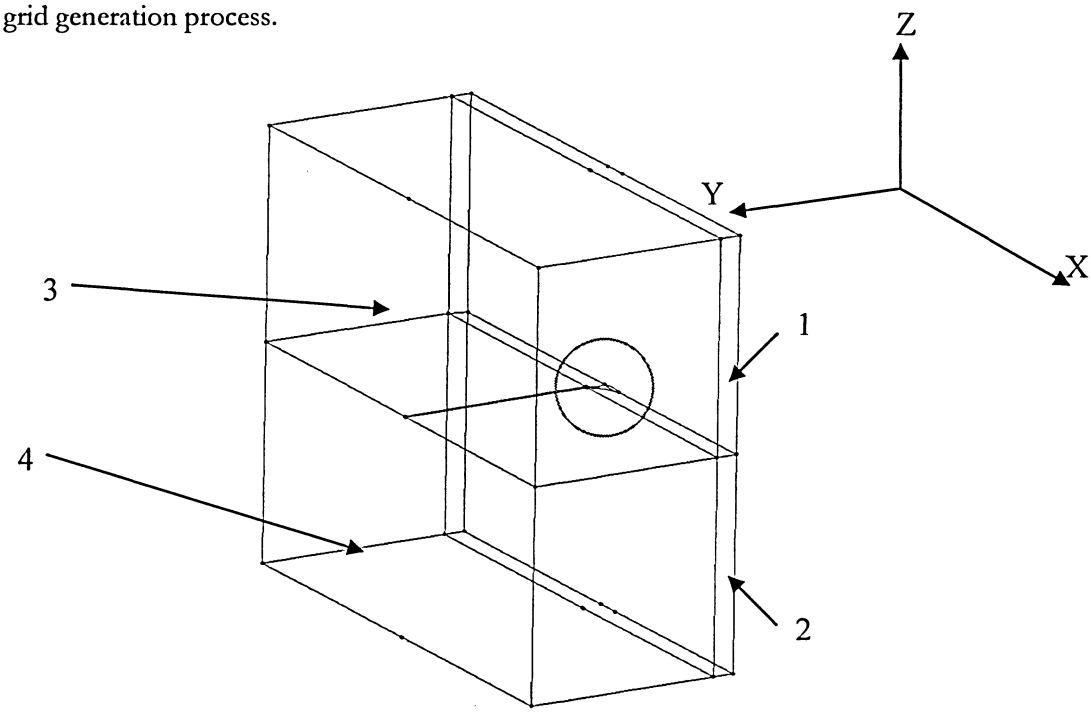

Figure 3.4 BWB baseline block layout.

The only drawback of the rectangular domain arises at the leading edge of the aircraft where the grid has to make an abrupt change in direction. This problem is reduced as the grid moves from the centerline out towards the wingtip where the change in direction is not as severe. Figure 3.5 illustrates the change in direction at the leading edge located at the centerline of the aircraft.

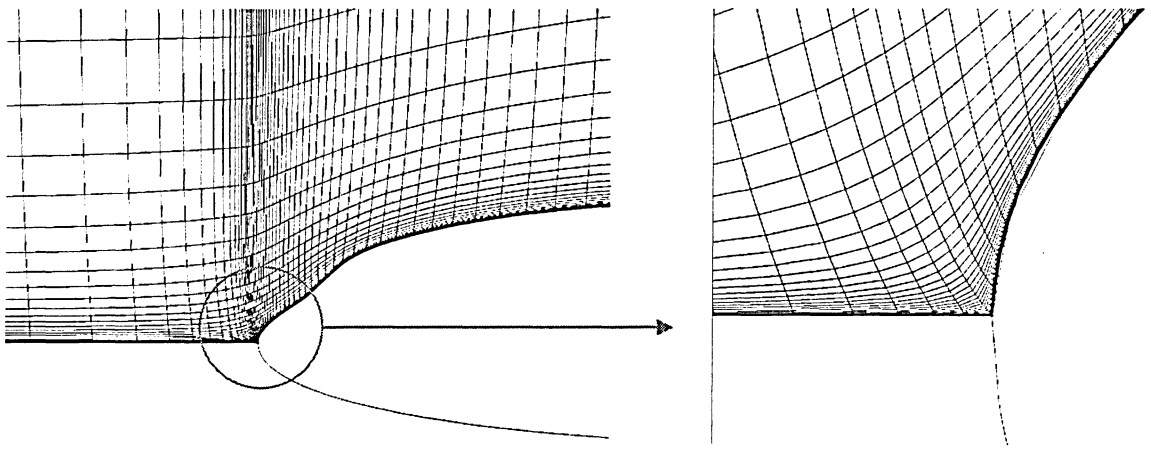

Figure 3.5 Structured grid over leading edge of BWB, including close-up.

Initially, Gridgen automatically produces a surface domain using an algebraic method called transfinite interpolation or TFI. This produces a grid as pictured in figure 3.6 below.

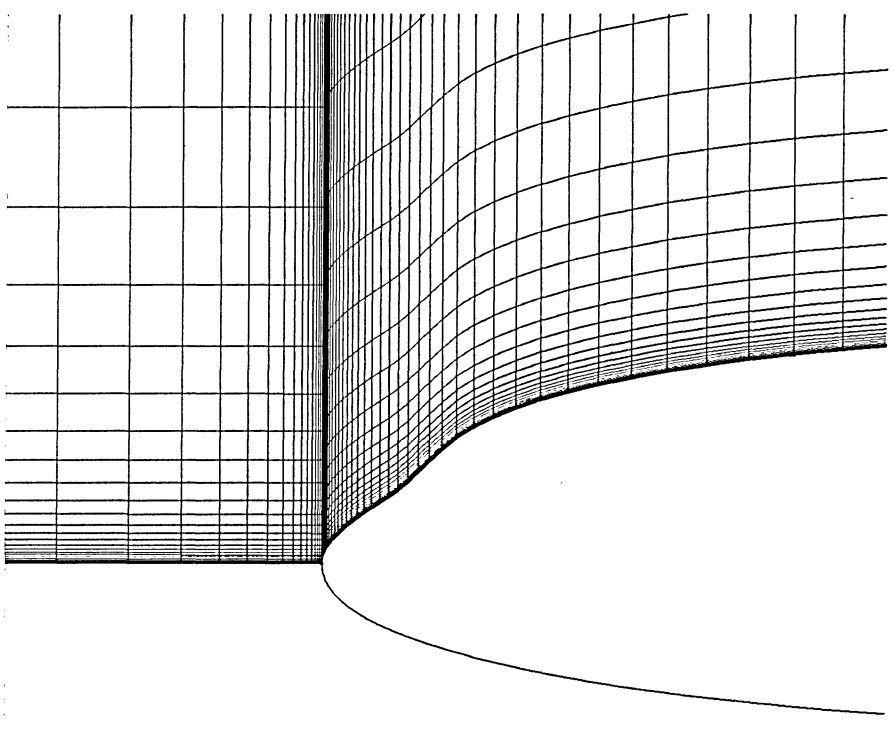

Figure 3.6 Initial grid using gridgens standard TFI.

To obtain the smooth grid transitions as pictured in figure 3.5, Gridgen's structured grid solver is applied. The structured grid solver uses elliptic partial differential equation (PDE) methods to smooth the clustering of the nodes on the grid [22]. These methods will be explained further in a later section.

The other drawback with a rectangular domain is that the grid size, i.e. number of nodes, is larger than that of a C-grid. This is a result of the added section in front of the model and the larger total domain volume.

The limits of the rectangular domain were sized large enough so that the effects of the aircraft on the fluid surrounding it would dissipate to the set boundary conditions at the domain extents. The standard value in CFD solutions, when modeling aircraft, is 20x the fuselage length in the x, y and z co-ordinate direction. For example, an airfoil with unit chord length would have the minimum distance to any boundary as 20 units in any direction, provided the Reynolds number is high, on the order of 10^6.

At this point it is appropriate to take a step back and examine a point that was discussed in chapter 2. As mentioned previously, the cap on the wingtip was created both to help alleviate wingtip vortices as well as assist in grid creation. With the rectangular domain and the way the grid is sectioned, it was necessary to create a wingtip cap that would assist in allowing the grid to properly transition over the end of the wing. The shape of the wingtip cap was shown in figures 2.3, 2.4 and 2.5 of chapter 2. Figure 3.7 shows the wingtip cap with the connectors that separate the domains.

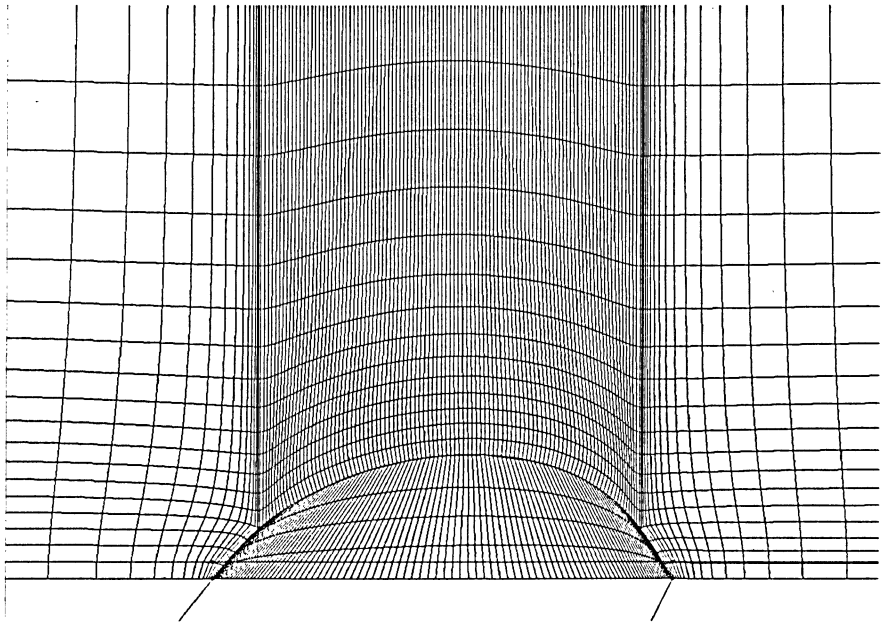

Figure 3.7 Top view of grid on wingtip cap.

As can be seen, the shape of the cap helps by allowing the grid lines running from right to left as well as top to bottom in figure 3.7, to flow around the model smoothly without creating sharp direction transitions that might produce skew or misshapen elements. With the model and domain successfully imported and created in Gridgen, the next step is to determine the density of the grid.

3.4 Number of Nodes, Spacing and Density

The next step in the grid generation process is to decide on the size of the grid, i.e. the number of nodes per connector, the density, and the node spacing. The size of the grid that is used is dependent on a number of factors. These include whether or not the model includes viscous effects such as boundary layer modeling, the required accuracy of the model as well as the computer resources available.

The majority of the grid spacing/density choices are based on the expected flow patterns around the model, such as areas where the flow characteristics will be changing rapidly such as stagnation points, model edges and areas where shockwaves form. Another driving factor in the grid spacing/density is the degree of surface curvature and the amount of variation of the curvature over a surface. Although one can use higher order splines and advanced geometry commands in CAD programs to create a model, the model is only as good as the number of nodes and the node spacing used to create it.

In the case of the BWB-450, there exist all of the above mentioned factors. The shape of the BWB is very complex and thus requires a suitable amount of nodes to accurately model the curves of the flying wing. Viscous effects are also examined and so drive the grid density in certain cases. Also the computer resources have to be taken into account. Create a fine grid and the computer resources available will require excessive run times. Create the grid too coarse and any results obtained may not resolve the modeled flow field sufficiently.

The number of nodes used in the model is based on grids built by Dino Roman of Boeing Phantom Works so as to save both computational resources and the time available for actual grid generation. Grids built by Boeing had obtained accurate results with a C-grid that had just fewer than 1 million nodes. These grids were built in the following way; 225 nodes were applied around the airfoil section, 32 nodes in the wake section, 49 nodes along the wing in the spanwise direction, and finally 65 nodes normal to the surface of the wing. An illustration of the node layout is shown in figure 3.8.

Although the actual accuracy of the model is dependent on both the gird and the flow solver, this layout was used as a guide to produce the grid around the baseline neutral configuration. As a result of the nature of a rectangular domain, i.e. its tendencies towards more nodes than a C-grid, slight modifications were made to the node scheme. For this model the airfoil had 100 nodes over the top surface and 100 nodes around the lower surface, 30 nodes in the front and rear wake sections each, 50 nodes in the spanwise direction, and 65 nodes normal to the aircrafts surface. 25 nodes were used in the spanwise direction extending from the end of the wing, over the wingtip cap and out to the farfield. The grid around the baseline neutral configuration was split into 4 separate

blocks, 1 representing the upper surface of the wing extending to the front of the domain, to the back of the domain, and extending out spanwise to the cutoff. The cutoff represents the point at which the airfoil data provided by Boeing ends and the wingtip cap begins. A similar block represents the lower surface of the airfoil. Two blocks, one upper and one lower, start at the cutoff and include the wingtip cap, and extend to the farfield. An illustration of the grid layout was presented in figure 3.4.

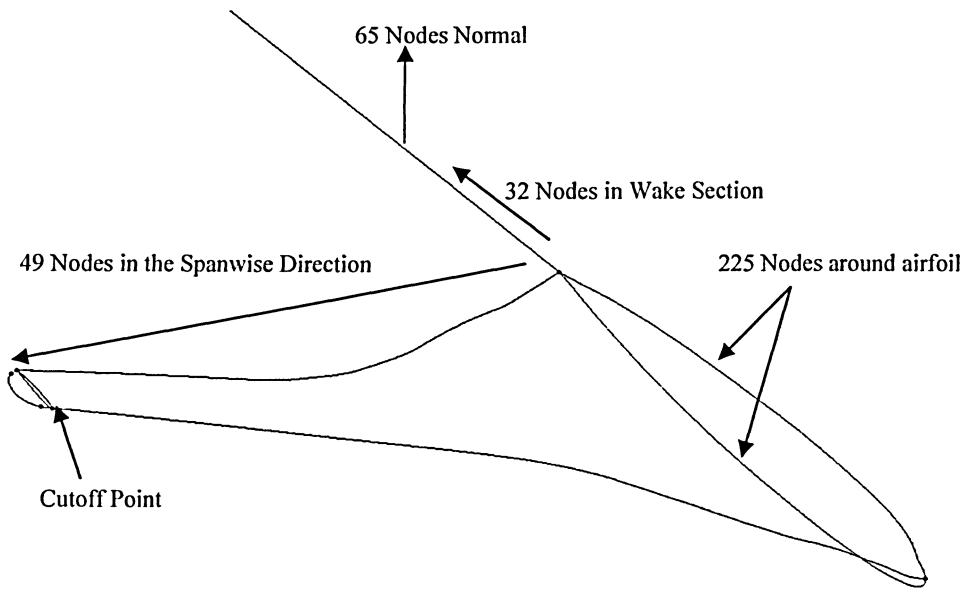

Figure 3.8 BWB node layout.

With the number of nodes per connector selected, the next portion of the process is to select the appropriate spacing. As mentioned previously the desired spacing is driven by the shape of the model, the flow characteristics involved and the required accuracy. Gridgen has numerous methods for distributing the nodes over the connectors. The default distribution scheme used by Gridgen is the hyperbolic tangent (TANH) function [23]. The TANH function distributes the nodes uniformly using a uniform interpolation scheme. In the case of the connectors which defined the upper and lower surface of the wing, the nodes needed to be concentrated near the leading and trailing edges. This was required to accurately model the curvature of the wing at the leading edge, and the subsequent changes in flow characteristics around this curvature. At the trailing edge the effects of boundary layer separation required that nodes be clustered here as well. At both the leading edge and trailing edge the distribution at the ends of the connectors were constrained. In Gridgen, nodes are distributed based on the first node spacing along the connector and the distribution function selected. Boeing's computational grid used 0.1% of the reference chord length initial spacing at the leading edge and 0.2% of the reference chord length spacing at the trailing edge.

Using the reference chord length of 1067 inches this results in values of approximately 1 inch and 2 inches initial node spacing, at the leading and trailing edges respectively. By constraining the leading edge and trailing edge node distribution, Gridgen switches from the uniform distribution of the TANH function to a geometric progression function. When geometric progression is selected, the successive spacing of each node will increase monotonically towards the end of the connector. Figure 3.9 shows the results of this.

Figure 3.9 removed due to proprietary reasons described on page ii.

Figure 3.9 Node layout on centerline airfoil section.

Since a structured domain was used, the same number of nodes and node clustering that was used on the profile at the symmetry plane was used at the wingtip. In the spanwise direction the nodes were equally spaced from the centerline to the wingtip. Modifications were tried near the mid-span of the wing to try to accurately cluster nodes near the curvature at this location in the wing, however this resulted in surface grids with skewed elements, therefore a uniform distribution was retained. With a grid on the connectors that define the upper and lower wing profiles, structured domains on the upper and lower surfaces of the wing were created and are shown in figure 3.10.

Figure 3.10 removed due to proprietary reasons described on page ii.

Figure 3.10 Top view of airfoil surface grid.

Next the wake domains in front and behind the wing were created. These domains were simple to create since the node clustering on the connectors which define these domains are constrained by the node clustering on the wing surface. For the connectors which extend in the positive and negative x direction, from the leading and trailing edges out towards the farfield, the end of the connector which meets the leading and trailing edges were constrained to have the same node spacing as the connectors which define the airfoil section. From this point geometric progression was applied to distribute the nodes out towards the farfield with the node spacing increasing as you move further from the leading and trailing edges, as pictured in figure 3.11.

Figure 3.11 removed due to proprietary reasons described on page ii.

Figure 3.11 Node distribution for wake sections.

This format was chosen for two reasons. First, it provides a smooth transition into the wake from the wing surface, and second as the nodes move further from the wing and closer to the farfield, the changes in the flow characteristics become negligible to the point where they match free stream values and therefore tight clustering is not required. The node spacing for the connector at the farfield in the spanwise direction was copied from the spanwise connector of the wing. The front and back wake domain grids are shown in figure 3.12.

Figure 3.12 removed due to proprietary reasons described on page ii.

Figure 3.12 Wake section surface grids.

Next the top and bottom domains of blocks 1 and 2 are created. The connectors running in the spanwise direction are created using the same clustering as used by the spanwise connectors in the wake domains. Gridgen has the unique ability to copy the node spacing and density settings

from multiple connectors to a single connector. In this case the node spacing/density was copied from the connectors that make up the front wake, BWB surface, and trailing wake. Upon doing so, Gridgen gives the option of copying the scaled distances. If this option is selected the distribution is a general distribution, rather than one of Gridgen's mathematical functions, which is copied from the selected connectors. This allows the distribution of nodes of the adjacent connector to follow the same pattern as the connectors from which the distribution was copied. This produces surface grids which follow approximately the same pattern. This option is advantageous when creating complicated structured grids as it helps to eliminate the formation of skewed elements.

With grids on the top and bottom of blocks 1 and 2 created, the next step was to create the sides. Having already defined the grid on 2 of the 4 connectors for each side, only 2 connectors, those running along the positive and negative z axis required a grid. The grid on these connectors would be similar to those that created the wake sections in that the grid would go from high density at the surface of the airfoil to a coarse low density grid at the farfield. The grid spacing at the surface of the airfoil, better known as the off wall spacing is determined by the parameter y+.

As mentioned previously grid generation is dependent on the type and characteristics of the model being simulated. When dealing with off wall spacing and y^+, specifically this deals with the turbulence model and viscous characteristics which are being modeled. For these simulations the Spalart-Allmaras (S-A) turbulence model is used [24]. This one equation turbulence model was selected since it is the least expensive, in terms of computational resources of Fluent's turbulence models. As well, the S-A turbulence model has been widely implemented in the aerospace industry in problems that, like those being modeled in this thesis, are external aerodynamic problems.

In order to properly implement the S-A turbulence model, Fluent recommends that the near wall mesh be either fine $y^+=0(1)$, i.e. is of order 1, so as to ensure that the first node off-wall is within the viscous sublayer, or a coarser near wall mesh, $y^+\geq 30$ so as to model the viscous sublayer using wall functions.

The parameter y^+ is a non-dimensional parameter and is defined as:

$$y^+ = \frac{\rho u_T y}{\mu} \tag{3.1}$$

where;

$u_T = \sqrt{\frac{\tau_w}{\rho_w}} \equiv$ friction velocity

$y \equiv$ distance from the wall to the node

$\rho \equiv$ fluid density

$\mu \equiv$ fluid viscosity

Since only a fully resolved boundary layer would permit modeling of separated flows, the $y^+=0(1)$ condition was adopted. This would ensure that an adequate number of nodes would be placed within the boundary layer. An estimate of the off wall spacing could be determined through the use of Equation 3.1, however this would be rather cumbersome as a result of the required data such as the friction velocity. Instead, a NASA CFD resources website [25] was used. This website uses a Java script calculator that is capable of calculating y given a y^+, a Reynolds number and reference length, which in this case are all known quantities. Based on a y^+ of 1, a reference length of 1068.7 inches (reference chord) and a Reynolds number of 181.7×10^6, an estimate of the first node spacing was calculated as 0.0002 inches. This value was input in Gridgen as a constraint at the ends of the connectors and Gridgen's geometric progression function was used to distribute the nodes along the connectors. Using Gridgen's grid examination tool the grid was checked, revealing folded elements. To correct this problem, the off wall spacing was increased to a value which Gridgen could satisfactorily produce a grid. This value was 0.001 which using the aforementioned process results in an estimated y^+ value of 5. Although Fluent recommends a y^+ value of 1 when using the S-A turbulence model, a value of 5 is still acceptable since the laminar sub layer can be modeled accurately with a y^+ range of 1 through 10. With the final connectors meshed, grids were produced on the sides of blocks 1 and 2. The final grids for the sides of block 1 are shown in figure 3.13 and 3.14.

Figure 3.13 removed due to proprietary reasons described on page ii.

Figure 3.13 Centerline airfoil side grid.

RYERSON

Figure 3.14 removed due to proprietary reasons described on page ii.

Figure 3.14 Wingtip airfoil side grid.

Figure 3.15 is a display of the y+ value as calculated by Fluent after the baseline grid reached a converged state. Figure 3.15 shows that the estimate found using the NASA website gave an accurate grid spacing to fully resolve the boundary layer over the surface of the wing.

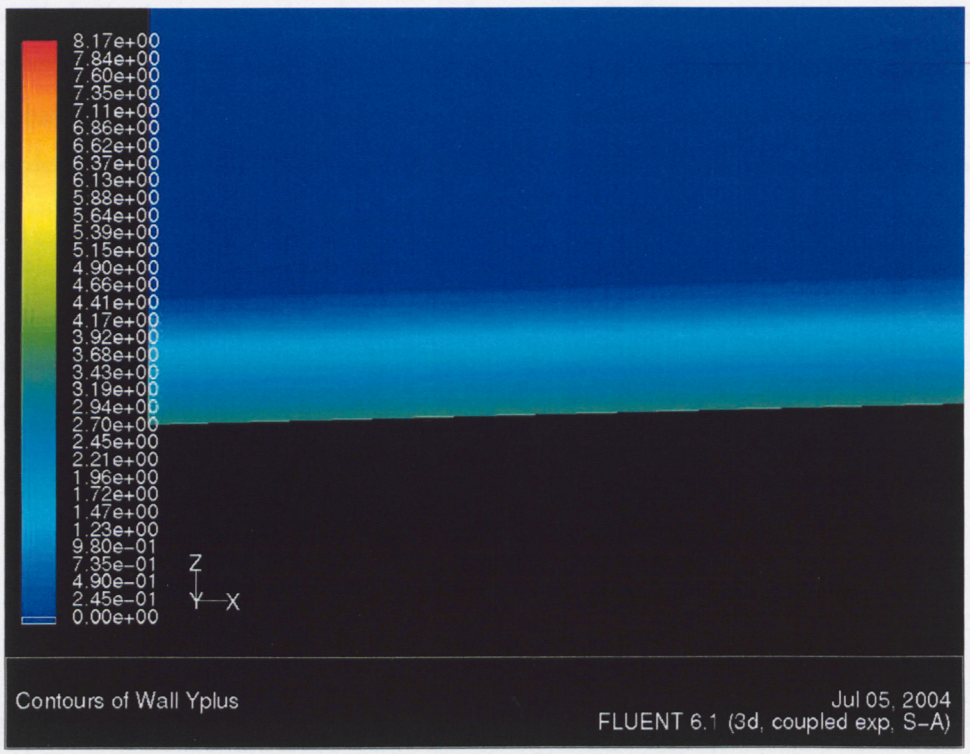

Figure 3.15 Contours of wall Yplus.

With blocks 1 and 2 complete, blocks 3 and 4 were meshed. The grid for blocks 3 and 4 are very simple to create since the majority of grid spacing questions are governed by the meshing of blocks 1 and 2. The connectors that run in the positive and negative z direction in blocks 3 and 4 have the same grid distribution as those in blocks 1 and 2. This is a good example of one of the problems with a structured grid. The remaining z-axis connectors that require a mesh are located at the farfield. Yet because of the nature of a structured grid, tight grid spacing is applied where it is not required. The same can be said of the connectors that run along the x-axis. The remaining x-axis connectors that require meshing are those that are in the farfield; however, these connectors have the same distribution as those connectors in blocks 1 and 2 that run in the x-axis.

The only connectors left that require a grid that the grid density can be controlled on are the connectors that run in the spanwise direction. The layout of the connectors which make up the bottom of block 3 or the top of block 4 are pictured in figure 3.16.

As can be seen, the domain is divided into 3 separate domains, a front wake domain (1), a middle wake domain that contains the wingtip cap (2a, 2b), and a back wake domain (3). Starting with the middle wake domain, the first portion that has to be dealt with is the wingtip cap. The curve that defines the wingtip cap is split into 3 separate connectors. This is done to give the wingtip cap 4 distinct sides to create a structured gird on the cap. The 3 connectors are made up of 2 spanwise connectors and 1 connector that along the chord length of the wingtip. The connectors that run in the spanwise direction have 10 nodes applied to them and are distributed uniformly along the connectors. The connector that runs in the chordwise direction has 100 nodes applied to it and these nodes are distributed in the same fashion as those nodes on the airfoil at the wingtip. The surface grid on the wingtip cap is pictured in figure 3.17.

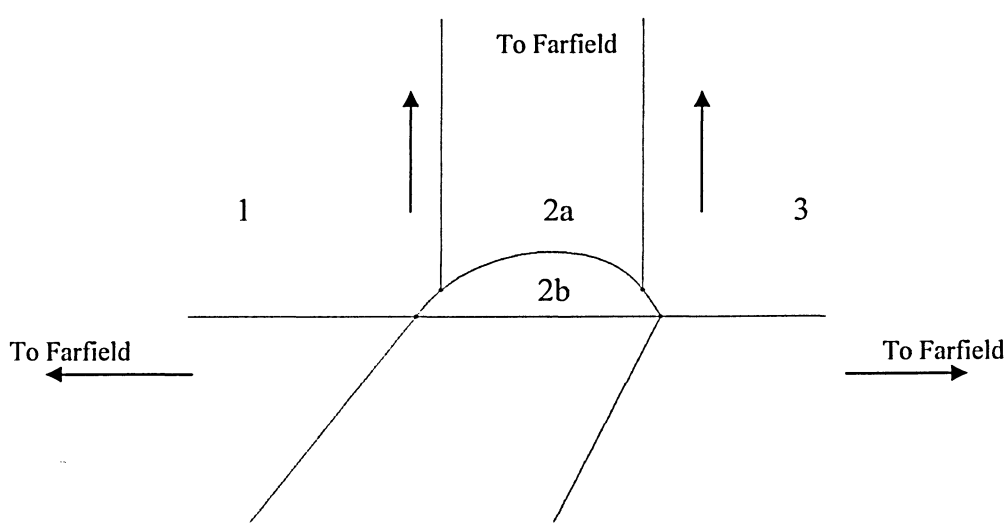

Figure 3.16 Block 3 & 4 Wake domain layout.

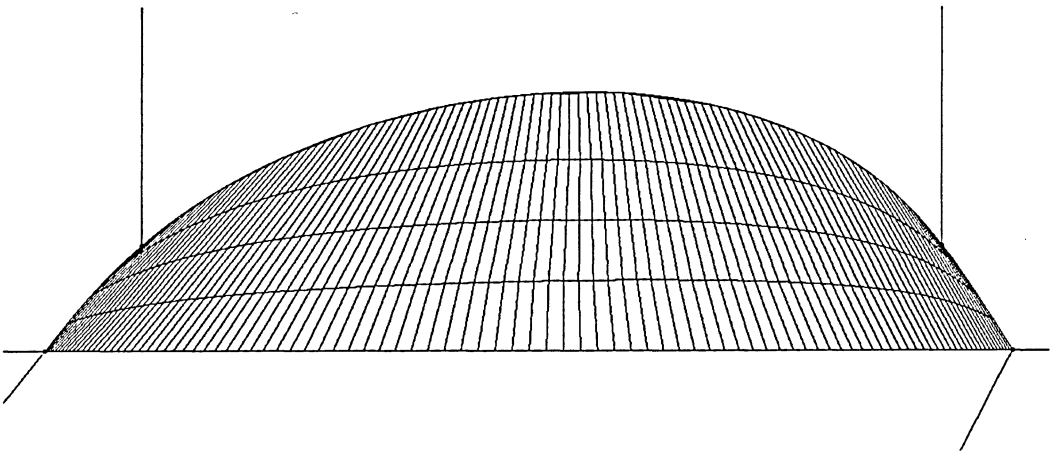

Figure 3.17 Wingtip cap surface grid.

Next the connectors running spanwise at the farfield are split into 2 separate connectors each. This was done in such a way so that one of the connectors lengths matched the length of the spanwise connectors on the wingtip cap. This would allow the gridlines running in the x-direction, from the farfield to the wingtip cap would match, producing a smooth grid. The remaining spanwise connectors running from the wingtip cap out towards the farfield had geometric progression applied to them with increasing node spacing as the nodes approached the farfield. Figure 3.18 and 3.19 shows the completed surface domains.

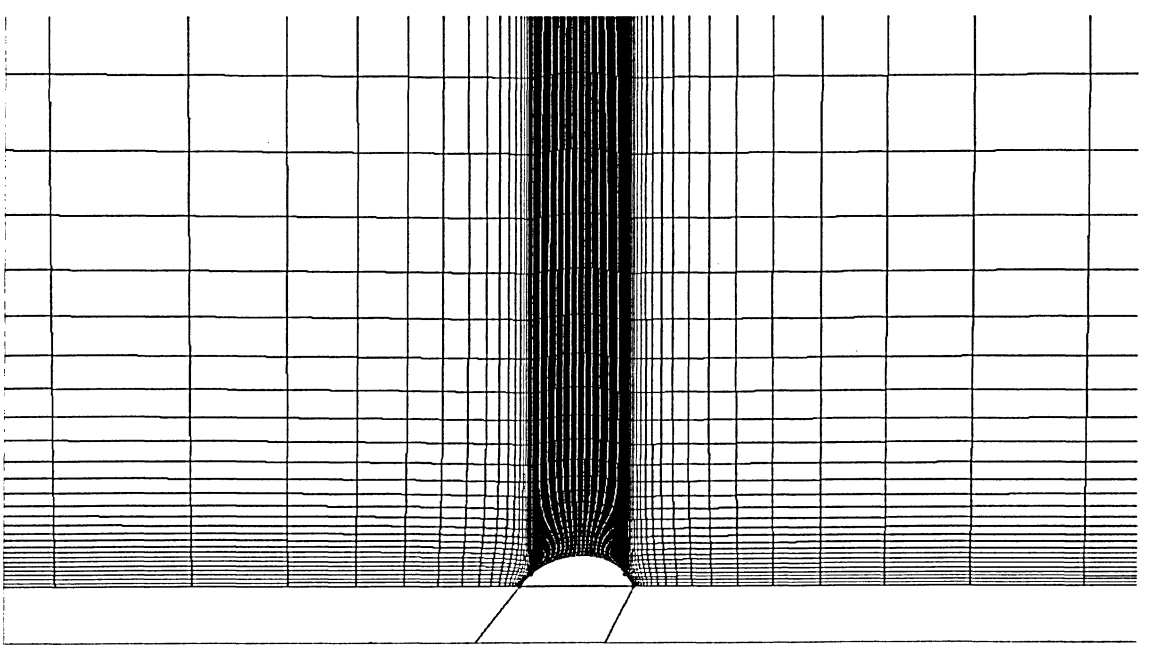

Figure 3.18 Block 3 & 4 wake domains.

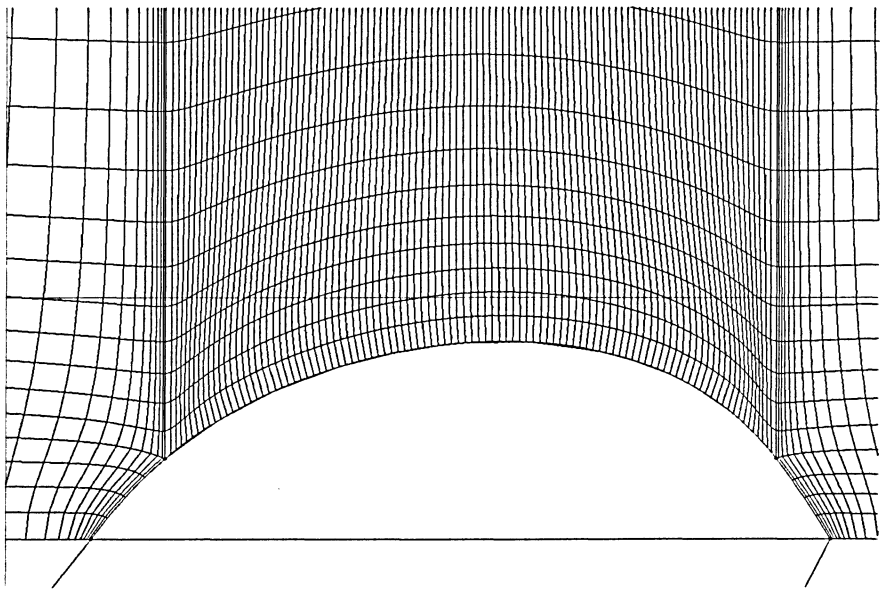

Figure 3.19 Close-Up of wake domain at wingtip cap.

3.5 Grid Smoothing

With all the required surfaces meshed, the next step in the grid generation process is to smooth any grids that require smoothing. Grid smoothing is done to eliminate any skewed elements that may have been produced during the grid generation process. Grid smoothing is also used to reduce asymmetry in the mesh which can help to reduce local truncation errors. An example of this was shown in figures 3.5 and 3.6 in section 3.4, where the grid was required to change direction around the leading edge of the wing. Gridgen has a number of methods for grid smoothing and a number of options for each method. As mentioned in section 3.4, when Gridgen initially produces a grid it uses an algebraic TFI method. Gridgen has a selection of 3 different TFI methods to apply when it produces a grid. The first method, Parametric TFI, is applied when all connectors that define the structured domain are database constrained elements. A database constrained element is a connector or domain that has been constrained to the geometry that has been imported as outlined in section 3.3. This allows Gridgen to produce domains that map to the geometry that has already been created. If Gridgen is unable to apply the Parametric TFI method, it uses the Parametric Fit TFI method, which occurs usually when some of the connectors are database constrained but certain amounts are not and the connectors which aren't are a certain tolerance away from the database entities [22]. The final method that Gridgen applies is the Standard TFI method. Gridgen colors the domain based on the TFI method used. For Parametric and Parametric fit methods the resulting domains are displayed as purple domains in the GUI, if Standard TFI is used the resulting domain is displayed green in the GUI. This can be a very important factor when creating domains as it lets the

user know whether or not a grid is conformed to created CAD data. In this case it is very important since the shape of the BWB wing is complex and therefore having the grid constrained to this shape is important for accurate results. Figure 3.20 shows a color image of the surface grid on the BWB wing and the wake sections and the use of Parametric and Standard TFI methods.

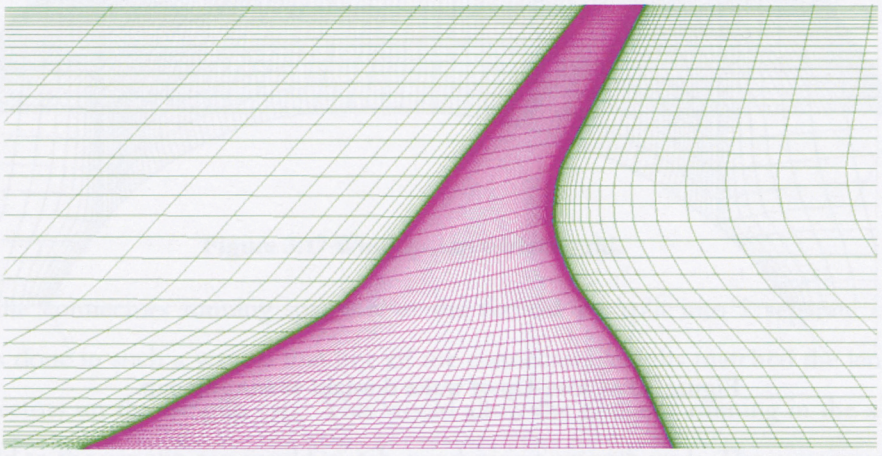

Figure 3.20 Surface grids created using parametric and standard TFI methods.

Other TFI methods can be applied manually and are designed for specific applications. These include Linear, Polar, and Ortho TFI methods and are discussed, including their appropriate applications, in reference [22].

Although Gridgen automatically chooses the most appropriate TFI method for the domain, the resulting grid is not always satisfactory and requires the implementation of Gridgen's grid solver utility. Figure 3.21 shows the initial grid produced by Gridgen using the Standard TFI method; figure 3.22 shows a zoomed in view of the leading edge of the airfoil.

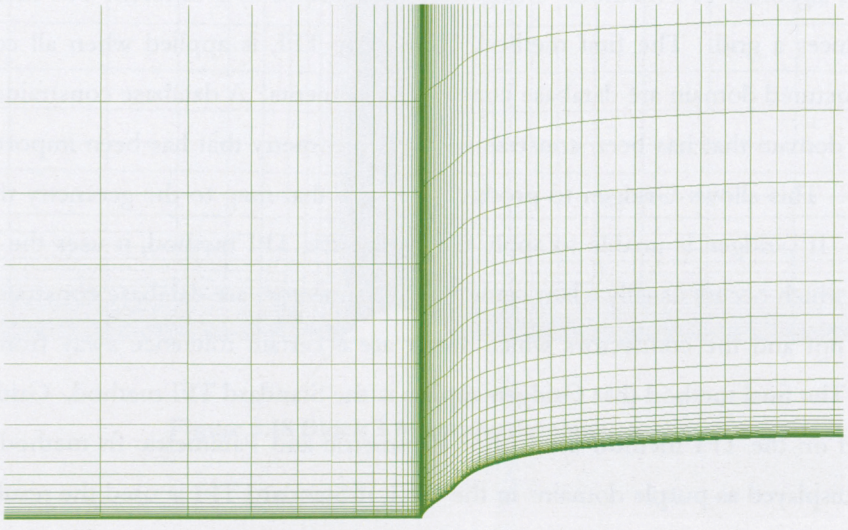

Figure 3.21 Domain created using standard TFI.

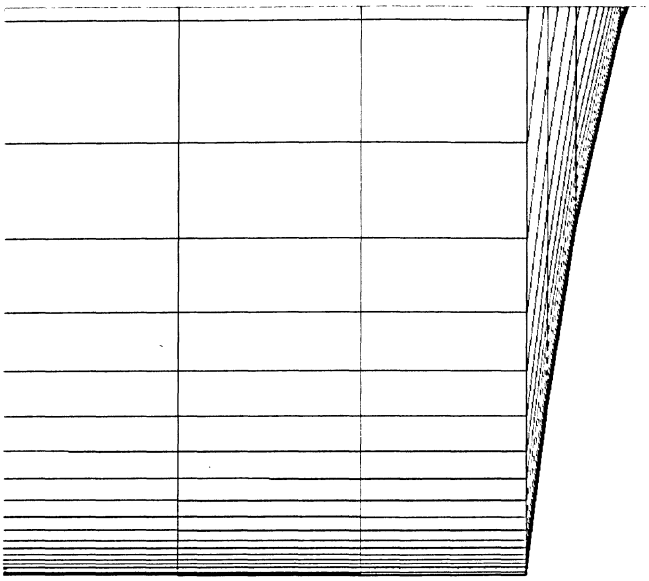

Figure 3.22 View of grid zoomed to region of leading edge.

As is shown in figure 3.22, the grid which is produced using the Standard TFI method produces highly skewed elements in the region of the leading edge where the grid is required to map to a region which has highly changing geometry. Also in figure 3.22 we can see the lack of symmetry in the grid, which as mentioned previously can produce numerical truncation errors. In order to reconfigure these elements and produce a satisfactory grid, Gridgen's grid solver utility must be applied.

Gridgen's grid solver command allows for the refinement of created grids using-elliptic partial differential equation (PDE) methods. Refinement in this case refers to the improvement of grid quality, not increasing the grid size through the insertion of nodes. The elliptic PDE methods allow for the improvement of grid smoothness while maintaining grid clustering and orthogonality. The elliptic PDE solver, when invoked on a grid, iteratively solves a set of PDE's to improve the quality of the grid. Although the full explanation of grid transformations and elliptic grid generation are beyond the scope of this work, the general idea behind elliptic grid generation and the transformations involved will be discussed. Further in depth description of these topics can be found in references [21, 27, 28 and 29]. To start, the general transformation of a grid from the physical plane to the computational plane is governed by Poisson's equation given below for 2D space.

$$\frac{\partial^2 \xi}{\partial x^2} + \frac{\partial^2 \xi}{\partial y^2} = P \qquad (3.2)$$

$$\frac{\partial^2 \eta}{\partial x^2} + \frac{\partial^2 \eta}{\partial y^2} = Q \tag{3.3}$$

Adjustments of the terms P and Q allow for the control of the distribution of the interior grid points. Setting P and Q to 0 yields the unperturbed elliptic equations commonly referred to as the Laplace Equation. Further, if equations 3.2 and 3.3 are inverted so as to make x and y the dependent variables equations 3.4 and 3.5 are obtained. The full derivation of equations 3.4 and 3.5 can be found in reference [21].

$$\alpha \frac{\partial^2 x}{\partial \xi^2} - 2\beta \frac{\partial^2 x}{\partial \xi \partial \eta} + \gamma \frac{\partial^2 x}{\partial \eta^2} = 0 \tag{3.4}$$

$$\alpha \frac{\partial^2 y}{\partial \xi^2} - 2\beta \frac{\partial^2 y}{\partial \xi \partial \eta} + \alpha \frac{\partial^2 y}{\partial \eta^2} = 0 \tag{3.5}$$

Where,

$$\alpha = \left(\frac{\partial x}{\partial \eta}\right)^2 + \left(\frac{\partial y}{\partial \eta}\right)^2$$

$$\beta = \left(\frac{\partial x}{\partial \xi}\right)\left(\frac{\partial x}{\partial \eta}\right) + \left(\frac{\partial y}{\partial \xi}\right)\left(\frac{\partial y}{\partial \eta}\right)$$

$$\gamma = \left(\frac{\partial x}{\partial \xi}\right)^2 + \left(\frac{\partial y}{\partial \xi}\right)^2$$

Equations 3.4 and 3.5 are solved using finite differences through an iterative process, resulting in a transformation from the computational plane to the physical plane. As a result of the use of finite differences to solve equations 3.4 and 3.5, x and y co-ordinates in the physical plane are given in relation to ξ and η co-ordinates in the computational domain. The above equations therefore have no bearing on the governing flow equations that are presented in chapter 4.

Gridgens's elliptic PDE solver has numerous settings that can be adjusted depending on what is required. These options are outlined in the manual [22] and will not be discussed in detail here, simply a few of the options relating to the smoothing of the grids in figures 3.21 and 3.22 will be discussed. Depending on the size of the grid and the initial implementation of the TFI method, there are two attributes that will be most relevant to the grid smoothing process. These are the

Background and Foreground Control Functions. Gridgen uses control functions to control the distribution of the grid points when the Elliptic PDE method is applied. The distribution of the interior grid points are influenced by the Background Control functions, whereas nodes near the grid boundaries are controlled by the Foreground Control functions. There are 3 choices for the Background Control functions, these are Laplace, Thomas-Middlecoff and Fixed Grid. Thomas-Middlecoff is the default BCF as it smoothes the grid while also maintaining the grids orthoganlity and clustering, whereas the Laplace equation smoothes but does not maintain any clustering or orthorganility. The third option, Fixed Grid, is applied only in very specific circumstances when the grid produced using the TFI method is adequate except for any slope discontinuities which are smoothed.

Foreground Control Functions (FCF's) as mentioned previously, are used to control the grid points next to the boundaries of the grid. Specifically they are used to control the orthoganilty, initial grid spacing and the angle between grid points one layer in from the selected boundary while smoothly blending the rest of the interior grid points. One layer in, refers to the first node adjacent to the edge of the domain. Under the FCF command in Gridgen there are several options to control the aforementioned grid aspects. The first option is Form. There are two specific functions that can be applied under Form, the first is the von Lavante-Steger-Sorenson FCF, this FCF allows for a grid that is orthogonal, clustered and smooth. When working with structured grids orthoginality is advantageous as it can help to reduce numerical errors in the solution. This method however loses some of its accuracy in concave regions. The second choice, and Gridgens's default selection, is the Hilgenstock-White FCF. This method maintains all the constraints of the original grid but does not smooth the grid as well as the previous Sorenson FCF. The second option is the spacing constraint. The selections under this option control the initial spacing adjacent from the boundary. The default command is to base the spacing off of the current grid, but selections can be made to adjust this based on what is required of the current grid being smoothed. The third option is the angle constraint. This selection allows the user to control the angle of transverse grid lines that run from the grid boundaries. The default selection is orthogonal, again though the user is able to adjust this setting to suit the needs of the grid. All of the previously mentioned grid options are outlined in reference [21] including examples of comparisons between each method.

There are numerous other settings that can be applied when using the Elliptic PDE methods and can be found in the Gridgen manual [22]. One option of note though is the ability to control the boundary conditions. In this case control of the boundary conditions refers to the ability for Gridgen to control the disbursement of nodes along a domains edge. In most cases the node distribution along the boundary is fixed, and is based on settings that were mentioned previously in the chapter, however Gridgen has the ability to adjust this distribution while refining the grid. Three

selections are given to the user, Fixed (Default), Floating and Orthogonal. The most notable of the three is the orthogonal option. By selecting this option, Gridgen will move the boundary nodes to maintain orthoganlity between adjacent nodes.

In order to smooth the grid in figure 3.22, the only adjustment that was made was to the Foreground Control Function. As can be seen in figure 3.21, the initial grid is adequate in the regions of the grid away from the airfoils leading edge. In order to eliminate the skew elements near the leading edge the boundary edge on the domain that contains the airfoil, pictured as the pink edge at the bottom in figure 3.23, the FCF is switched from Hilgenstock-White, to von Lavante-Steger-Sorenson in order to keep the nodes that are adjacent to the airfoil, orthogonal and clustered.

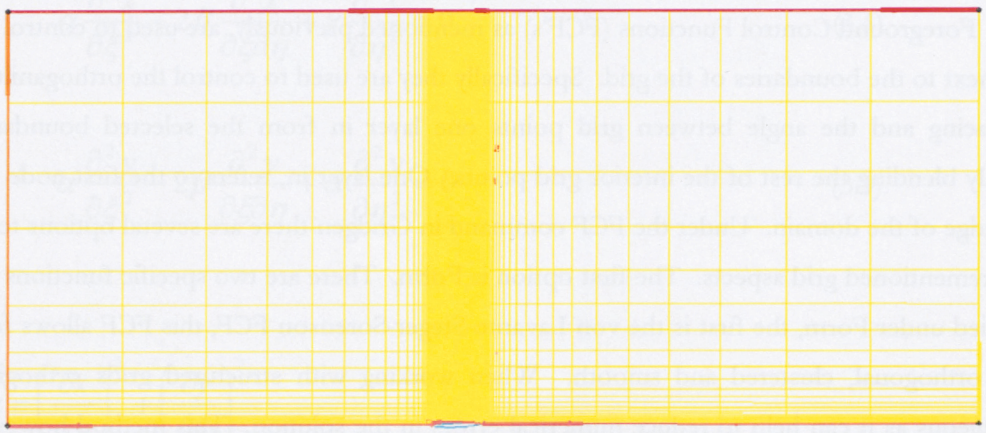

Figure 3.23 Application of Sorenson FCF.

In figures 3.24, 3.25 and 3.26 we see the effects of running the elliptic PDE solver. Also, we can see the difficulties near the concave region at the leading edge. The Sorenson method is unable to keep the nodes constrained to the way that the original grid had them and has to "pull" the nodes out enlarging the initial grid spacing in that region, but maintains the first offwall spacing.

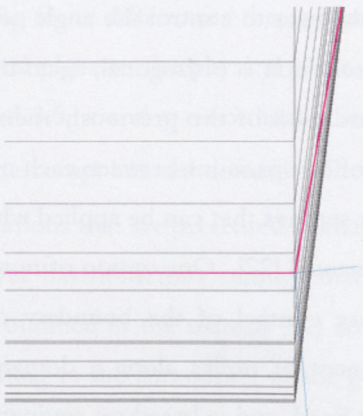

Figure 3.24 Initial grid at leading edge.

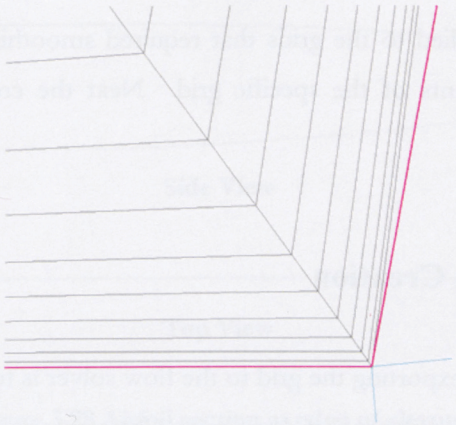

Figure 3.25 50 Iterations of Sorenson FCF.

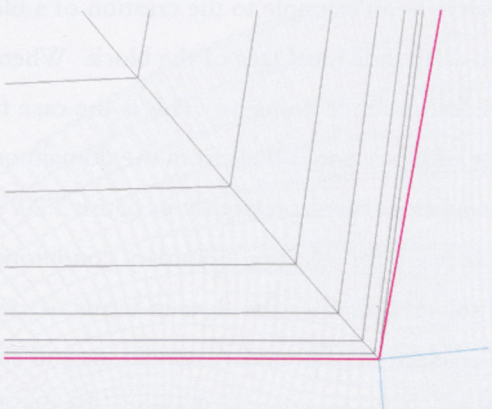

Figure 3.26 200 Iterations of Sorenson FCF.

One thing of note in figures 3.24, 3.25, and 3.26 is the pink line in all three images. This line represents the boundary edge of the domain that the FCF was applied to in figure 3.23. Figure 3.27 shows the finished results of applying the Sorenson FCF to the boundary edge around the airfoil.

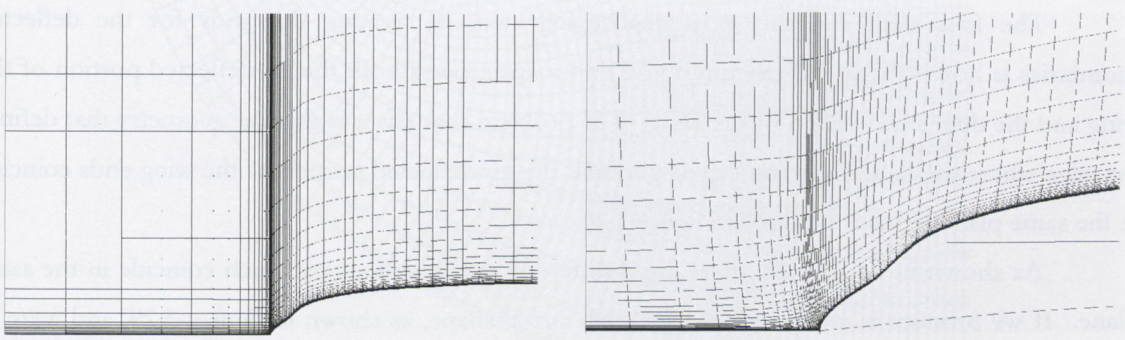

Before **After**

Figure 3.27 Completed application of Sorenson FCF, before and after pictured above.

This process was applied to the grids that required smoothing, adjusting the elliptic PDE options to suit the requirements of the specific grid. Next the creation of structured blocks is discussed.

3.6 Structured Block Creation

The final step before exporting the grid to the flow solver is to build blocks from the created domains. Building a block from structured domains in Gridgen involves the assembly of the 6 faces of the block. Figure 3.4 showed the layout for the un-deflected baseline BWB grid and included 4 distinct blocks. Block 1 will serve as an example to the creation of a block in Gridgen. Each side of the block is selected and saved as an individual face of the block. When selecting one of the six faces of the block it is possible to select multiple domains. This is the case for the creation of the base of block 1 in figure 3.4. The base of block one is built from the domain on the surface of the wing, and the front and rear wake domains as pictured previously in figure 3.20. When all 6 faces are selected Gridgen saves the block and is ready for selecting boundary conditions and the appropriate analysis software. A structured flow solver computes the flow in terms of structured blocks, therefore the block format is necessary. The selection of boundary conditions and analysis software is discussed in a later section. Section 3.8 discusses the creation of the grids for the deflected geometries as well as the geometries with the modified trailing edges.

3.7 Grid Generation for Deflected and Modified Geometries

The first step, and the most challenging step, in creating the grids for the deflected geometries is how to create a structured grid that maps around both the un-deflected portion of the wing and the deflected portion of the wing. The problem that arises is that the geometry that defines the edge where the deflected geometry begins and the un-deflected portion of the wing ends coincide in the same plane. This is pictured in figure 3.28.

As shown in figure 3.28, there are 2 different airfoil geometries which coincide in the same plane. If we produce a structured grid for each airfoil shape, as shown in figures 3.29, and were to then overlap the two grids, there would be regions in the grid where grid points do not match up.

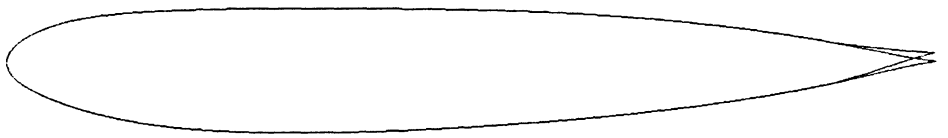

Side View

Top View

Figure 3.28 Airfoil section at edge of elevon.

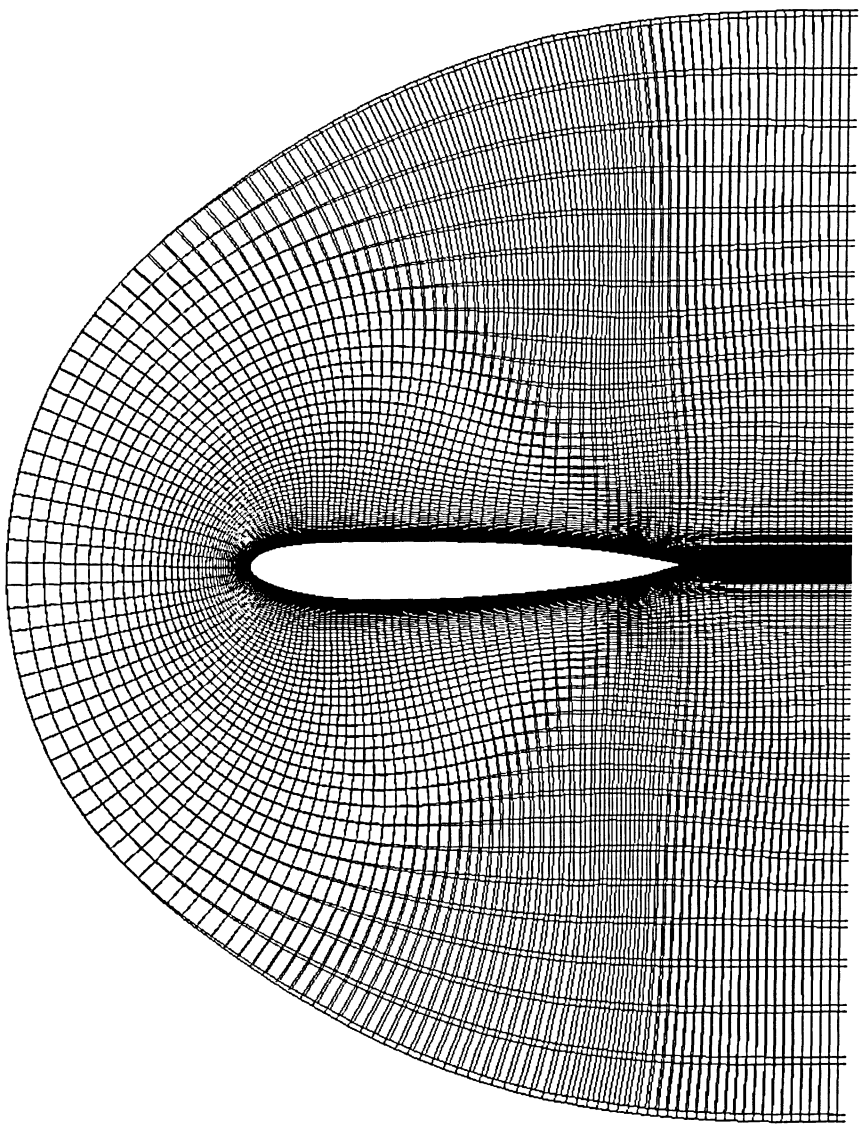

Figure 3.29 Two C-Grids around each airfoil shape.

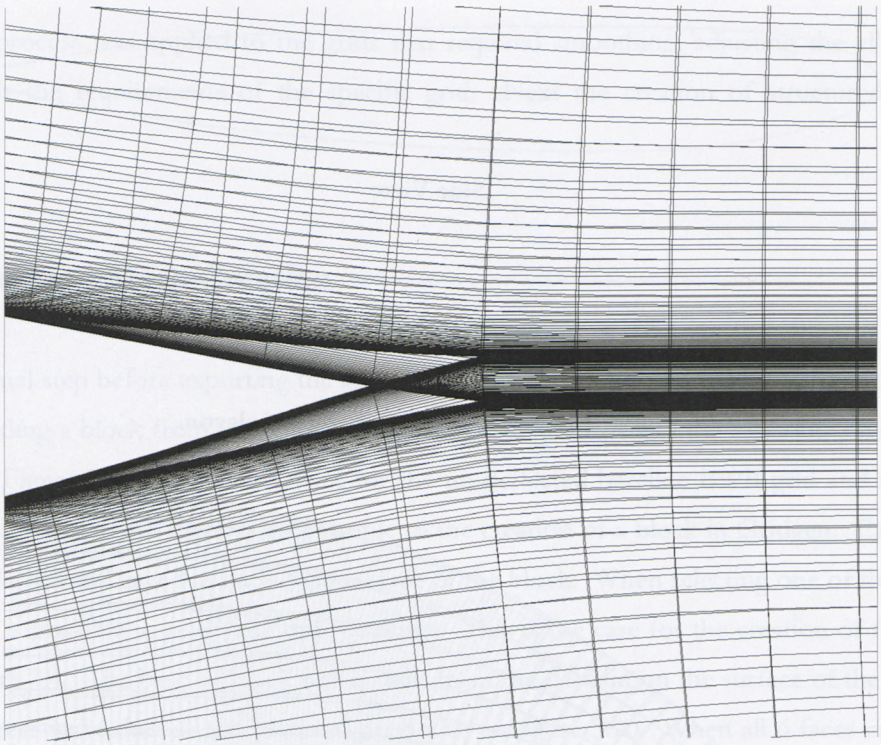

Figure 3.30 Overlap of C-Grids in the region of the trailing edge.

Figure 3.30 shows the overlap of the two grids in the region of the trailing edge. Work done by Tarhan, and Oktay [30] involves the use of overset grids, better known as Chimera grids in the analysis of 2-D airfoil flap systems. Figure 3.31 shows the use of Chimera grids in the analysis of wing flap systems similar to the work of Tarhan and Oktay.

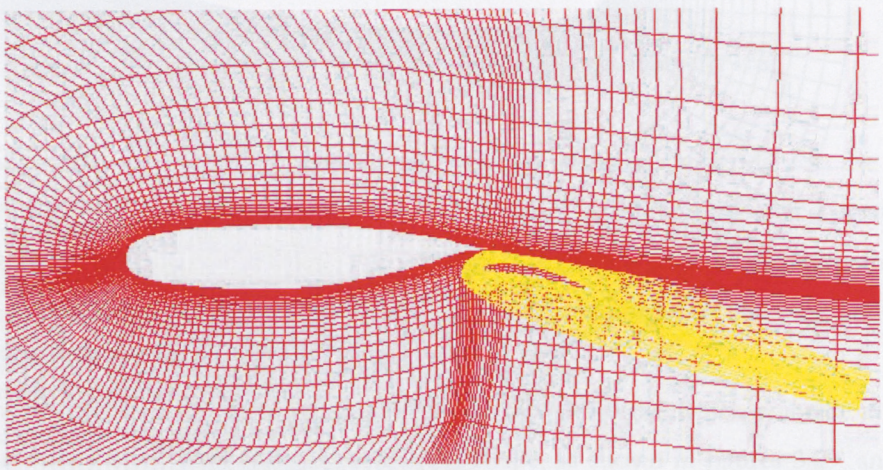

Figure 3.31 Example of Chimera grid in the Analysis of an airfoil and flap. [31]

Before the flow solver software starts the iterative process, it isolates the grid points that are intergrid points, those that don't match up through the overlapping of two different grids, and applies an interpolation method to these points to allow for the flow solver to continue. Their

results through the application of Chimera grids show accurate results as compared to single block and multi-block methods as well as experimental results.

Fluent and Gridgen are unable to use Chimera grids so alternate methods are required in order to produce a grid around the deflected geometries. Numerous methods and ideas were explored to try and produce a structured grid that would be able to accurately model the viscous effects on the deflected elevon. However, no solution was found and unstructured grid methods were examined. It was decided that an unstructured block would be used around the portion of the wing with a deflected elevon. This would allow the production of structured blocks around the rest of the BWB wing with only a small unstructured block around the deflected elevon.

The first step was to size the block that would surround the deflected elevon. The sides of block were extended to the airfoil sections adjacent to the edge of the elevon. The front and back of the block were sized to allow for development of the unstructured grid around the elevon, while the height of the blocks was sized again to allow for proper development of the unstructured grid within the block. Figure 3.32 shows the unstructured blocks surrounding the elevon, with the upper block colored red, the lower block colored blue. The connectors that define the wing are green and the elevon connectors are colored black.

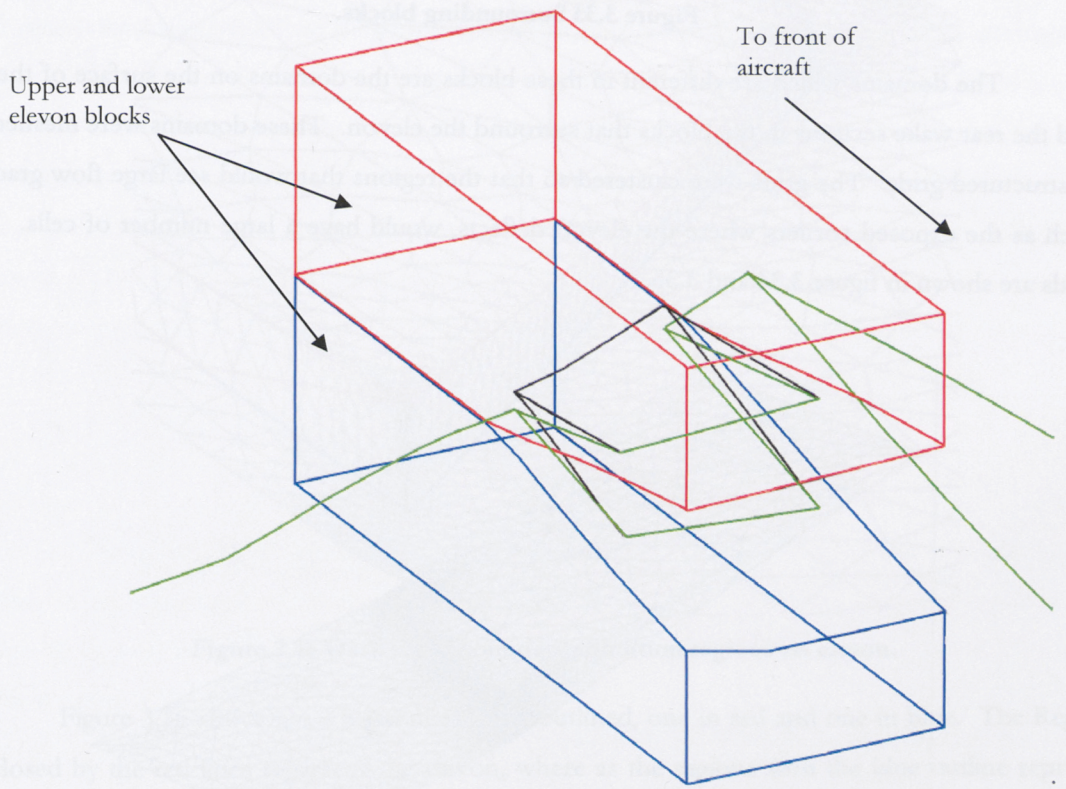

Figure 3.32 Unstructured blocks surrounding deflected elevon.

From this point, domains need to be created on the exterior edges of the blocks to make up the sides of the blocks that surround these two blocks. When working with structured grids, if a block is segmented into multiple blocks the mesh on the adjacent blocks must all match in order to maintain the structured grid. Figure 3.33 shows the blocks that have been produced, segmenting the larger single block from the original grid, the colored lines outline the domains that makeup these blocks.

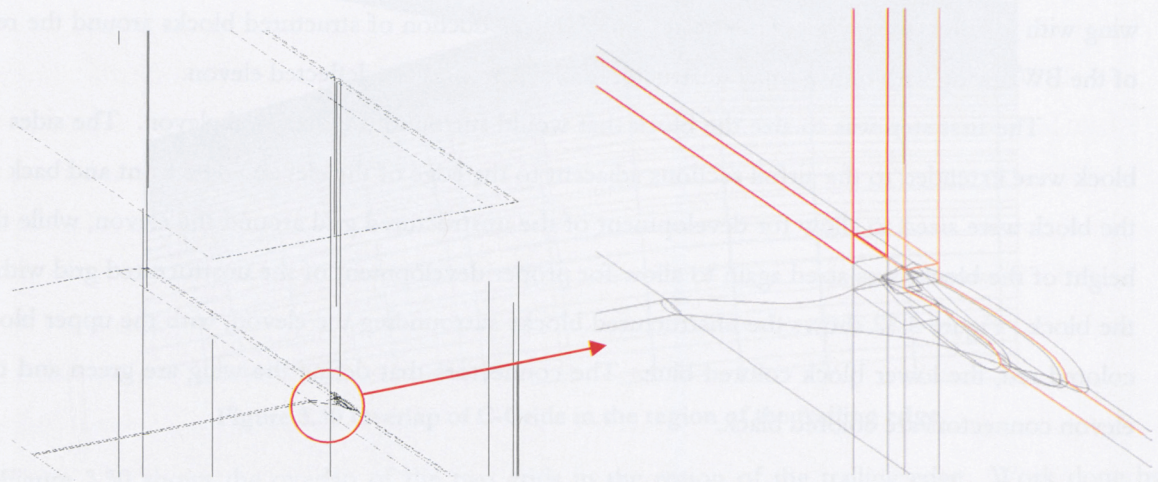

Figure 3.33 Surrounding blocks.

The domains which are different in these blocks are the domains on the surface of the wing and the rear wake sections in the blocks that surround the elevon. These domains were meshed with unstructured grids. The grids were clustered so that the regions that would see large flow gradients, such as the exposed corners where the elevon deflects, would have a large number of cells. These grids are shown in figure 3.34 and 3.35.

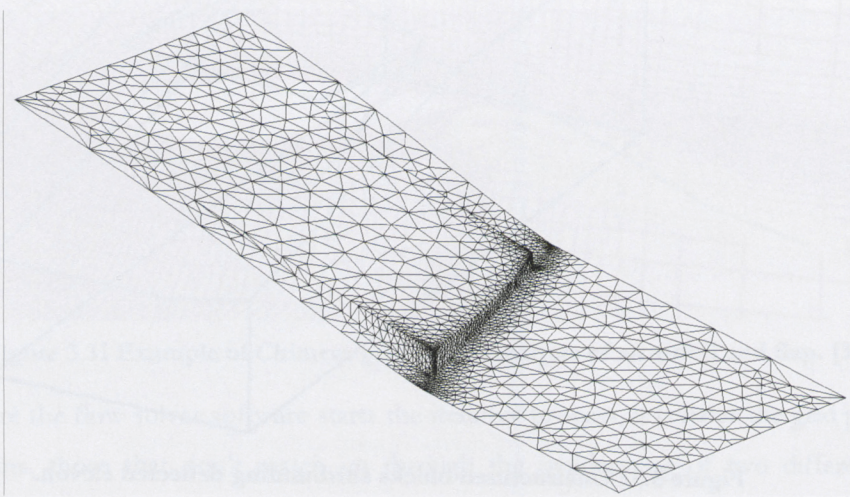

Figure 3.34 Unstructured grids on elevon and wake domains.

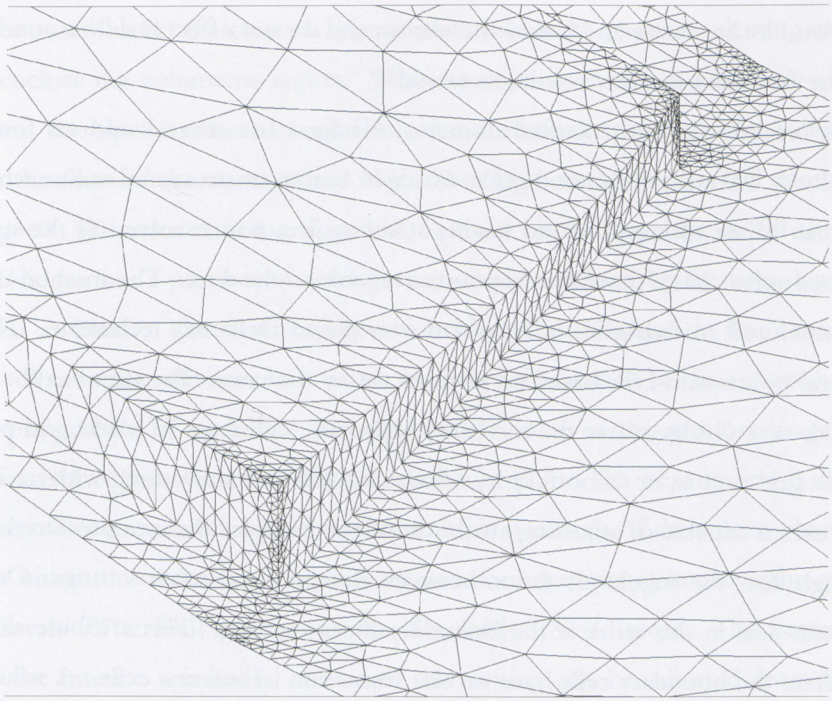

Figure 3.35 Unstructured grids on elevon edge.

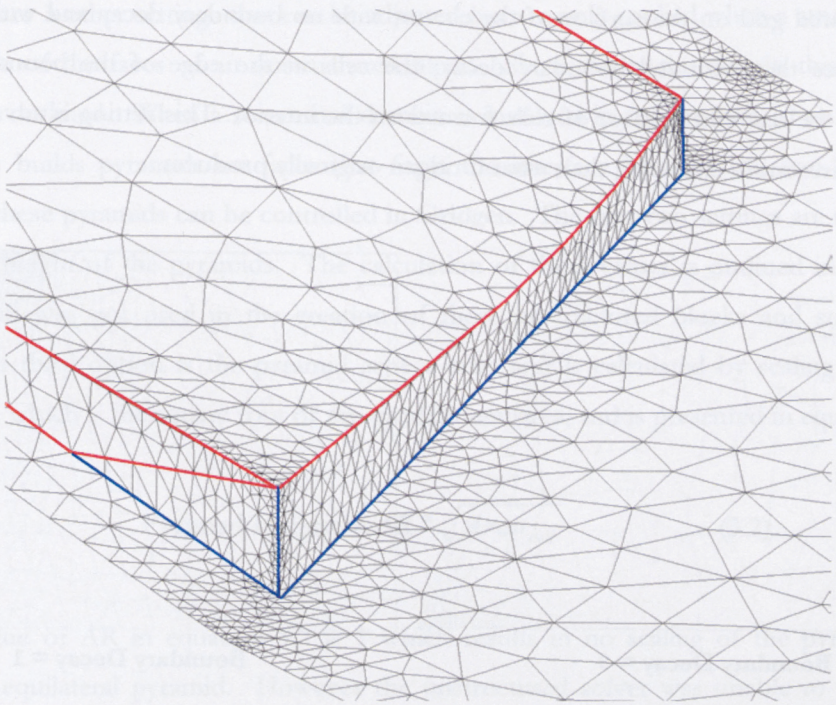

Figure 3.36 Outlines of boundary condition regions on elevon.

Figure 3.36 above has 2 separate regions outlined, one in red and one in blue. The Regions enclosed by the red lines represent the elevon, where as the regions with the blue outline represent block interface boundary conditions. The selection of boundary regions will be discussed later in section 3.10, for now the reader should understand that these regions in blue are the interface meshes

between the two blocks, above and below the elevon and do not affect the flow conditions such as a wall or pressure far field boundary condition would.

When creating the unstructured domains, Gridgen has several options for improving the initial grid created. Like the structured grids, Gridgen has an unstructured solver which has settings that the user can adjust to improve grid quality. Although not as involved as the structured solver, the unstructured solver has a number of options available to the user. The method used by Gridgen to create unstructured surface grids is based on a modified Delaunay technique. This involves the insertion of grid points into cells based on options set by the user. The user has the ability to either refine, in which case Gridgen uses the modified Delaunay technique to insert grid points, decimate, which removes grid points, or smooth only, which uses LaPlace smoothing with no insertion of grid points. The user is capable of adjusting attributes of the triangles that are produced such as the min and max triangle size, the angular deviation between elements and other settings. One setting which was used a great deal in this work is the Boundary Decay setting. This attribute allows the user to control the effect the boundary cells have on the formation of interior cells. A value of 0 turns the feature off while a value of 1 applies full boundary influence on the interior cells. Figure 3.37 shows the unstructured grid on the surface of the elevon with no boundary decay and with full boundary decay. Notice that with full boundary decay, the cells at the edge of the boundary have more influence on the size and number of cells formed on the interior. This setting is advantageous when the grid requires more clustering than what Gridgen originally produces.

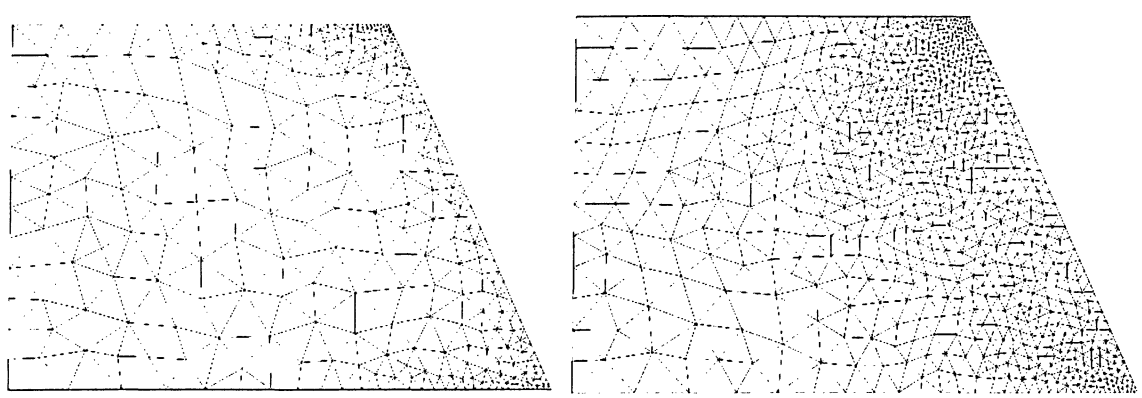

Boundary Decay = 0 **Boundary Decay = 1**

Figure 3.37 Comparisons of boundary decay settings.

3.8 Unstructured Block Creation

Creation of Unstructured blocks is very different from the creation of structured blocks. Whereas the creation of structured blocks required the definition of 6 distinct faces that would make

up a proper structured block, the creation of unstructured blocks requires selecting enough meshed faces that will enclose the volumetric region. When creating a structured grid, once all 6 faces have been selected and the block has been saved Gridgen automatically produces the 3-dimensional grid. However, once the faces of the unstructured block have been saved there is still another step to the process. Gridgen's 3D unstructured grid generator must be run in order to fill the unstructured block. Again Gridgen has a number of settings that can be adjusted by the user depending on the specific problem at hand. The first setting which has to be adjusted is the Tetrahedral Solver Memory Limit. This setting allocates how much memory will be used by the solver and is limited to the amount of physical RAM available. An approximate value of the memory usage of Gridgen's tetrahedral solver is 1 MByte for every 15,000 tetrahedra [22]. The next setting is the number of iterations for the solver to run and is used to run multiple iterations of the solver when a poor mesh results from the initial run of the generator. Each iteration attempts to improve the quality of poor regions in the mesh. The final attribute is the Tetrahedral Size Factor. This setting adjusts the relative size of the interior tetrahedral elements, this setting can be adjusted from 0 (small) to 1 (large).

There are 3 other settings that can be adjusted but are only applied when a structured grid is included as one of the faces of an unstructured block. Since this is the case in this block, these settings will be outlined. When a structured domain is involved in the creation of an unstructured block, Gridgen builds pyramids on faces that form the interface between the two blocks. The production of these pyramids can be controlled in Gridgen. The first two settings are the minimum and maximum height of the pyramids. The calculation of these values is outlined in the Gridgen manual [22] and was not used in the creation of these unstructured blocks and so will not be discussed. The third option is the pyramid aspect ratio and is calculated by scaling the nominal pyramid height, which is the square root of the quadrilateral area, and is presented in equation 3.2.

$$\text{Pyrimad Height} = AR * \sqrt{Area_{cell}} \qquad (3.2)$$

The default value of AR in equation 3.2 is 1 which results in no scaling of the pyramid height, resulting in an equilateral pyramid. However the unstructured solver was unable to create a grid because there were intersecting edges in the corners of the block where the two structured grids meet shown in figure 3.38.

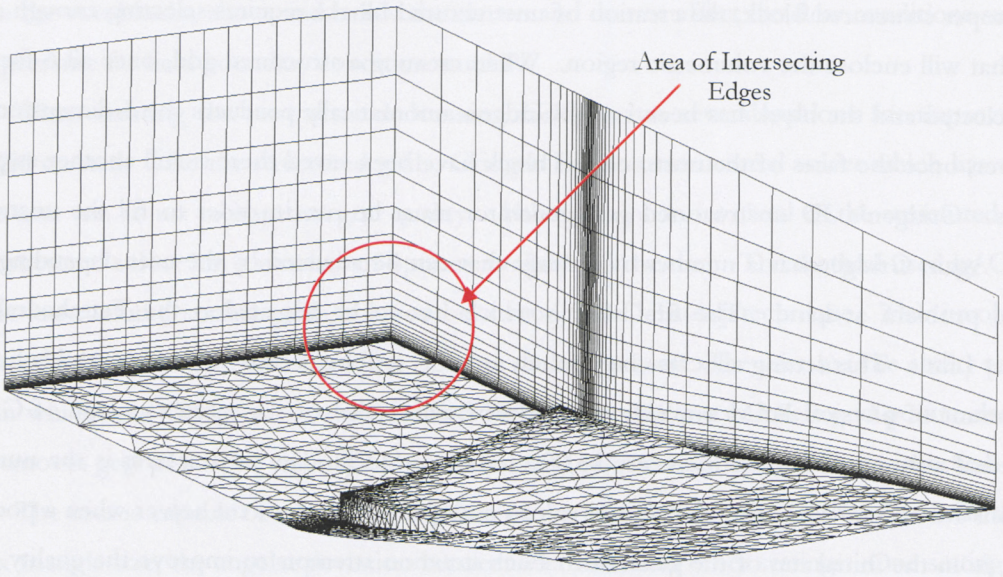

Figure 3.38 Structured domains on unstructured block.

In order to eliminate these intersecting edges the value of AR in equation 3.2 was set to 0.125 in order to produce an unstructured grid. This process was completed for the block underneath the wing surrounding the portion of the deflected elevon. With the two unstructured grids complete, the rest of the structured grids were produced in the same fashion as the grids for the baseline un-deflected geometry. From this point the grid is ready for selection of boundary conditions and analysis software.

3.9 Selection of Analysis Software and Boundary Conditions

With all blocks completed the next step is to select the analysis software to be used and the boundary conditions to be applied. Selecting the desired flow solver will allow Gridgen to format the output mesh such that it can be loaded in to the desired flow solver. Although it is possible to change the flow solver at anytime during the grid generation process, any boundary conditions that have been set will be erased. For this work Fluent 6.0 is the flow solver being used, by selecting Fluent from the selection of flow solver this opens the option of applying boundary conditions that are compatible with Fluent. The boundary conditions in this case are very simple to apply and will be discussed in depth in chapter 4. Figure 3.39 and 3.40 are colored based on the boundary conditions applied. The blue domains are Pressure Far-Field, the orange are Symmetry and the purple are wall boundary conditions.

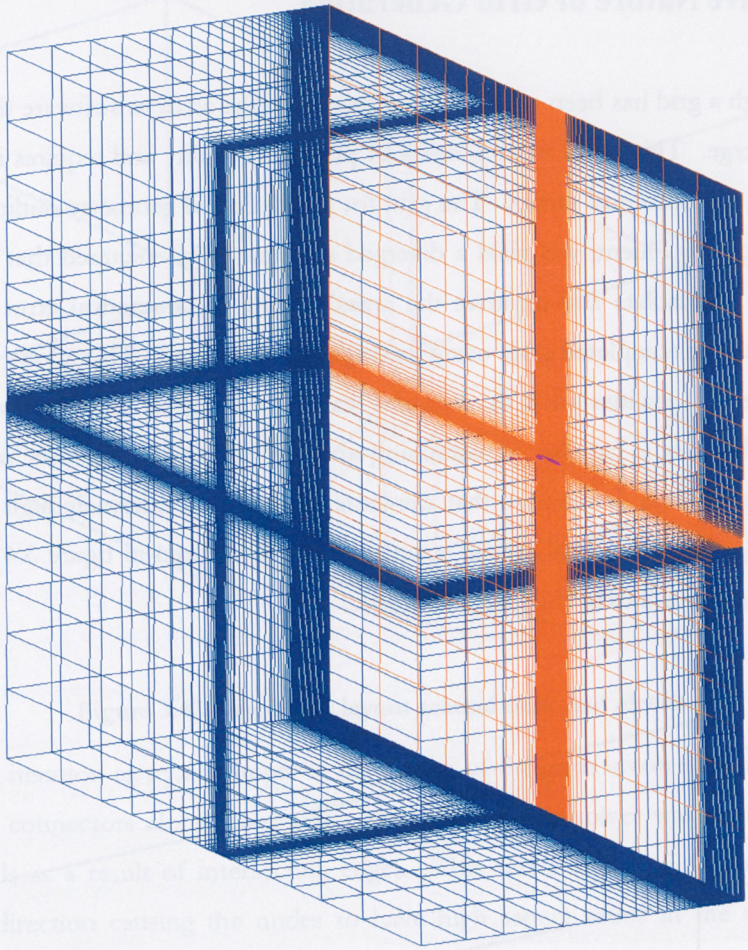

Figure 3.39 Domains with pressure far field and symmetry boundary conditions.

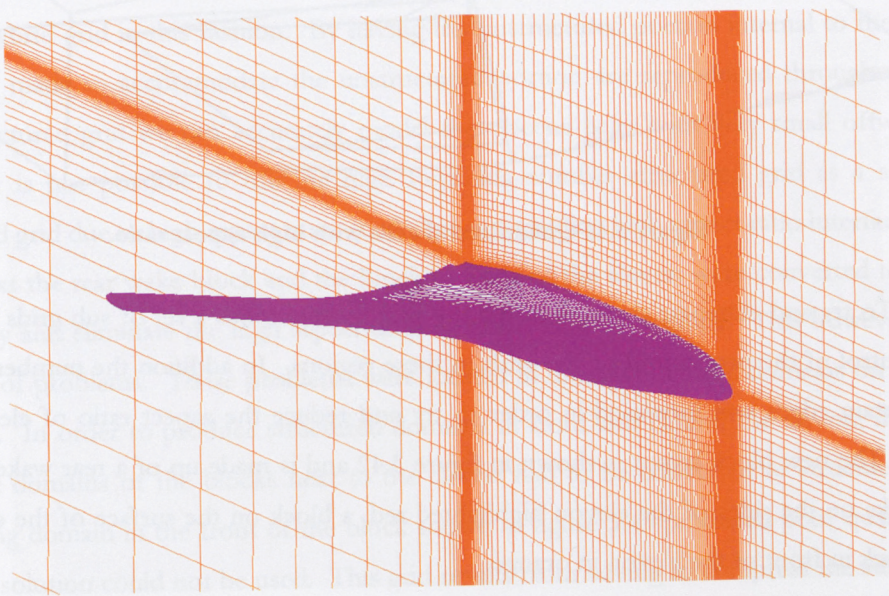

Figure 3.40 Domains with symmetry and wall boundary conditions.

3.10 Iterative Nature of Grid Generation

Although a grid has been successfully exported to the analysis software the resulting solution process can diverge. This tends to be a result of poor grid quality and requires isolating the regions that are causing the numerical errors. The grid for the deflected geometry outlined above, although successfully output to Fluent, will yield a diverged solution. This required that the original grid be examined to try and isolate and improve the areas causing the numerical errors. Gridgen has the ability to examine the completed grids using its diagnostic functions. This allows the user to examine the grid for specific qualities such as skewness values, and aspect ratio values. There are other quantities that the user is capable of examining and are outlined in the user manual [22]. In the unstructured block it was determined that elements existed with extremely high aspect ratios in the region of the edges near the first offwall spacing. This is pictured in figure 3.41 with the elements with aspect ratios above 5.0×10^6 highlighted in red.

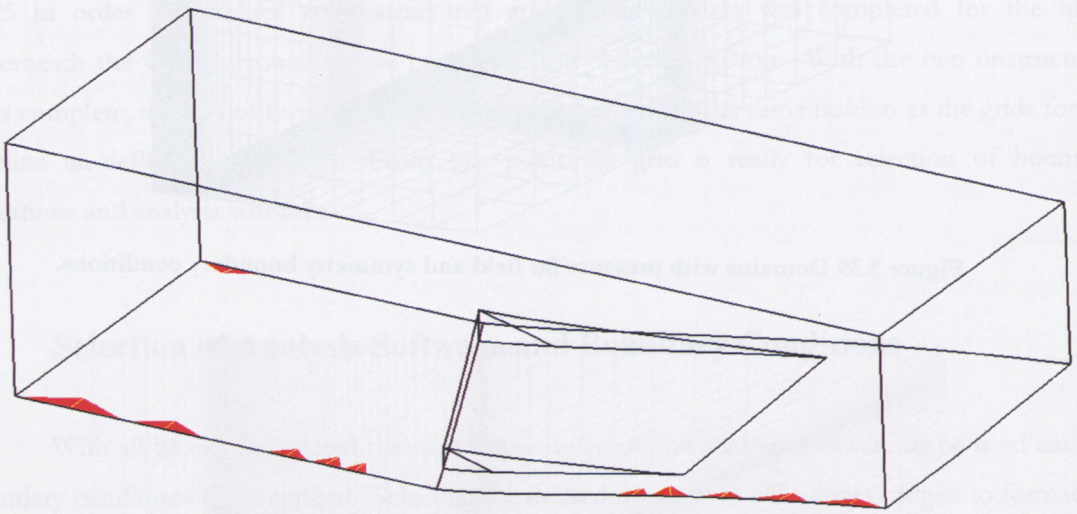

Figure 3.41 Quadrilateral cells with high aspect ratio.

To try and eliminate these elements the grid was split into a set of sub grids to try and gain more control of the production of the grids in these regions. In addition the number of grid points along certain edges was increased in order to try and reduce the aspect ratio of elements in these regions. The new block layout is shown in figure 3.42 and is made up of a rear wake block in blue, two blocks on the sides of the elevon highlighted red, a block on the surface of the elevon in green and a block in front of the elevon in orange.

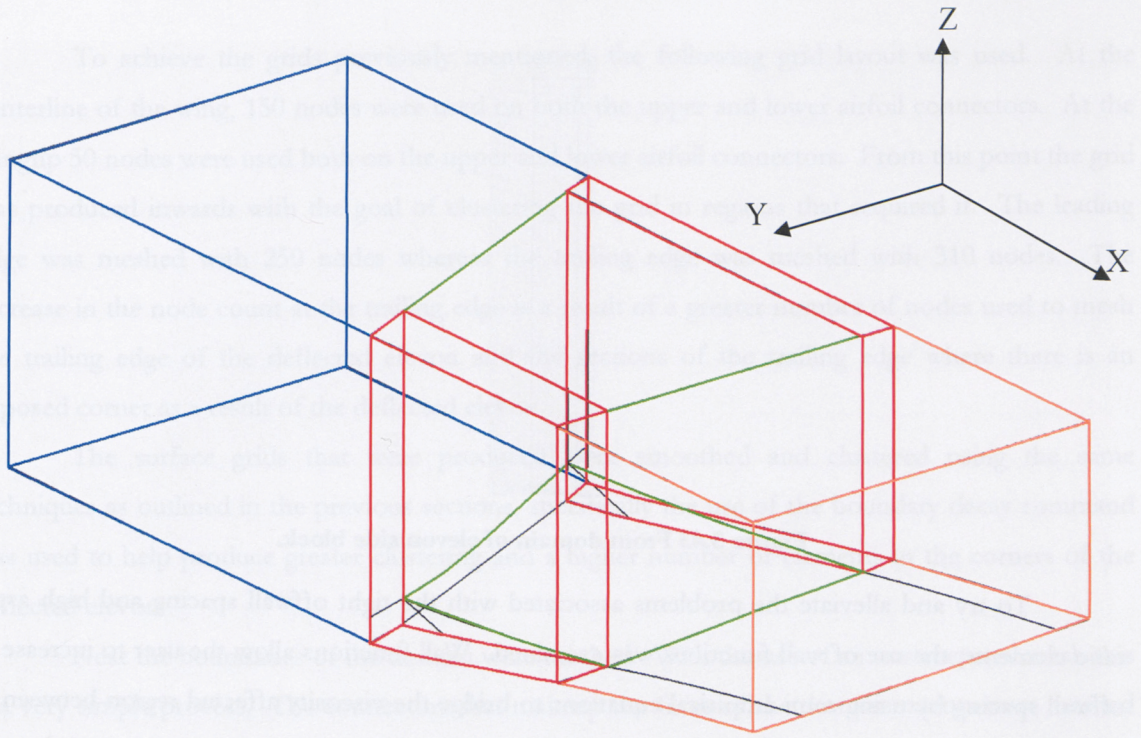

Figure 3.42 New block layout around deflected elevon.

The first iteration to try and improve the quality of the grids involved increasing the number of nodes on the connectors along the x-axis. The unstructured solver was unable to produce the unstructured grids as a result of intersecting edges. This was a result of the increase in the node count in the x direction causing the nodes to have high aspect ratios in the z-axis. To try and alleviate this problem the node count was increased in the z-axis. This was unsuccessful, and caused an increase in the node count beyond the resources available. This highlights the problem of trying to build a hybrid grid in this fashion. By having the unstructured portion internal to the structured, adjustments made to accommodate the unstructured portion are reproduced throughout the grid. With a structured grid we can accurately model the viscous layer with very small offwall spacing. However, it is not possible to use the high Reynolds number structured grid as a seed for the unstructured grid due to high aspect ratio quad elements yielding high aspect ratio interface pyramids.

Next the rear wake block and the block in front of the elevon were converted to structured blocks to try and eliminate the high aspect ratio elements in these regions. This however produced its own set of problems. These problems were located in the unstructured domains on the sides of the elevons. In order to produce structured domains in front and behind the elevon, the front and back of the domains of the blocks next to the elevon had to be converted to structured domains. The resulting domain in the front of the block shown in figure 3.43 produced poor quality elements and so this solution could not be used. This grid results from having to compress the structured grid along the side of the deflected elevon.

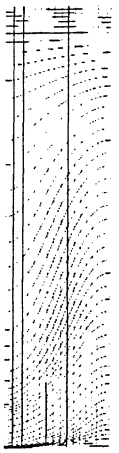

Figure 3.43 Front domain of elevon side block.

To try and alleviate the problems associated with the tight offwall spacing and high aspect ratio elements, the use of wall functions was examined. Wall functions allow the user to increase the offwall spacing by using semi-empirical equations to bridge the viscosity affected region between the wall and turbulent region [32]. However, a proper unstructured grid was unattainable and the node count increased with every try to produce an unstructured block beyond both the scope of Fluent's wall functions and the computational resources.

The next solution was to try a fully unstructured grid. The first major concern with selecting a fully unstructured grid is the fact that there is no control over the production of the grid within the boundary region and so becomes problematic when trying to model viscous effects using either the near wall method or wall function. With a fully unstructured mesh the cases would first be run using Fluent's inviscid solver to a converged solution and then the viscous solver would be turned on and the solution would be run to a converged solution.

With a fully unstructured grid the need for a multi-block grid, as was used for the previous grids, is eliminated. The only surfaces that need to have a grid produced on them are the surface of the wing and extents of the boundary. The upper and lower surfaces of the BWB were meshed with 13339 and 13198 triangular elements respectively. The connector layout for the positive deflection baseline BWB is shown in figure 3.44.

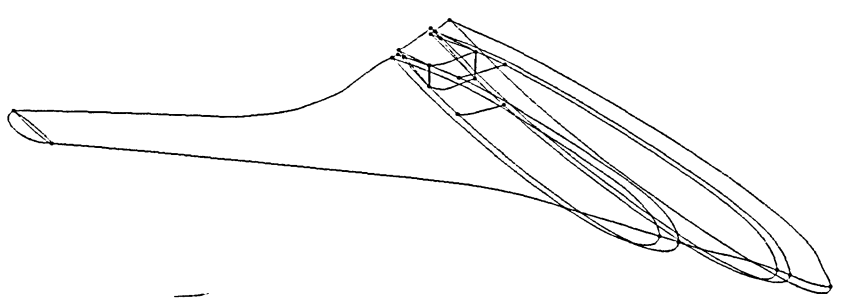

Figure 3.44 Connector layout for deflected geometry.

To achieve the grids previously mentioned, the following grid layout was used. At the centerline of the wing, 150 nodes were used on both the upper and lower airfoil connectors. At the wingtip 50 nodes were used both on the upper and lower airfoil connectors. From this point the grid was produced inwards with the goal of clustering the grid in regions that required it. The leading edge was meshed with 250 nodes whereas the trailing edge was meshed with 310 nodes. The increase in the node count at the trailing edge is a result of a greater number of nodes used to mesh the trailing edge of the deflected elevon and the sections of the trailing edge where there is an exposed corner as a result of the deflected elevon.

The surface grids that were produced were smoothed and clustered using the same techniques as outlined in the previous sections, specifically the use of the boundary decay command was used to help produce greater clustering and a higher number of elements in the corners of the deflected elevon.

Next the boundaries of the domain were meshed. With the use of an unstructured mesh this is a very simple process. The connectors that makeup the faces of the domain extents were meshed with 25 nodes each. A coarse mesh such as this is acceptable in this case as the gradients in the flow properties at the farfield are small or non existent.

One of the first problems that was encountered with the unstructured mesh was located in the corners where the elevon deflects and the un-deflected and deflected portion of the wing meets, this is pictured in figure 3.45 and 3.46.

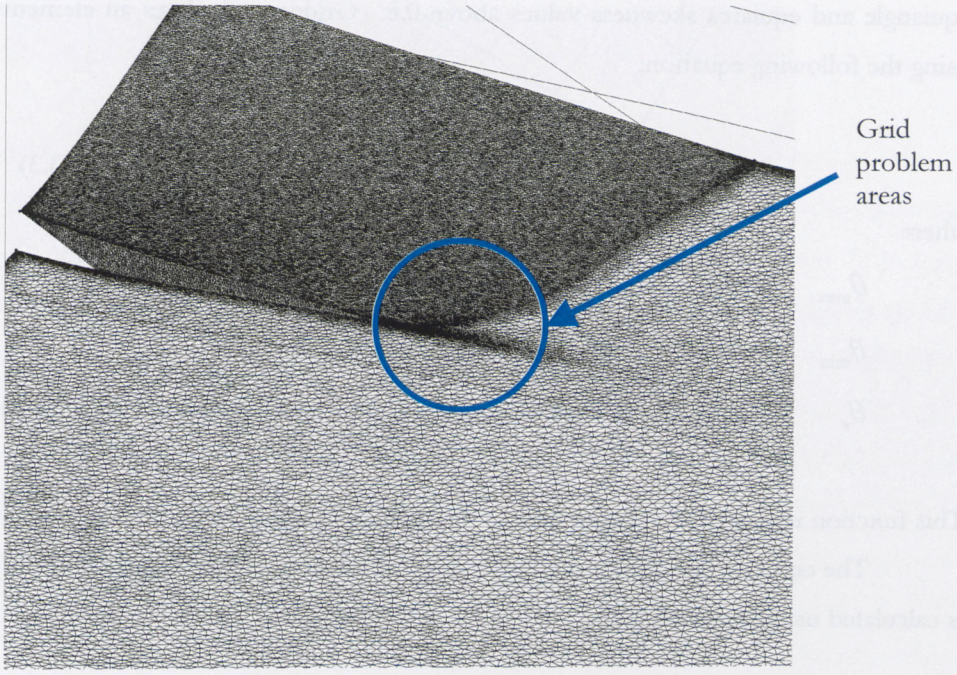

Figure 3.45 Area with problematic grid elements.

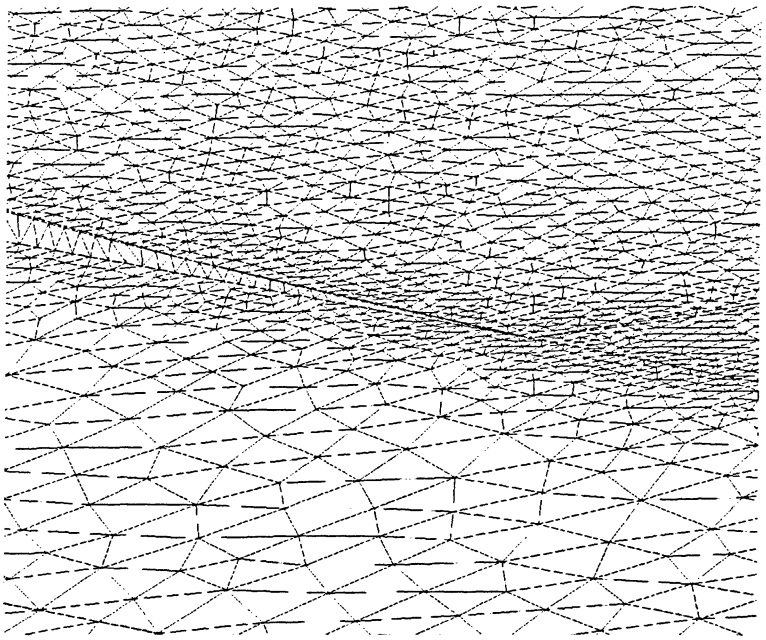

Figure 3.46 Enlarged view of elevon corner highlighted in figure 3.45.

The problem that arises is that the elements that are produced in this region are above the limits that Gridgen is able to work with when trying to produce an unstructured block. This resulted in the block solver encountering errors when trying to produce the 3-dimensional elements in this region. Contact was made with Gridgen's technical support to try and determine how to correct this problem. Their solution was to examine the grids and eliminate any areas in the grid that had equiangle and equiarea skewness values above 0.8. Gridgen calculates an elements equiangle value using the following equation;

$$\max[(\theta_{\max} - \theta_e)/(180 - \theta_e), (\theta_e - \theta_{\min})/\theta_e] \qquad (3.3)$$

where

$\theta_{\max}$ = largest angle in the cell in degrees

$\theta_{\min}$ = smallest angle in the cell in degrees

θ_e = angle for an equilateral element (60° for a triangle 90° for a quad)

This function represents the angle ratio of the included angle compared to an equilateral angle.

The equiarea or equivolume, depending on the type of elements (2D or 3D) being examined, is calculated using equation 3.4.

$$\text{(Optimal Cell Size} - \text{Actual Cell Size)/(Optimal Cell Size)} \qquad (3.4)$$

where the Optimal Cell Size is the area (2D) or volume (3D) of an equilateral cell with the same circum radius as the actual cell. This equation represents the ratio between the actual cell volume/area to the optimal cell volume/area and is only applicable to triangles and tetrahedral elements in Gridgen.

To try and eliminate the problems with the equiangle and equiarea values in these regions, the number of nodes on the connectors that make up this region were increased to try and reduce the values, however no acceptable solution was achieved. To eliminate this problem the solution was to separate the sides of the elevon from the BWB by introducing a gap on each side of the elevon.

No material is currently available on how to size a gap next to a control surface and no data specifically exists on whether or not there is actually a gap next to the elevon in the case of the BWB. Therefore the sizing of the gap was not based on any known data. However in actuality some finite gap would be found at the edges of the elevon to allow for a smooth transition from un-deflected to deflected state. The gap was spaced so as to allow for an accurate unstructured grid to be produced as well as so not to introduce any significant error into the problem. Rather then go back to the CAD data and introduce the gap, Gridgen's domain split command was used to produce the gaps next to the elevon. First a structured grid was produced on the elevon, as the domain split command is only available for structured domains. Next the grid on the connectors that run in the spanwise direction on the elevon was adjusted so that the first node spacing was set to 0.5. From this point the grid was split along the first gridline running in the chordwise direction shown in figure 3.47.

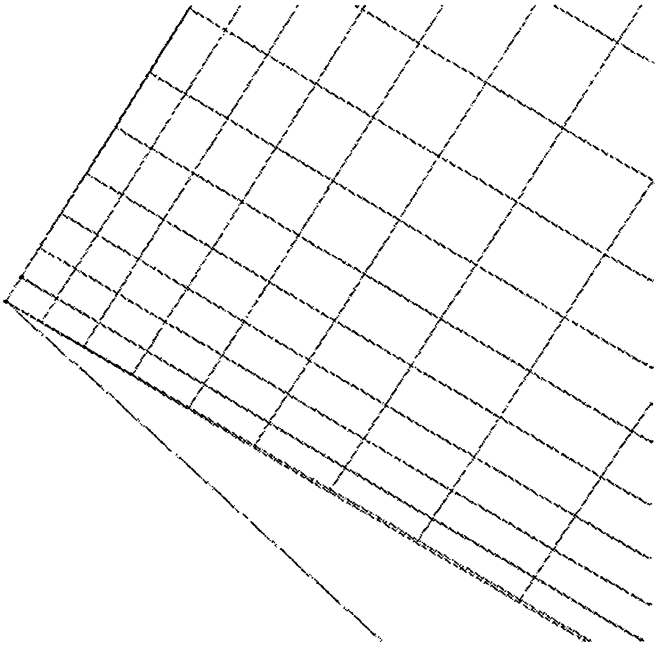

Figure 3.47 Split domains on elevon surface.

In figure 3.47, the red line represents the new connector that Gridgen creates when the domain is split. The domain is now two separate domains and the smaller of the two can be deleted to introduce the gap next to the elevon. The advantage of this is that the new domain maintains the database surface that it was originally created on. This results in a new domain that still matches the surface curvature of the original elevon. This process was performed on the left and right side of the elevon and on the upper and lower surface of the elevon. Figure 3.48 shows the completed gap.

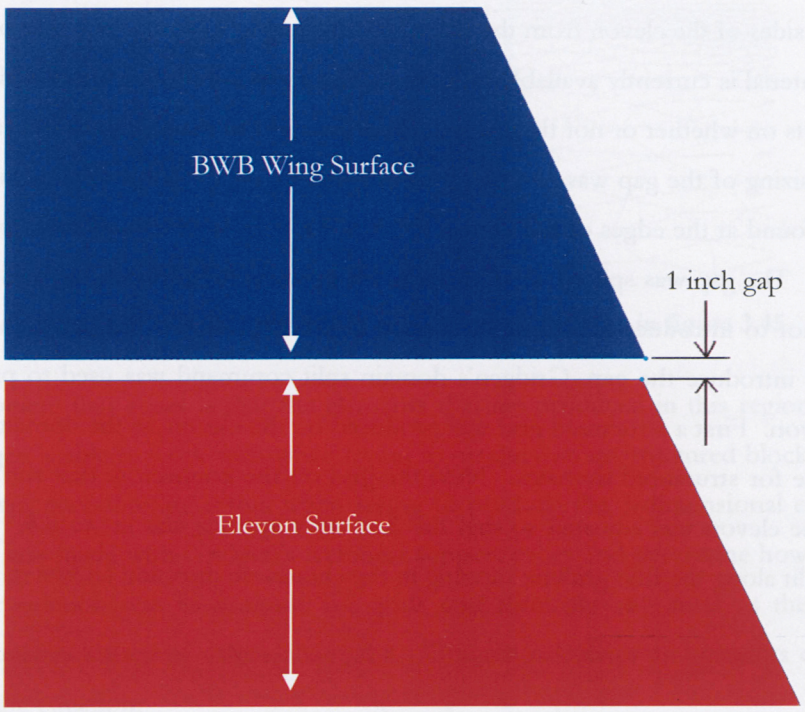

Figure 3.48 Top view of gap.

In figure 3.48 the gap width is 1 inch wide, the length of edge from the deflection point to the trailing edge is approximately 100 inches. This results in a total surface area of 100 in^2 for the gap. This value is multiplied by 4 to account for each side of the elevon and the top and bottom of the elevon giving a total surface area of 400 in^2 or approximately 3 ft^2. The total elevon surface area without the gap is 197 ft^2, this results in 1.5% of the surface area of the elevon being removed through the creation of a gap between the un-deflected and deflected portion of the BWB and elevon. The total surface area of the BWB is 6953.4 ft^2 which results in 0.05% of the total BWB surface area removed through the introduction of the gap. These values can be considered small in comparison to the total surface areas.

Next the new surfaces created as a result of the gap are meshed. The gap width was meshed with a 5x200 unstructured mesh and is pictured in figure 3.49

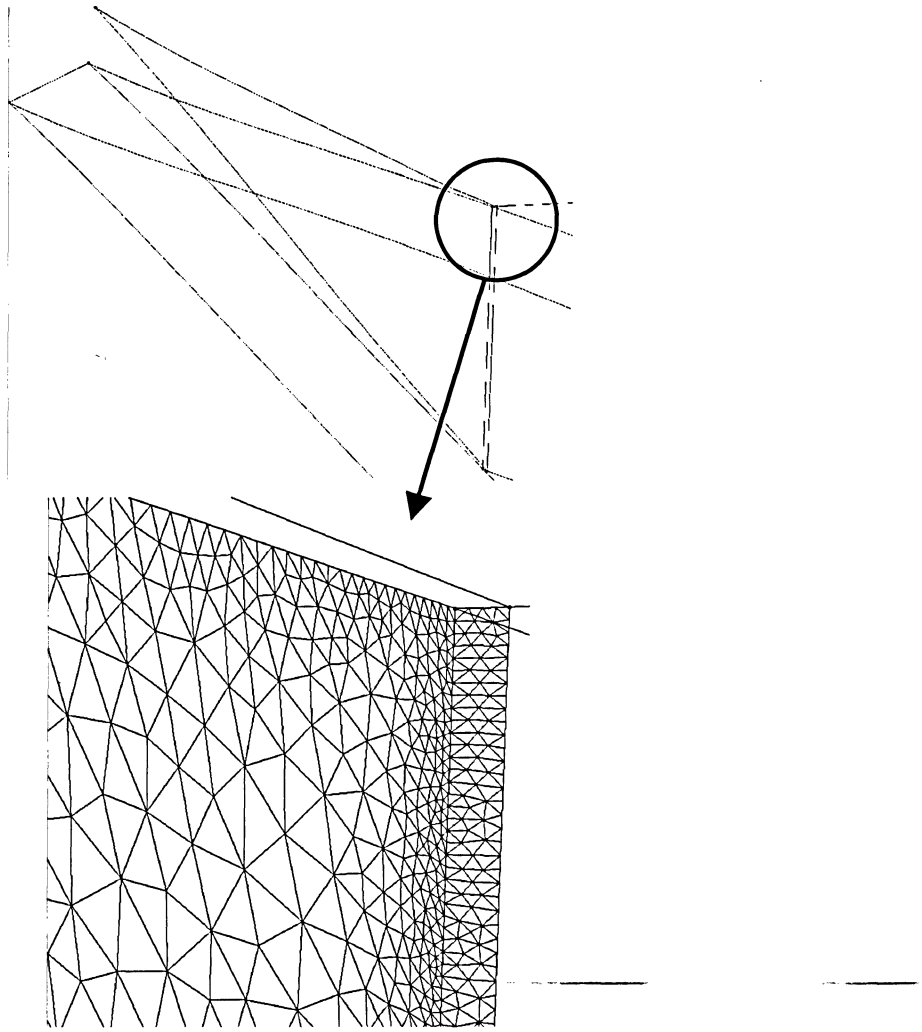

Figure 3.49 Unstructured grid in gap region.

From this point, the unstructured block is assembled, as was outlined in section 3.9. The tetrahedral size factor was set to 0.5, where 1 is large and 0 is small, to help conserve computational resources. The node count at the domain extents in the farfield were increased from 25 to 100 as problems were encountered when trying to produce the unstructured block. Gridgen's technical support was contacted in regards to the problem, and it was suggested that the elements at the domains extent were too large and that the dynamic range between element sizes needed to be reduced. Therefore the node count at the farfield was increased. This resulted in a final grid that had 3,173,214 elements. From this point, the boundary conditions were set as outlined in section 3.10, and the grid was exported to Fluent.

With working grids created, the setup of a grid case to run in Fluent is outlined in chapter four.

Chapter 4

Flow Solver

4.1 Introduction

The flow solver used for this work is Fluent version 6.1. The choice of flow solver can be dependent on a number of factors. It can be based on the type of grid being solved, unstructured or structured, the type of flow being solved, inviscid or viscid solutions, and the type of turbulence model. Fluent is a highly used CFD code, used both in industry and academia. It is capable of solving unstructured, structured and hybrid grids. It is capable of running both viscous and inviscid solutions and turbulence modeling, in three dimensions or two.

In section 4.2, the governing equations of fluid mechanics and their use in Fluent are outlined. Section 4.3 outlines the finite volume method, and finally Section 4.4 and the following subsections discuss the setup of a problem in Fluent and the settings pertinent to this work.

4.2 RANS Equations

The basis of fluid dynamics revolves around trying to model the flow of fluids and their interactions with the environment through the Navier-Stokes equations. The ultimate goal would be to find an analytical solution to these equations with general boundary conditions; however, this is not possible for realistic aerodynamic applications. Instead, numerical approximations are used to try and find approximate solutions to the interactions of fluids with their environment. Fluent uses a Reynolds-Averaged approach to model turbulence in fluids. The Reynolds-Averaged approach involves the transformation of the Navier-Stokes equations so as to remove the need to directly model small scale turbulent fluctuations. This transformation models the Navier-Stokes equations as

mean flow transport equations, known as Reynolds Averaged Navier-Stokes (RANS) equations. To decompose the exact Navier-Stokes equations to the Reynolds Averaged form of the equations, the scalar quantities such as velocity, pressure etc. are written in their mean and fluctuating components, as indicated by equation 4.1, where $\overline{\phi}_i$ is the mean component and ϕ_i' is the fluctuating component.

$$\phi_i = \overline{\phi}_i + \phi_i' \tag{4.1}$$

To obtain the RANS equations, equation 4.1 is substituted into the continuity, momentum, and energy equations. These equations are then time averaged. A quantity f time averaged is defined as:

$$\overline{f} \equiv \frac{1}{\Delta t}\int_{t_0}^{t_0+\Delta t} f dt \tag{4.2}$$

In equation 4.2, Δt is a large time period compared to the random fluctuations associated with the fluctuating components. Secondly, the time-average of a fluctuating quantity f is defined as;

$$\overline{f'} \equiv \frac{1}{\Delta t}\int_{t_0}^{t_0+\Delta t} f' dt \equiv 0 \tag{4.3}$$

Taking the time average of the continuity and momentum equation result in equations 4.4 and 4.5

$$\frac{\partial \overline{\rho}}{\partial t} + \frac{\partial}{\partial x_i}(\overline{\rho u_i} + \overline{\rho' u'_i}) = 0 \tag{4.4}$$

$$\begin{aligned} &\frac{\partial}{\partial t}\left(\overline{\rho u_i} + \overline{\rho' u'_i}\right) + \frac{\partial}{\partial x_j}\left(\overline{\rho u_i u_j} + \overline{u_i \rho' u'_j}\right) \\ &= -\frac{\partial \overline{p}}{\partial x_i} + \frac{\partial}{\partial x_j}\left(\overline{\tau}_{ij} - \overline{u_j \rho' u'_i} - \overline{\rho u'_i u'_j} - \overline{\rho' u'_i u'_j}\right) \end{aligned} \tag{4.5}$$

Where

$$\overline{\tau_{ij}} = \mu\left[\left(\frac{\partial \overline{u_i}}{\partial x_j} + \frac{\partial \overline{u_j}}{\partial x_i}\right) - \frac{2}{3}\delta_{ij}\frac{\partial \overline{u_k}}{\partial x_k}\right] \tag{4.6}$$

Equations 4.4 and 4.5 have the same general form as the instantaneous Navier-Stokes equations except that the flow variables have been replaced by time-averaged flow variables. The term $-\overline{\rho u_i' u_j'}$ called the Reynolds stress in equation 4.5, models the effects of turbulence. Fluent models the effect of this term, by using the Boussinesq assumption [32]. The Boussinesq assumption relates the Reynolds stresses to the mean velocity gradients by the following equation.

$$-\overline{\rho u_i' u_j'} = \mu_T\left(\frac{\partial \overline{u_i}}{\partial x_j} + \frac{\partial \overline{u_j}}{\partial x_i}\right) - \frac{2}{3}\delta_{ij}\left(\mu_T\frac{\partial \overline{u_k}}{\partial x_k} + \rho\overline{k}\right) \tag{4.7}$$

In equation 4.7, μ_T is the turbulent viscosity, $\overline{k}$ represents the turbulence kinetic energy and is given by $k = \overline{u_i' u'}_i / 2$.

Equations 4.4 and 4.5 can be further simplified by mass-weighted averaging suggested by Favre and better known as Favre averaging. The full proof of Favre averaging is not included in this work but can be found in reference [26]. Favre averaging is useful for treatment of compressible flows and mixtures of gases. When the density fluctuations in a flow can be neglected, Reynolds averaging and Favre averaging become identical. The continuity and momentum equations are re-written in their mass-weighted average form and presented in equations 4.8 and 4.9.

$$\frac{\partial \overline{\rho}}{\partial t} + \frac{\partial}{\partial x_i}(\overline{\rho u_i}) = 0 \tag{4.8}$$

$$\frac{\partial}{\partial t}\left(\overline{\rho u_i}\right) + \frac{\partial}{\partial x_j}\left(\overline{\rho u_i u_j}\right) = -\frac{\partial \overline{p}}{\partial x_i} + \frac{\partial}{\partial x_j}\left(\overline{\tau_{ij}} - \overline{\rho u_i' u_j'}\right) \tag{4.9}$$

4.3 Finite Volume Method

The analytical equations used by Fluent have been outlined in section 4.2; however, these equations must be converted to a set of algebraic equations that Fluent can solve using numerical methods. Fluent uses a control volume technique to accomplish this.

The explanation of the finite volume method begins by writing the transport equation for a general variable ϕ in differential form, as given in equation 4.10 where Γ is a general diffusion coefficient.

$$\frac{\partial(\rho\phi)}{\partial t} + \nabla \cdot (\rho\phi\mathbf{u}) = \nabla \cdot (\Gamma \cdot \nabla\phi) + S_\phi \tag{4.10}$$

Equation 4.10 illustrates the various transport processes: the rate of change and convective terms on the left hand side, followed by the diffusive and source terms on the right hand side. The next step in the finite volume method is to integrate equation 4.10 over the entire control volume resulting in equation 4.11.

$$\int_{CV} \frac{\partial(\rho\phi)}{\partial t} dV + \int_{CV} \nabla \cdot (\rho\phi\mathbf{u}) dV = \int_{CV} \nabla \cdot (\Gamma \cdot \nabla\phi) dV + \int_{CV} S_\phi dV \tag{4.11}$$

The volume integrals of the convective term on the left hand side and the diffusive term on the right hand side are replaced by integrals over the entire bounding surface of the control volume using Gauss' divergence theorem. This theorem states that for a given vector **a**,

$$\int_{CV} \nabla \cdot \mathbf{a} dV = \int_{A} \mathbf{n} \cdot \mathbf{a} dA \tag{4.12}$$

Equation 4.10 states that the divergence of vector **a** over a control volume V, is equal to the component of vector **a** in the direction normal to the surface which bounds the volume, integrated over the entire bounding surface A. Applying Gauss' divergence theorem to the convection and diffusion terms in equation 4.9 yields,

$$\int_{CV} \frac{\partial(\rho\phi)}{\partial t} dV + \int_{A} \mathbf{n} \cdot (\rho\phi\mathbf{u}) dA = \int_{A} \mathbf{n} \cdot (\Gamma \cdot \nabla\phi) dA + \int_{CV} S_\phi dV \tag{4.13}$$

Equation 4.13 can be expressed in words as follows,

Rate of change of ϕ in C.V.	+	Flux of ϕ due to convection across the boundaries	=	Flux of ϕ due to diffusion across the boundaries	+	Rate of creation of ϕ from sources in C.V.

If the problem is steady-state, the rate of change term in equation 4.13 is equal to zero, thus simplifying equation 4.13 to,

$$\int_A \mathbf{n}\cdot(\rho\phi\mathbf{u})dA = \int_A \mathbf{n}\cdot(\Gamma\cdot\nabla\phi)dA + \int_{CV} S_\phi dV \tag{4.14}$$

The discritization of equation 4.14 is best explained through a simple one-dimensional convection-diffusion problem. To start, equation 4.10 is re-written dropping the source term on the right hand side of the equation and the rate of change term on the left hand side of the equation. The source term in equation 4.14 can be eliminated since the problem does not include the creation/injection of species; likewise source terms are not included in the continuity or momentum equations developed in the previous section for the same reasons. Since the equation is one-dimensional we use only the x-component.

$$\frac{d}{dx}(\rho u\phi) = \frac{d}{dx}\left(\Gamma\frac{d\phi}{dx}\right) \tag{4.15}$$

Also the problem must satisfy continuity,

$$\frac{d(\rho u)}{dx} = 0 \tag{4.16}$$

The problem is illustrated in figure 4.1 in which a control volume surrounds node C with neighboring nodes A and B, with control volume faces labeled a, and b. The entire length of the control volume is denoted δx_{ab}, while the distance from node center to the faces of the control volume are denoted δx_{aC}, and δx_{Cb}. The distances between nodes is denoted by δx_{AC}, and δx_{CB}.

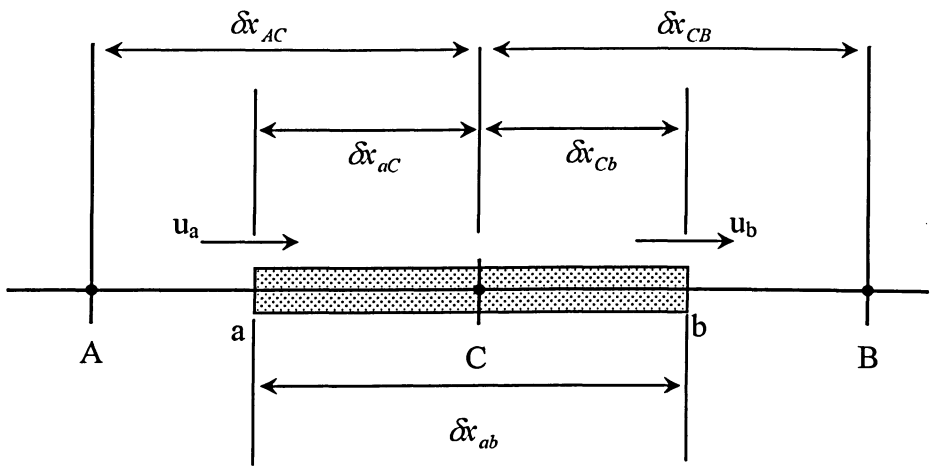

Figure 4.1 One dimensional convection diffusion problem layout.

Next equations 4.15 and 4.16 are integrated over the control volume yielding equations 4.17 and 4.18.

$$(\rho u A\phi)_b - (\rho u A\phi)_a = \left(\Gamma A \frac{d\phi}{dx}\right)_b - \left(\Gamma A \frac{d\phi}{dx}\right)_a \tag{4.17}$$

$$(\rho u A)_b - (\rho u A)_a = 0 \tag{4.18}$$

For this problem, the velocity field is assumed to be known and that $A_a = A_b = A$. Making these assumptions allows equation 4.18 to be solved leaving only equation 4.17 remaining to be solved.

The diffusive terms on the right hand side of equation 4.17 require us to know the interface diffusion coefficient Γ and gradient $d\phi/dx$ at locations a, and b in figure 4.1. The values of Γ and ϕ are evaluated and stored by Fluent at the cell nodes, in this case at A, B and C, however the gradients at the cell faces are required. The use of central differencing through linear approximations is used to calculate these gradients. Fluent uses these methods for the diffusive gradients only, with higher order methods used to calculate variables at the C.V. boundary. Using linear interpolation to calculate the diffusive coefficients at the faces of the control volume, results in equations 4.19a and 4.19b given below.

$$\Gamma_a = \frac{\Gamma_A + \Gamma_C}{2} \tag{4.19a}$$

$$\Gamma_b = \frac{\Gamma_C + \Gamma_B}{2} \tag{4.19b}$$

Next the diffusive gradients are calculated as,

$$\left(\Gamma A\frac{d\phi}{dx}\right)_a = \Gamma_a\left(\frac{\phi_C-\phi_A}{\delta x_{AC}}\right) \tag{4.20}$$

$$\left(\Gamma A\frac{d\phi}{dx}\right)_b = \Gamma_b\left(\frac{\phi_B-\phi_C}{\delta x_{CB}}\right) \tag{4.21}$$

Equations 4.20 and 4.21 are substituted into equation 4.17 to yield,

$$(\rho u\phi)_b-(pu\phi)_a=\Gamma_b\left(\frac{\phi_B-\phi_C}{\delta x_{CB}}\right)-\Gamma_a\left(\frac{\phi_C-\phi_A}{\delta x_{AC}}\right) \tag{4.22}$$

The only terms in equation 4.20 that are left to determine are the convective values of ϕ at the cell faces a, and b.

Fluent has several schemes for calculating the face values ϕ_a, and ϕ_b in equation 4.22. The schemes used for this work are the first order and second order upwinding schemes. Upwinding has been developed to simulate numerically, the direction of the propagation of flow field information. The first method employed, first order upwinding determines the face values by assuming that the cell face value is equal to the cell value 'upstream' of the face. In this problem then, $\phi_a=\phi_A$, and $\phi_b=\phi_C$. The only drawback of the first order scheme is that because of the first order accuracy it is highly diffusive when the flow is not aligned with the grid. This error can be reduced by increasing the grid density; this though has its own drawbacks. To overcome this problem higher-order methods are available, for this work the second-order method was used for the viscous solutions. In the second order upwinding scheme the face value is calculated based on the upstream cell center value and the gradient between the cell center node and cell face.

$$\phi_f=\phi+\mathbf{n}\cdot(\nabla\phi) \tag{4.23}$$

For the previously outlined problem the second order upwinding scheme can be written as,

$$\phi_f=\phi_b=\frac{3}{2}\phi_C-\frac{1}{2}\phi_B \tag{4.24}$$

4.4 Case Setup

There are numerous settings that need to be adjusted when setting up a case. The main settings that need to be adjusted for both a viscous solution and an inviscid solution are outlined in this chapter. For a complete outline on all the settings and their application the reader is referenced to the Fluent manual [32].

4.4.1 Grid Setup

With grids created in Gridgen the first step is to import the grid into Fluent and check its structure. This will check a variety of properties of the grid such as volume statistics and element statistics for any errors. If errors are found the user must correct these errors before solver settings can be adjusted. Next, the user should make sure that the grid is scaled correctly. In this case, the grid was created in inches and Fluent's default setup is in meters, therefore the grid must be scaled back to inches to keep the correct proportions.

4.4.2 Segregated Vs Coupled

The first selection the user has to make is in the type of solution algorithm fluent will use. The user has two choices, either segregated or coupled. Fluent's segregated solution algorithm solves the governing equations sequentially. Figure 4.2 outlines this process.

The second option is the coupled solution algorithm. The coupled solver solves the governing equations, continuity, momentum, and when invoked energy and species transport simultaneously. Figure 4.3 outlines this process.

The segregated solver can be advantageous when dealing with low speed flow solutions where compressibility is not significant. For this work, however, the flow is high speed and since some regions will contain high subsonic and even supersonic flow, a coupled solver is required. In both of the above methods, the non-linear governing equations must be linearized to produce a set of equations for the dependent variable for each computational cell in the grid. These equations are then solved to produce an updated flow field solution. This is done in either an implicit or explicit fashion, which is outlined in the next section.

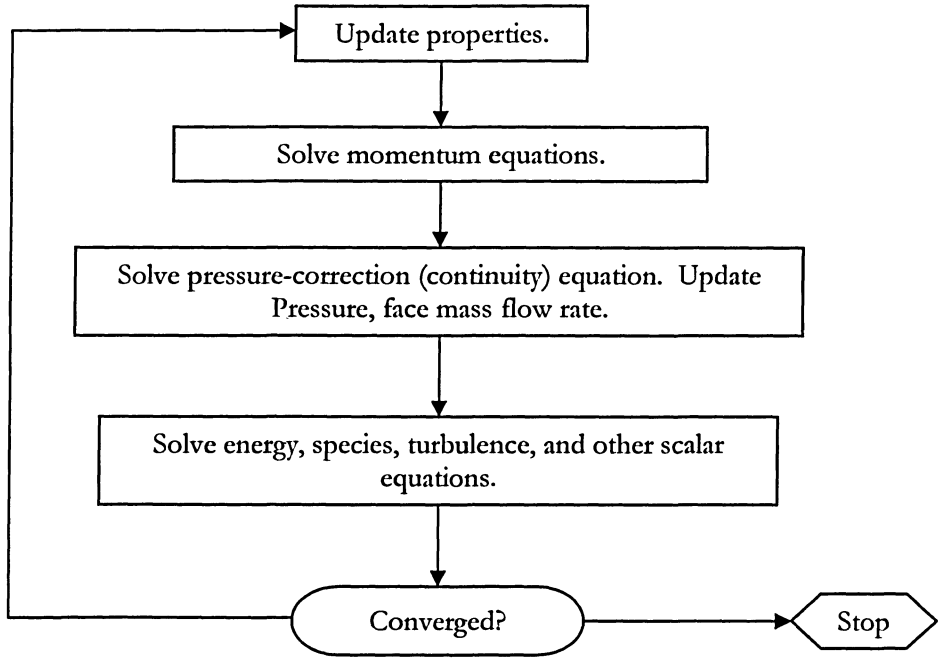

Figure 4.2 Fluent's segregated solver method. [32]

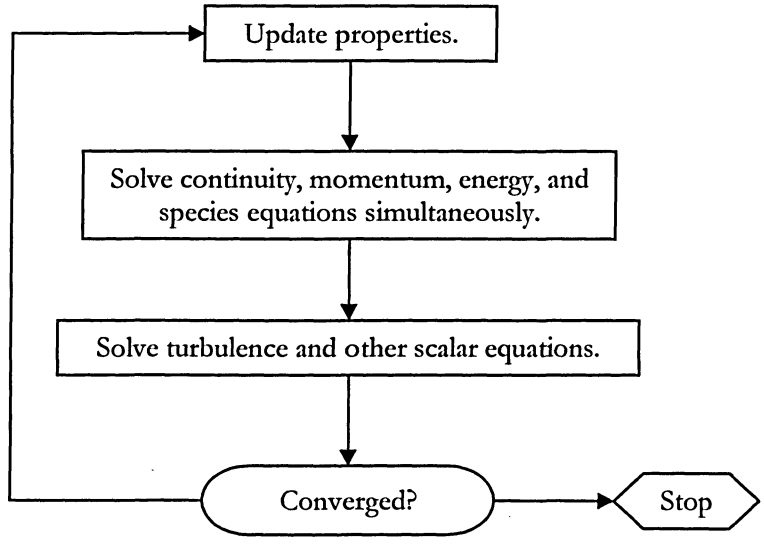

Figure 4.3 Fluent's coupled solver method. [32]

4.4.3 Implicit Vs Explicit

The user has two choices when using a coupled solver, either implicit or explicit time integration. The differences in the implicit and explicit method is best shown by considering the following equation,

$$\frac{\partial \phi}{\partial t} = \frac{\partial^2 \phi}{\partial x^2} \tag{4.26}$$

Writing out the left hand side of equation 4.26 using a forward difference equation, and the right hand side using a central differencing scheme yields equation 4.27. The derivation of differencing equations is not included in this work, rather the derivation of these equations can be found in any substantial text on CFD.

$$\frac{\phi_i^{n+1} - \phi_i^n}{\Delta t} = \frac{\phi_{i+1}^n - 2\phi_i^n + \phi_{i-1}^n}{(\Delta x)^2} \tag{4.27}$$

Rearranging equation 4.27 for ϕ_i^{n+1},

$$\phi_i^{n+1} = \phi_i^n + \frac{\Delta t}{(\Delta x)^2}\left(\phi_{i+1}^n - 2\phi_i^n + \phi_{i-1}^n\right) \tag{4.28}$$

In the above equation, n represents the variable at time t, and $n+1$ represents the variable at time $t + \Delta t$. In equation 4.28, given initial conditions, the unknown value in a cell is found using a relation that involves only known values. The result is that the unknown appears in one equation only and therefore can be solved explicitly

In the implicit method a flow variable is solved in each cell using a relationship that uses both existing and unknown values from neighboring cells. The result is that more than one unknown variable will appear in each linearized equation and therefore the system needs to be solved simultaneously to solve for the unknowns. This is shown by returning to equation 4.26 and this time writing the right hand side of the equation in terms of the average of the variable between times t and $t + \Delta t$.

$$\frac{\phi_i^{n+1} - \phi_i^n}{\Delta t} = \frac{1}{2}\left(\frac{\phi_{i+1}^{n+1} - 2\phi_i^{n+1} + \phi_{i-1}^{n+1}}{(\Delta x)^2}\right) \tag{4.29}$$

Equation 4.29 contains unknown values at time index $n+1$ on the right hand side of the equation, therefore equations must be produced for all grid points and the equations solved simultaneously to arrive at a solution.

The segregated implicit solver solves for a single flow variable in every cell at the same time. It then solves the next flow variable in the same fashion, repeating this process for each flow variable. For the coupled solver, the user has the choice between the implicit or explicit linearization. For the coupled implicit method all variables are solved in all cells at the same time. For the coupled explicit method all the flow variables are solved one cell at a time.

For this work the coupled solver was used. Initially for the baseline case an explicit method was used. The explicit solver was chosen because it uses less computational resources than the coupled implicit method. This choice was based on the initial computational resources available at Ryerson University which consisted of a single processor machine with 2GB of RAM. Later Ryerson University acquired access to the High Performance Computational Virtual Laboratory (HPCVL) which consists of multiple computer clusters with large quantities of RAM and multiple CPU's.

4.4.4 Energy Equation

The next step is the choice of the inclusion of the energy equation. In Fluent, the energy equation is defined as:

$$\frac{\partial}{\partial t}(\rho E)+\nabla\cdot(\vec{v}(\rho E+p)) = \nabla\cdot\left(k_{eff}\nabla T-\sum_j h_j\vec{J}_j+(\overline{\overline{\tau}}_{eff}\cdot\vec{v})\right)+S_h \tag{4.30}$$

Equation 4.30 includes a number of terms which are applied by Fluent depending on the setup of the case by the user. On the right hand side of equation 4.30, the first three terms represent the energy transfer due to conduction, species transfer and viscous dissipation. For the first term on the right hand side of equation 4.30, k_{eff} represents the effective thermal conductivity given by $k+k_t$, where k_t is the thermal conductivity due to turbulence and is determined by Fluent depending on the turbulence model selected. In the second term, $\vec{J}_j$ represents the diffusion flux of species j and is not included in this work as it does not deal with multiple species. The third term represents the thermal energy created by viscous shear in the flow. The final term on the right side of equation 4.30, S_h represents the heat due to chemical reactions and any other volumetric heat source defined by the user. In this case S_h is not included since it does not involve any specific

chemical reactions or user defined energy sources. Pressure work and kinetic energy are included on the left side of equation 4.30 where;

$$E = h - \frac{p}{\rho} + \frac{v^2}{2} \tag{4.31}$$

4.4.4 Viscous Solver

Fluent allows the user to select a number of different turbulence models depending on the type of flow, required accuracy and available computational resources. Fluent has five turbulence models and they are:

1.) 1-eqn Spalart Allmaras
2.) 2-eqn k-epsilon
3.) 2-eqn k-omega
4.) 7-eqn Reynolds Stress
5.) Large Eddy Simulation

All of these turbulence models are outlined in the Fluent manual [32] in detail. In this work the 1-eqn Spalart Allmaras model was used initially on the baseline case based on its wide use for wall bounded flow simulations and the efficient use of computational resources. This was then switched to the inviscid model for the unstructured grids on the deflected and modified geometries. The Spalart Allmaras model was mentioned in chapter 3. When an inviscid solution is run, Fluent solves the Euler equations which are equations 4.4, 4.5 and 4.30 without viscous effects.

4.4.5 Materials

Fluent allows the user to adjust the properties of the fluid using the materials control panel. Here, the user selects the appropriate fluid, in this case air, and is able to adjust numerous properties of the material. The available properties that the user is able to adjust will be dependent on how the case is being setup. For this work, the calculation of density is found through the ideal gas law, defined in Fluent as:

$$\rho = \frac{p_{op} + p_{gauge}}{RT} \tag{4.32}$$

Where p_{op} the operating pressure is specified by the user and p_{gauge} is the gauge pressure determined by Fluent. For an inviscid calculation this is the only necessary material adjustment. When viscous effects are included the only other adjustment that is made from the default values is the calculation of laminar viscosity and by association, the thermal conductivity. The laminar viscosity is defined using a temperature dependent function, namely, the Sutherland law. Fluent has five different temperature dependent functions. The Sutherland law was selected based on recommendations by Fluent for this type of work as it is well suited for high speed compressible flows.

4.4.6 Boundary Conditions

The boundary conditions (BC) used in this work were outlined at the end of chapter 3, they were pressure far-field, symmetry and wall boundary conditions. There are a number of different boundary conditions that Fluent can simulate depending on the flow model, but for this work these were the only three used. The first boundary condition, pressure far-field, is used in Fluent to model free stream conditions at infinity. This boundary condition is only applicable when the density is calculated using the ideal gas law as outlined in section 4.4.5. When the pressure far-field BC is used, the user must give the free stream Mach number, static conditions, i.e., the free stream pressure and temperature, and the flow direction, given in x, y and z components. For this work the test conditions are the following:

Mach number: 0.85

Altitude: 35,000 ft

Gauge Pressure: 497.956 lb/ft^2

Temperature: 393.854 $^\circ$R

Angle of Attack α : 3.75°

X-component of flow direction: 0.9978589

Y-component of flow direction: 0

Z-component of flow direction: 0.0654031

The second boundary condition, symmetry, is used when the expected flow pattern and geometry have mirror symmetry. Fluent applies the symmetry condition by applying zero normal velocity and zero normal gradients of all the flow variables at the symmetry boundary. No inputs by the user are required for the symmetry boundary condition.

The third and final boundary condition used is the wall BC. For this work two different applications of the wall boundary are applied. For the inviscid solutions, Fluent applies a slip condition at the wall and therefore the wall exerts no shear stress on the adjacent fluid. When viscous effects are included through the use of the Spalart Allmaras turbulence model or any of the other turbulence models, Fluent applies a no-slip condition at the wall, and therefore wall shear stresses need to be evaluated. Given a general flow field with viscous effects included, the wall exerts a shear stress on the fluid. The wall shear stress, given by τ_w is proportional to the flow gradient $\partial u/\partial n$ and is expressed as,

$$\tau_w \propto \frac{\partial u}{\partial n} \tag{4.33}$$

The proportionality in equation 4.33 is defined as the viscosity coefficient μ, this yields,

$$\tau_w = \mu \frac{\partial u}{\partial n} \tag{4.34}$$

Equation 4.34 is an analytic solution for the wall shear stress; however, it requires knowledge of both the viscosity coefficient and the velocity gradient. The calculation of the viscosity coefficient is dependent on the selection of turbulence model. The velocity gradient requires that the grid be sufficiently resolved in the boundary layer to accurately model turbulent flow.

In Fluent, through the use of the Spalart Allmaras model, the following equations are used depending on the grid near wall resolution:

$$\frac{u}{u_\tau} = \frac{\rho u_\tau y}{\mu} \tag{4.35}$$

$$\frac{u}{u_\tau} = \frac{1}{\kappa} \ln E\left(\frac{\rho u_\tau y}{\mu}\right) \tag{4.36}$$

Where

u = velocity parallel to the wall

u_τ = shear velocity

y = distance from the wall

κ = von Kármán constant = 0.4187 [32]

E = 9.793 [32]

Equations 4.35 and 4.36 are dependent on the type of the grid. If the grid clustering is tight enough to resolve the laminar sublayer, then equation 4.35 which is the laminar shear-stress relationship is used. If, on the other hand, the grid quality is not fine enough to resolve the laminar sublayer, Fluent assumes that the centroid of the cell lies within the logarithmic region and uses equation 4.36 which is the law of the wall for the S-A turbulence model.

4.4.7 Solution Controls

The solution control panel allows the user to set various parameters that have been enabled during the case setup process. These include selection of the enabled equations that are solved, under-relaxation parameters, the selection of the upwinding scheme, as discussed in section 4.3, and finally selection of the Courant number which controls the time stepping scheme.

The first of these selections allows the user to enable or disable equations that Fluent is solving during the iteration process. This can allow the user to focus on certain equations pertinent to the solution or help to reach convergence if equations are causing stability problems. For this work, nothing was adjusted and all equations were solved simultaneously.

Next, the user is able to adjust the under-relaxation parameters. These settings are used by Fluent to control the update of computed variables during iterations. Due to the non linearity of the governing equations under-relaxation parameters are used to reduce the change in the variable. The change in variable ϕ is controlled via equation 4.37.

$$\phi_{new} = \phi_{old} + \alpha\Delta\phi \tag{4.37}$$

Where ϕ_{old} is the old value, α is the under-relaxation parameter, and $\Delta\phi$ is the computed change in ϕ. The default values used by Fluent have been set to the optimal values for the widest range of problems; however, if divergence is a problem in the solution, the user is capable of adjusting these

values to try and reduce the divergence and obtain convergence. Again, for this work no changes in the under-relaxation parameters were made.

Finally, the user is capable of adjusting the Courant number to directly affect the time step used by Fluent. The Courant number is calculated based on the Courant-Friedrichs-Lewy condition or CFL condition. The value of CFL for which a given numerical scheme (implicit or explicit) is stable, is defined under linear stability theory. Linear stability theory is discussed in detail in references [21] and [26]. The details of linear stability theory are beyond the scope of this work and only the limits for each method will be discussed. In general though, linear stability theory shows that, for stability, the Courant number should equal or be less than 1 when using an explicit scheme. For an implicit scheme, linear stability theory shows it to be unconditionally stable. When running the coupled explicit solver in Fluent, the Courant number can be increased to 2.5 through the use of residual smoothing. For the first case, the baseline un-deflected geometry the Courant number was set as low as 0.0125 during the beginning of the iterations to maintain stability and increased slowly as the solution progressed. For the inviscid solutions which were run implicitly the Courant number was set at 0.1 at the beginning and increased to 5 to speed up convergence.

4.4.8 Solution Monitors

The user is capable of monitoring the progress of the solution while it is running iterations through the use of solution monitors. Fluent monitors the convergence of the solution through the residuals monitor. The user can also manage convergence through monitoring values of C_L and C_D. To setup the monitors of C_L and C_D, the user must select a boundary surface on which to calculate C_L and C_D and input the appropriate component vectors for the lift force and drag force calculation. In figure 4.4 below, an airfoil is pictured in freestream flow V_∞ at an angle of attack α. It shows the vectors and the components of those vectors that define lift and drag. R in figure 4.4 is the resultant aerodynamic force acting on the airfoil, where;

$$Lift \equiv L \equiv \text{component of R perpendicular to } V_\infty$$

$$Drag \equiv D \equiv \text{component of R parallel to } V_\infty$$

R can further be split into its components N and A, where N is the normal vector perpendicular to the chord c, and A is the axial vector parallel to chord c. Lift and drag can then be written in terms of the angle of attack α and the normal and axial components.

$$L = N\cos\alpha - A\sin\alpha \tag{4.38}$$

$$D = N\sin\alpha + A\cos\alpha \tag{4.39}$$

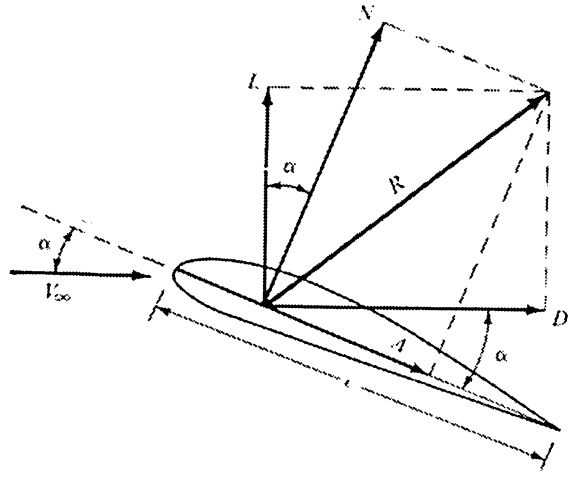

Figure 4.4 Layout of lift and drag vectors and their components. [34]

In Fluent, for this case, the user would input $\cos\alpha$ as the z-component and $-\sin\alpha$ for the x-component for the calculation of C_L. For the calculation of C_D, the user would input $\sin\alpha$ for the z-component and $\cos\alpha$ for the x-component. There are a number of ways that the residual and force monitors can be displayed, they can be plotted, printed out to screen, written to a data file or a combination of all three. The convergence criterion for this work was such that the values and C_L and C_D converged to within four significant figures. An example of this is shown in figure 4.5 which shows the convergence of C_L for the baseline negative deflection.

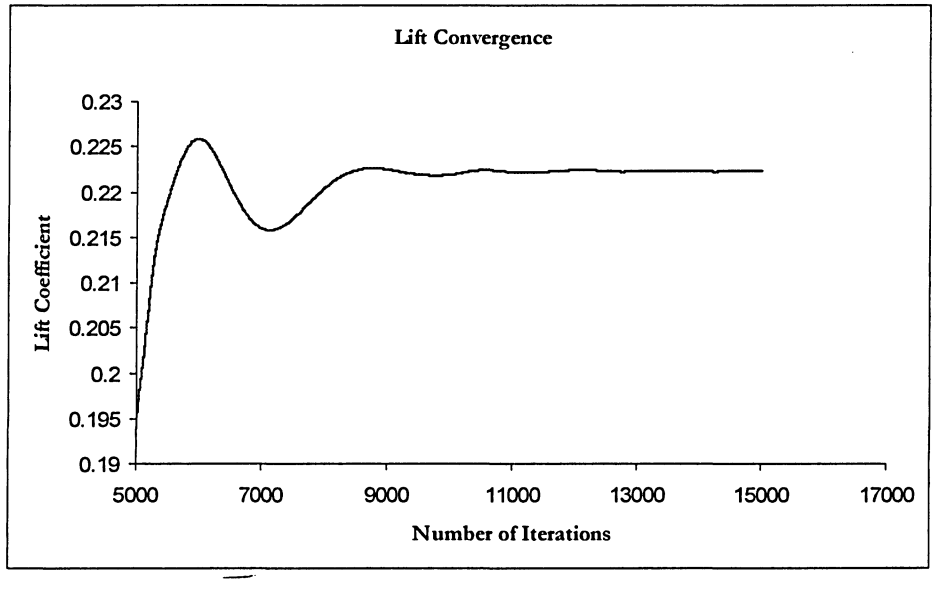

Figure 4.5 Graph of lift convergence for baseline negative deflection.

Chapter 5

Results

5.1 Introduction

In this chapter the results of this work are presented. In section 5.2, the results of the numerical validation are presented to show that the case setup used in this work, along with the use of Fluent, are valid for modeling airfoil flows with deflected surfaces. In section 5.3, the results of the grid sensitivity study are presented to show that the selection of grid density to help reduce runtimes is valid without sacrificing solution accuracy. Finally in section 5.4 and the subsequent sub sections, the results of the work are presented and the flow phenomena and their bearing on this work are explained.

5.2 Validation

Validation of CFD codes has been, and continues to be, a major subject of work in CFD studies. For this work, a validation study was performed to validate Fluent's code and to validate the case setup in this work. The model that was examined is the 2D NACA 0012 symmetrical airfoil with a 0.20c, 60° deflected split flap. The geometry of this model is pictured in figure 5.1.

The experimental data for this case was obtained by Abbott and Doenhoff using the NACA two-dimensional low-turbulence pressure tunnel [35]. This wind tunnel allowed for the collection of experimental data in two dimensions at large Reynolds numbers, in low-turbulence flow. The results of this research can be found in reference [35].

The computational grid that was built is a fully unstructured grid with triangles clustered near the surface of the wing. The entire computational grid is pictured in figure 5.2, with the grid clustering around the airfoil pictured in figure 5.3.

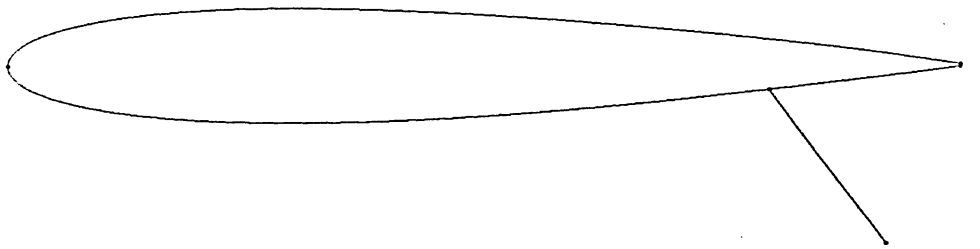

Figure 5.1 NACA 0012 airfoil section with 60° split flap.

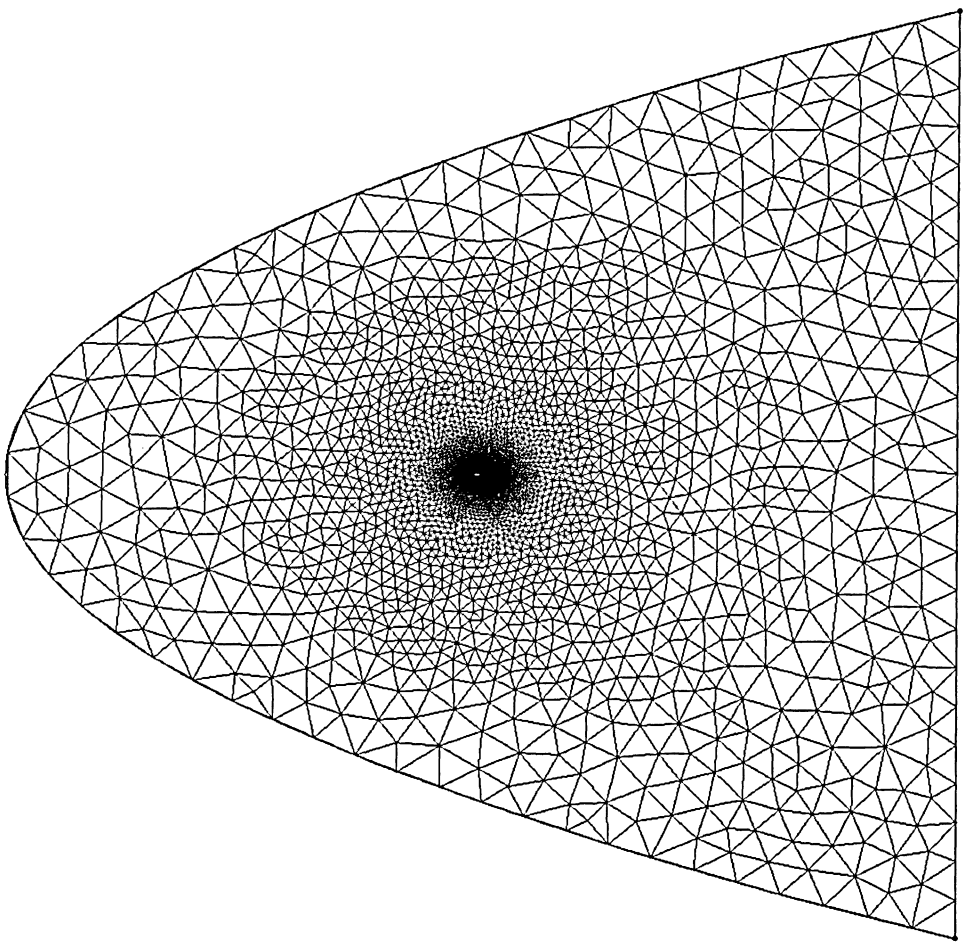

Figure 5.2 Fully unstructured grid around NACA 0012 airfoil.

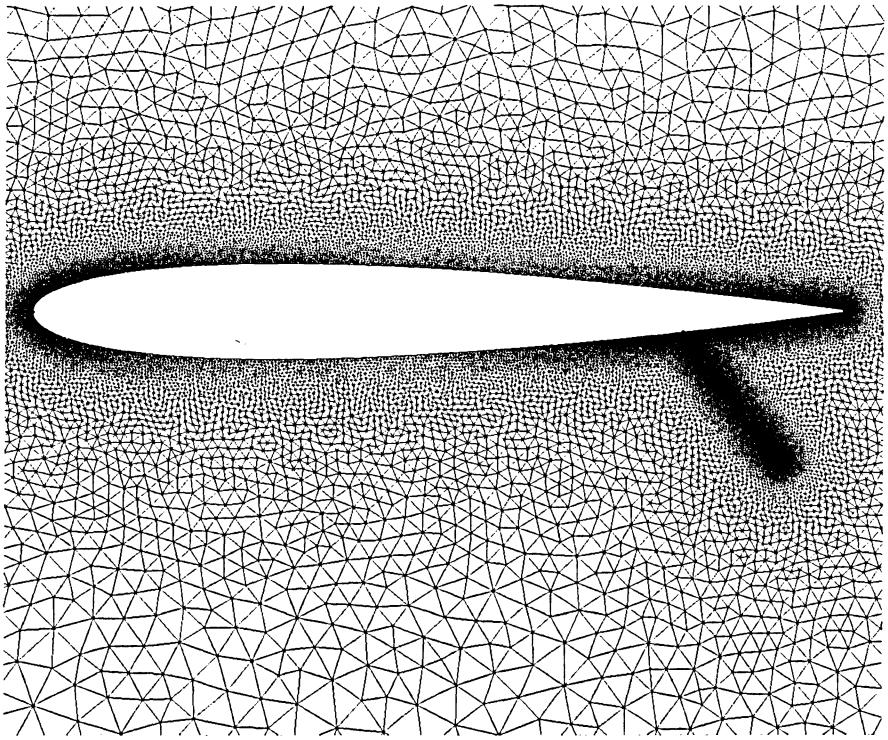

Figure 5.3 Clustered unstructured grid around NACA 0012 airfoil.

The computational model was setup in Fluent to run at a Mach number of 0.1, at standard atmosphere conditions. The computational model was run at 0, ±4°, ±8° and ±12° angle of attack. The results of these test cases are shown in figures 5.4 and 5.5. The experimental and numerical data are presented in table 5.1 along with the percent difference between the two. The experimental results are compared to the numerical results for both C_L and C_M. The hinge line was taken at the quarter cord which coincided with the aerodynamic center.

Angle (degrees)	C_L (Exp)	C_L (Num)	% Difference	C_M (Exp)	C_M (Num)	% Difference
-12	0.1	0.1443	44.30 %	-0.175	-0.2165	23.71%
-8	0.5	0.5542	10.84 %	-0.21	-0.2289	9.00%
-4	0.975	0.9458	-2.99 %	-0.225	-0.2325	3.33%
0	1.4	1.3251	-5.35 %	-0.23	-0.2335	1.52%
4	1.8	1.6955	-5.81 %	-0.23	-0.2336	1.57%
8	2.2	2.0257	-7.92 %	-0.23	-0.2259	-1.78%
12	2.25	2.2883	1.70 %	-0.275	-0.2184	-20.58%

Table 5.1 Experimental and numerical results for validation case with percent error.

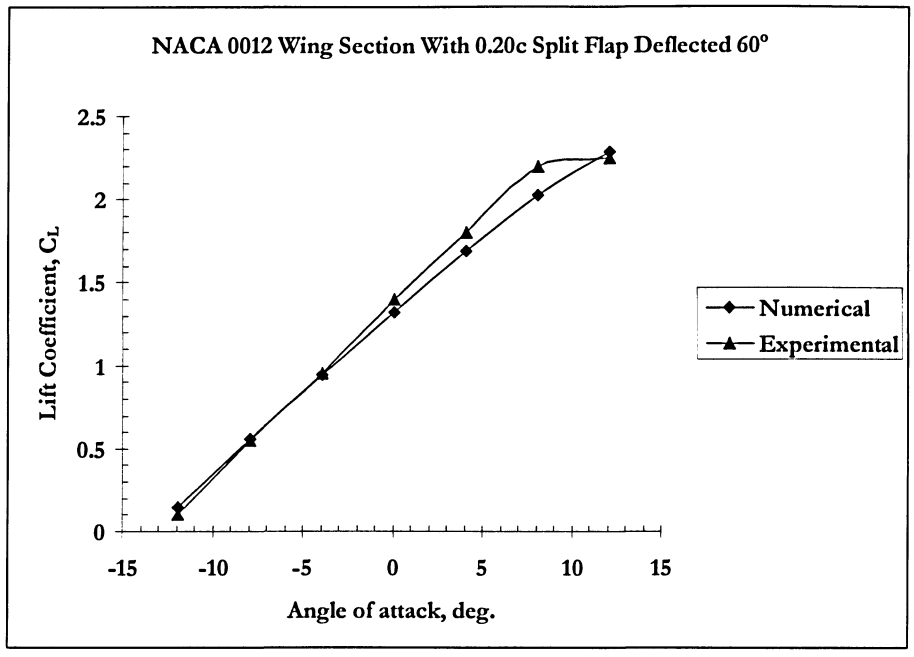

Figure 5.4 Comparison between numerical results and experimental results for C_L for the NACA 0012 airfoil with a 60° split flap.

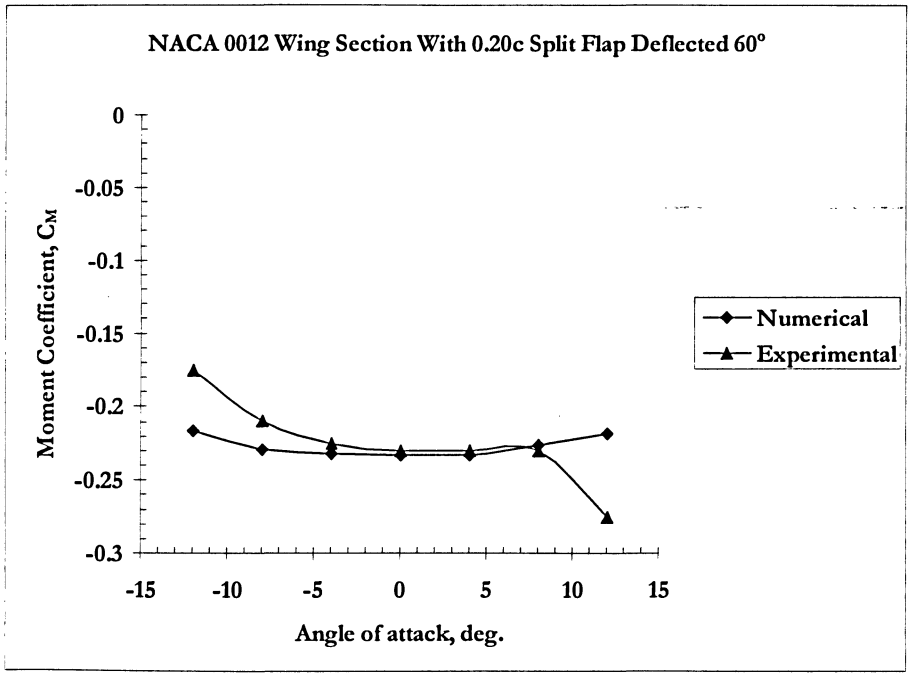

Figure 5.5 Comparison between numerical results and experimental results for C_M for the NACA 0012 airfoil with a 60° split flap.

The numerical results show close agreement with the experimental results for small angles of attack for both C_L and C_M. As the angle of attack increases the solutions start to diverge. This is more than likely the result of the inability of the inviscid solution to predict the flow separation at the

higher angles of attack. The models for both 0° angle of attack and -12° angle of attack where run using the S-A turbulence model to see if the viscous solver would have any affect on the calculation of lift and moment coefficients. For these solutions, the residuals diverged due to instability. After numerous reductions in the Courant number, the solution halted. These results show that for the current work, which focuses on the calculation of moments at small angles of attack and small deflection angles, the use of an inviscid model with an unstructured grid for calculating the moment forces and lift forces is applicable. The drag results obtained were off by an order of magnitude and so are not presented here. The large error in the drag results is due to the absence of the viscous drag component being modeled by the inviscid solver.

5.3 Grid Sensitivity Study

A grid sensitivity study was performed to assess the accuracy in C_L, C_D, and C_M. Four unstructured grids were created using the geometry with a 5° negative deflected elevon with no modification to the trailing edge. The surface of the wing and elevon had 39,327 nodes which were kept constant for all four grids. The grid density within the interior of the domain was controlled through the number of nodes on the farfield boundary connectors and the use of Gridgen's boundary decay function on the symmetry domain. The 360,463 element grid used 25 nodes along each farfield boundary connector and used a boundary decay value of 0.50. For the 3,173,214 element grid, the node count along the boundary connectors was increased to 100 nodes, with a boundary decay factor of 0.95. The grid that was used for this work, the 955,887 element grid, used 50 nodes along the farfield boundary connectors with a boundary decay of 0.9. The results for C_L, C_D, and C_M are presented in table 5.2. The percent error results, using the 3 million element case as a reference, are presented in table 5.3. The results are plotted in figures 5.6, 5.7 and 5.8.

Table 5.2 removed due to proprietary reasons described on page ii.

Table 5.2 Grid sensitivity study results.

Number of Elements	C_L Percent Error	C_D Percent Error	C_M Percent Error
1,868,831	-0.58%	0.86%	-0.96%
955,887	-0.72%	1.14%	-1.68%
360,463	-5.97%	33.60%	-9.13%

Table 5.3 Percent error in aerodynamic coefficients using 3 million element case as reference.

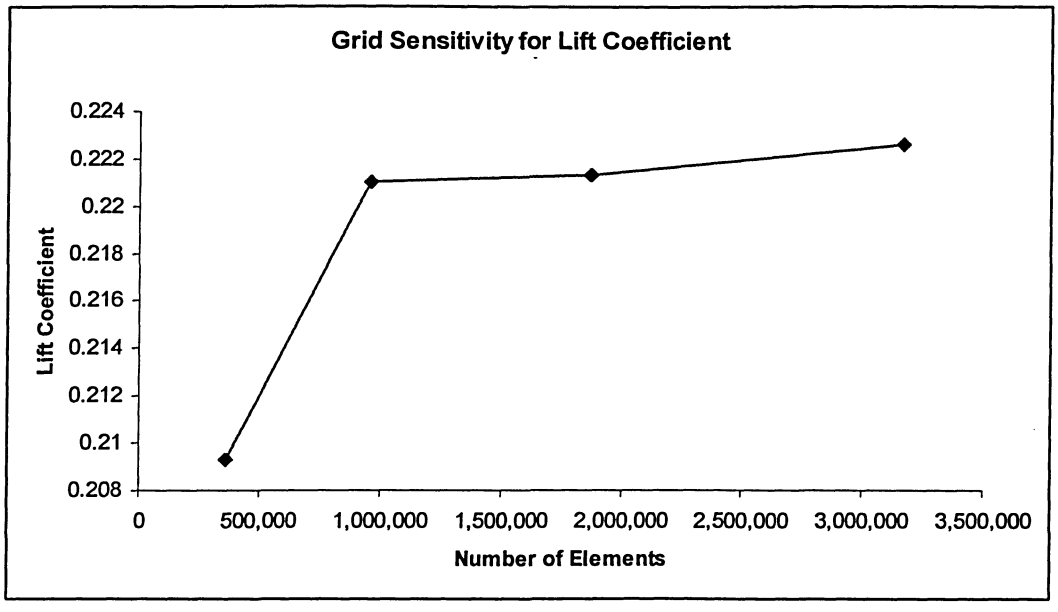

Figure 5.6 Grid sensitivity results for lift coefficient.

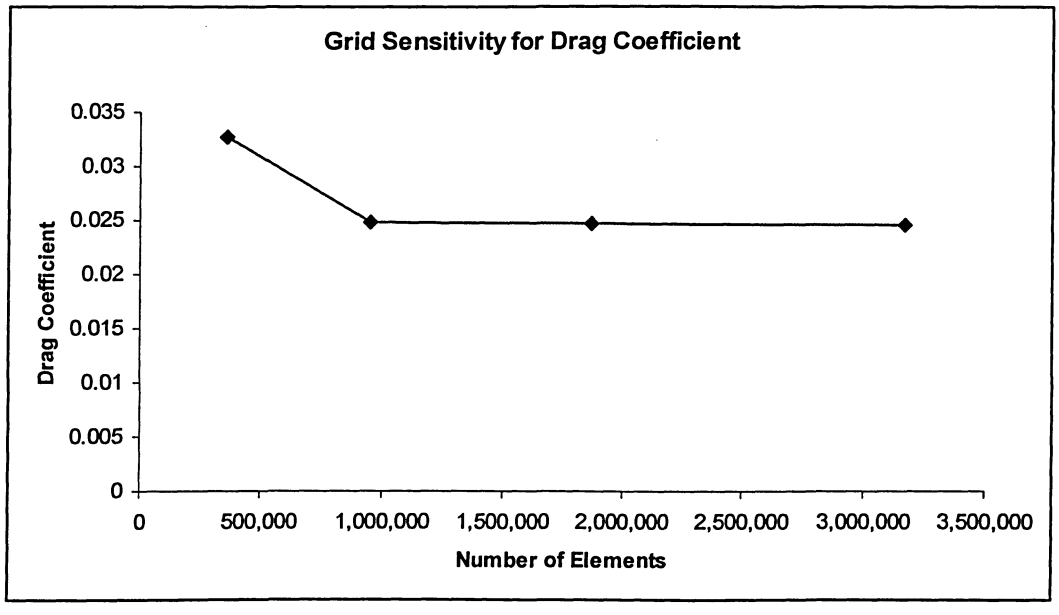

Figure 5.7 Grid sensitivity results for drag coefficient.

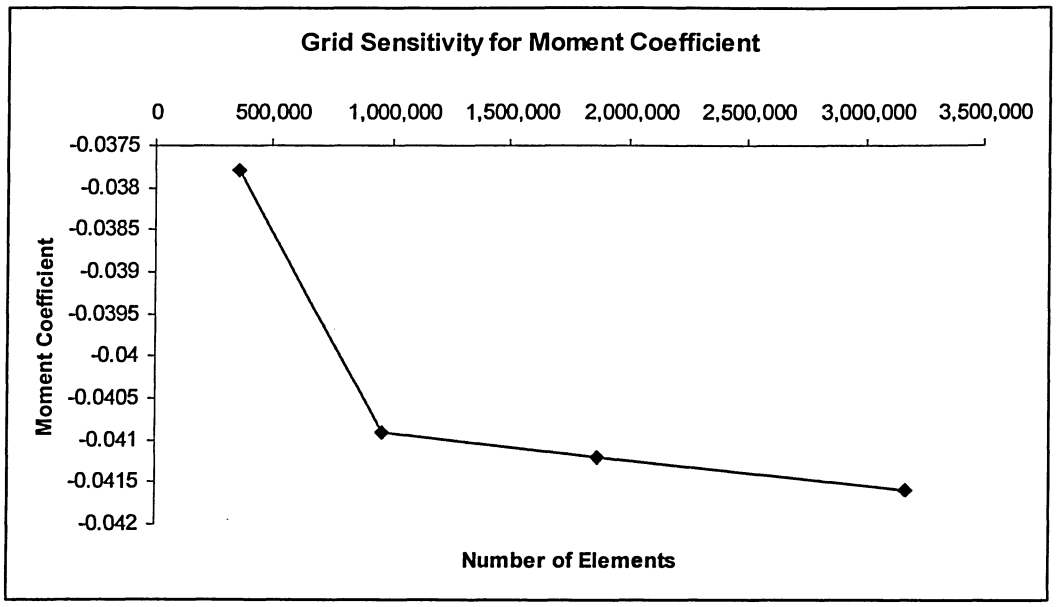

Figure 5.8 Grid sensitivity results for moment coefficient.

The results of the grid sensitivity study showed that the grids could be reduced from 3 million elements to 1 million elements with an average of 1.18% change in the aerodynamic coefficients. Reduction of the grid density below 1 million elements increased the error significantly. The reduction of the grid density from 3 million to 1 million elements reduced the run times from 1 week, using 4 processors on the HPCVL system, to 3 days to reach a converged solution.

5.4 Results and Discussion

In this section the results of this research are presented along with the flow effects around the elevon and their bearing on the hinge moments, as well as the implications to the design of the inboard elevon of the BWB.

5.4.1 Case Files

A total of nine different cases have been examined, and numerical results obtained. The file naming for these cases can be found in table 5.4. The naming scheme starts with the name of the aircraft, followed by the respective elevon deflection angle, then the direction of the deflection, the angle of the bevel modification and finally the type of modification.

Aircraft	Deflection Angle	Deflection	Modification Angle	Type of Modification
	0° or 5°	Positive, negative, or neutral	60° or 70°	Baseline or Beveled
bwb	00 05	pd nd ne	60 70	bl be

Table 5.4 File naming convention.

The first three cases are the baseline cases which have no modification applied to the trailing edge of the inboard elevon. These cases are used as a reference and comparison for the other six cases which have modifications to the trailing edge of the inboard elevon. These three cases consist of a neutral un-deflected geometry, bwb00nebl, a positive 5° deflected elevon, bwb05pdbl, and a negative 5° deflected elevon, bwb05ndbl.

The second three cases pertain to the first modification to the trailing edge, a 60° beveled trailing edge on the inboard elevon. These three cases consist of an un-deflected case, bwb00ne60be, a positive 5° deflected elevon, bwb05pd60be, and a negative 5° deflected elevon case, bwb05nd60be.

The final three cases are for the 70° beveled trailing edge modification of the inboard elevon. These three cases consist of an un-deflected case, bwb00ne70be, a positive 5° deflected elevon, bwb05pd70be, and finally a negative 5° deflected elevon case, bwb05nd70be.

The 60 and 70 degree bevels were chosen based on the results produced by Harrison [17] which studied various trailing edge modifications in 2D and found that beveled geometry within this range provided the largest improvement.

5.4.2 Aerodynamic Coefficient Results

In this section, the final results obtained from this research are presented in their respective non-dimensionalized coefficients. Equations 5.1 and 5.2 present the lift and drag coefficients for the total aircraft,

$$C_L = \frac{L}{\frac{1}{2}\rho_\infty V_\infty{}^2 S_{ref}} \tag{5.1}$$

$$C_D = \frac{D}{\frac{1}{2}\rho_\infty V_\infty{}^2 S_{ref}} \tag{5.2}$$

Reference Data:

Freestream Density:	0.02369 lb_m/ft^3
Freestream Velocity:	826.636 ft/sec
Reference Area:	6953.4 ft^2

In equation 5.1 and 5.2, ρ_∞ and V_∞ are the freestream density and freestream velocity respectively and their values are specified above. Also, in equations 5.1 and 5.2, the coefficients contain a reference area. For these coefficients, this reference area is the reference surface area of the BWB and is 6953.4 ft^2. The next equation, 5.3, is the pitching moment coefficient for the entire aircraft about the aerodynamic center.

$$C_M = \frac{M}{\frac{1}{2}\rho_\infty V_\infty{}^2 S_{ref} l_{ref}} \tag{5.3}$$

The new term, l_{ref} in equation 5.3 is reference chord length, equal to 1068.2 inches. The aerodynamic center is defined in x, y, and z Cartesian co-ordinates as follows.

Aerodynamic Center:

$$x_{ref} = 1172.20 \text{ in.}$$
$$y_{ref} = 435.60 \text{ in.}$$
$$z_{ref} = 0.00 \text{ in.}$$

The pitching moment given in equation 5.3 was calculated using the aerodynamic center data above. The hinge moment coefficient for the inboard elevon is defined in equation 5.4 given below.

$$C_H = \frac{M_H}{\frac{1}{2}\rho_\infty V_\infty{}^2 S_{ref} l_{ref}} \tag{5.4}$$

In equation 5.4, M_H is the hinge moment acting about the moment center of the hinge line. The reference area and reference length in equation 5.4 are the surface area of the elevon and the

reference chord of the elevon. The reference values and moment center for the elevon are presented below.

Reference Values:

$$S_{ref} = 197.46 \text{ sq. ft.}$$
$$l_{ref} = 185.85 \text{ in.}$$

Moment Center of Hinge Line:

$$x_{ref} = 1901 \text{ in.}$$
$$y_{ref} = 155 \text{ in.}$$
$$z_{ref} = 20 \text{ in.}$$

The final results for the un-deflected elevon, positive 5° deflected elevon, and the negative 5° deflected elevon are presented in table 5.5, 5.6 and 5.7 respectively.

Table 5.5 removed due to proprietary reasons described on page ii.

Table 5.5 Aerodynamic coefficients for un-deflected cases.

Table 5.6 removed due to proprietary reasons described on page ii.

Table 5.6 Aerodynamic coefficients for 5° positive deflected cases.

Table 5.7 removed due to proprietary reasons described on page ii.

Table 5.7 Aerodynamic coefficients for 5° negative deflected cases.

The results given in tables 5.5, 5.6 and 5.7 are presented in percent difference form using the baseline case as a reference. A negative percentage represents a reduction compared to the baseline, while a positive percentage represents an increase as compared to the baseline case. The results are tabulated in tables 5.8, 5.9 and 5.10 below.

	C_L	C_D	C_M	C_H
bwb00ne60be	-0.10%	0.84%	-1.26%	-7.34%
bwb00ne70be	-0.25%	0.00%	-2.52%	-15.60%

Table 5.8 Percent difference of the aerodynamic coefficients, using the baseline case as the reference value, for the un-deflected elevon.

	C_L	C_D	C_M	C_H
bwb05pd60be	-2.09 %	3.51 %	-6.93 %	-77.16 %
bwb05pd70be	-0.80 %	0.88 %	-3.03 %	-79.94 %

Table 5.9 Percent difference of the aerodynamic coefficients, using the baseline case as the reference value, for the positive deflected elevon.

	C_L	C_D	C_M	C_H
bwb05nd60be	-0.14 %	0.40 %	-0.73 %	-111.94 %
bwb05nd70be	0.36 %	0.40 %	-0.24 %	-88.06 %

Table 5.10 Percent difference of the aerodynamic coefficients, using the baseline case as the reference value, for the negative deflected elevon.

The results show that, for the un-deflected cases, table 5.8, the use of a beveled modification has very little effect, less than 1%, on the values of C_L, and C_D; however, this difference increases when examining the pitching moment. In the case of the hinge moments, there is a small affect as compared to the results in tables 5.9 and 5.10. The three un-deflected cases have no definitive trend as to which case would be the best. The ideal case would be to have an improvement in the aerodynamic coefficients or at the very least, no change over the baseline case, with a significant

reduction in the hinge moment. From table 5.8, the 70 degree bevel has the largest improvement in hinge moment; however, the 60 degree bevel has the least affect on aerodynamic performance.

In table 5.9, for the positive deflected cases, the use of the bevel at the trailing edge shows that although the changes are within 7% for the values of C_L, C_D, and C_M, the results are detrimental to the aerodynamic performance, i.e., there is a decrease in the lift coefficient, an increase in the drag coefficient and a decrease in the pitching moment coefficient. In the case of the hinge moment coefficient, table 5.9 clearly shows that the bevel has a significant effect on the hinge moment, with the 70 degree bevel providing approximately 80% reduction in the hinge moment. Table 5.9 shows that, for positive deflection, the 70 degree bevel provides the best solution as it has the smallest affect on the aerodynamic performance coupled with the largest reduction in hinge moment.

For the negative deflection cases, table 5.10, the results are far better with the bevel modification affecting the aerodynamic coefficients C_L, C_D, and C_M, by less than 1%. In the case of the 70 degree bevel, there is even a small improvement in the lift coefficient. Again, the 70 degree bevel shows the better performance gain of the two modifications, producing an 88% reduction in the hinge moment. In table 5.10, the 60 degree bevel produces 112% reduction in the hinge moment; however, this can be misleading. In the case of the 60 degree bevel, the hinge moment is completely reduced compared to the baseline, but is then increased in the opposite direction. The significance of this hinge moment reversal is discussed later in the chapter.

5.4.3 Baseline Un-deflected Results Comparison

For the baseline un-deflected geometry, two grids were built, a viscous model using a structured grid with a developed boundary layer region, and an inviscid model, built using an unstructured grid. The results for the viscous and inviscid model are compared with those obtained from Boeing for the un-deflected geometry in table 5.11. The values for C_D were not compared as the inviscid model only calculates the pressure drag and does not include the effects of viscous drag, and so would not provide an accurate comparison.

Table 5.11 removed due to proprietary reasons described on page ii.

Table 5.11 Comparison of aerodynamic coefficients for the un-deflected viscous and inviscid cases.

The viscous model built for this work agreed very closely with the results obtained by Boeing, with the value for C_M out by less than 4%, and no difference between the values of C_L. Comparing the inviscid and viscous result obtained from this work and the results are within 10% difference for C_L and C_M. The differences between the viscous and inviscid results are slightly larger than expected, as compared to the results obtained for the validation cases.

5.4.4 Trailing Edge Modification Flow Effects

In section 5.4.2, the results of the trailing edge modifications were compared to the baseline geometry. The results showed on average less than a 2% difference in the aerodynamic coefficients, C_L, C_D, and C_M, but an average 90% reduction in the hinge moment. These variations, and the phenomena involved, are discussed in this section.

In figures 5.9 and 5.10, plots of the surface pressure on the elevon at a spanwise location of 155 inches are shown, showing both the baseline negative deflection case and the 60° beveled trailing edge negative deflection case. In figure 5.9, there is a sudden decrease in surface pressure followed by a sudden spike, as the flow approaches the trailing edge. This is compared to figure 5.10 that shows a gradual increase in the surface pressure followed by a minor spike in the surface pressure at the end of the elevon.

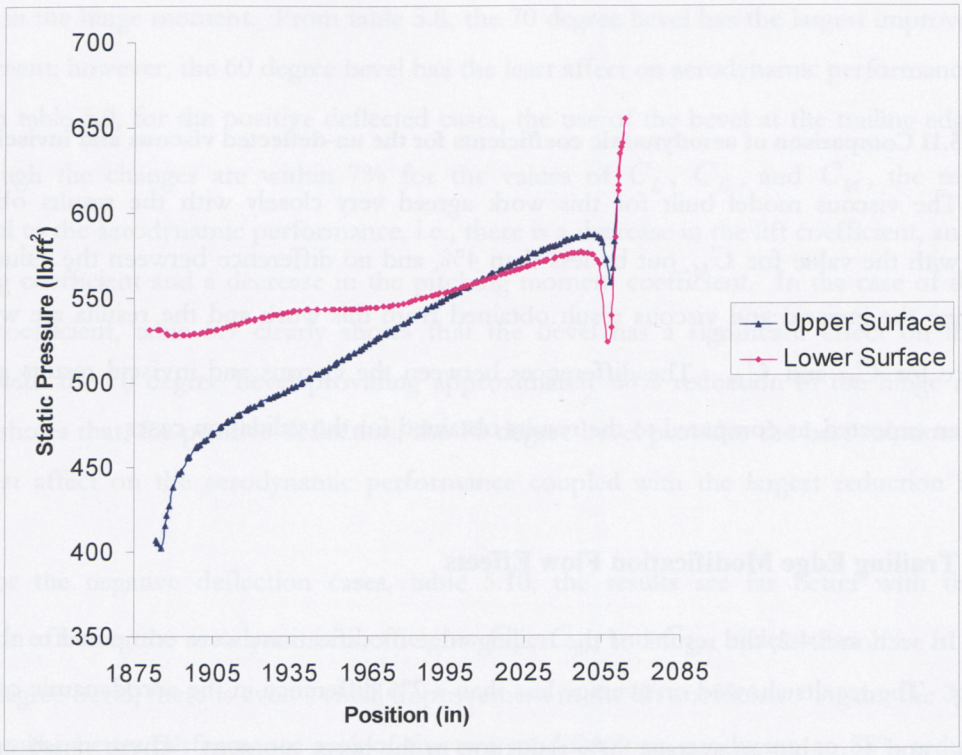

Figure 5.9 Static pressure plot on elevon surface for 60° beveled trailing edge, at a spanwise location of 155 inches, negative deflection case.

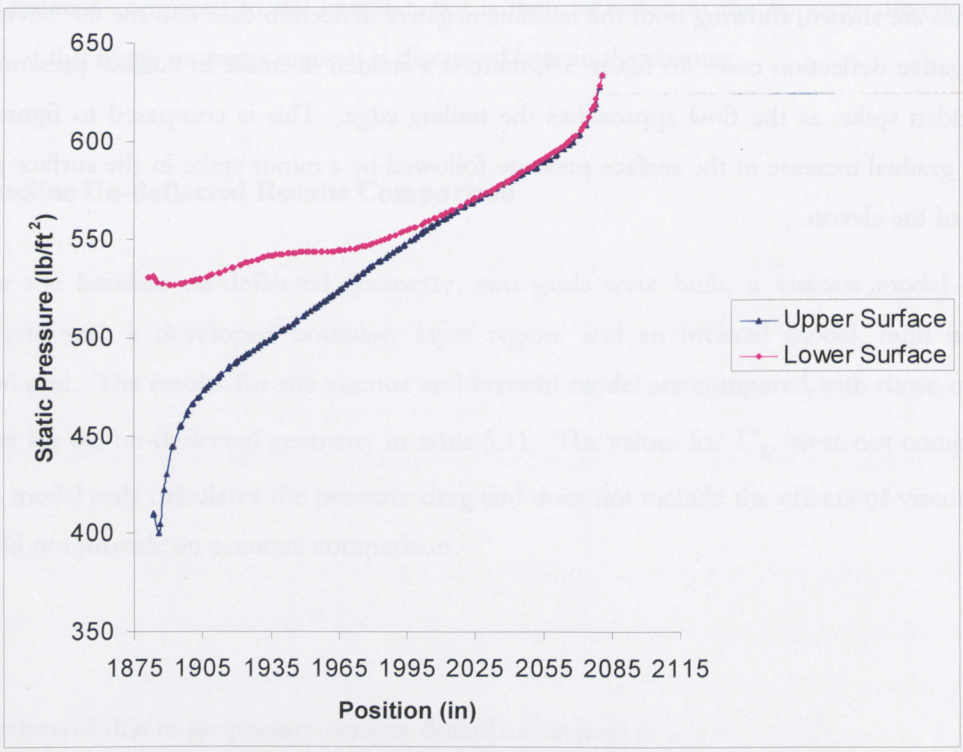

Figure 5.10 Plot of static pressure on elevon surface for baseline unmodified trailing edge, at a spanwise location of 155 inches, negative deflection case.

The flow effects in this region can be further displayed by plotting the velocity vectors in this region for both the 60° beveled edge modification and the unmodified trailing edge, as shown in figures 5.11 and 5.12.

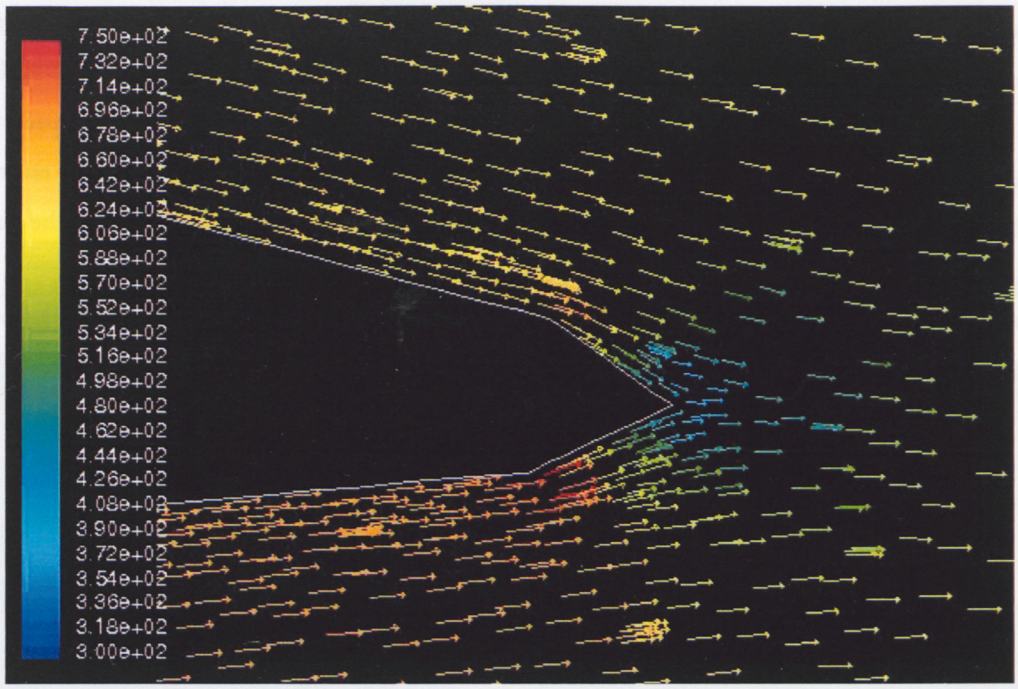

Figure 5.11 Velocity vectors over 60° beveled trailing edge at a spanwise location of 155 inches.

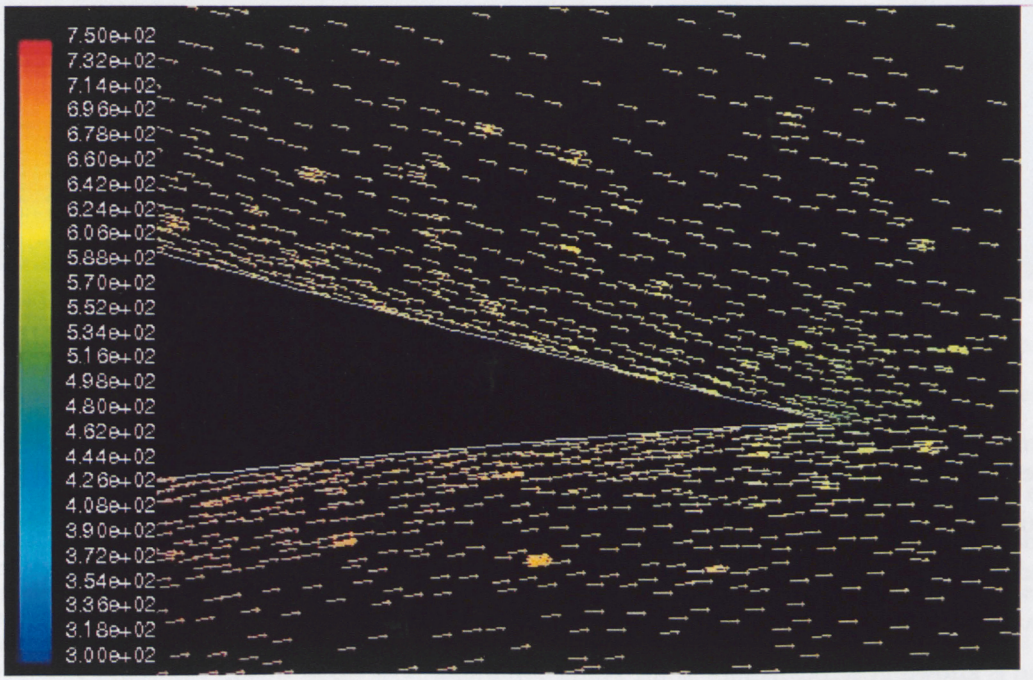

Figure 5.12 Velocity vectors over unmodified trailing edge at a spanwise location of 155 inches.

In figure 5.11, the velocity vectors show that the flow accelerates over the beveled edge, reaching speeds of approximately 700 ft/sec on the lower surface and approximately 650 ft/sec on the upper surface. This results in the drop in surface pressure as seen in figure 5.10. This flow then decelerates to approximately 350 ft/sec at the trailing edge which corresponds to the surface pressure spike in figure 5.10. In figure 5.12, the changes in velocity magnitude over the unmodified geometry are not as severe; approximately 600 ft/sec on the surface, slowing to 500 ft/sec at the trailing edge, and so there is only a gradual increase in the surface pressure followed by the small pressure spike shown in figure 5.10. This trend in pressure drop to pressure spike occurs across the entire surface of the beveled edge, as seen in figure 5.13. The surface pressure drop is shown by the dark green band with the high pressure region shown by the orange band near the trailing edge.

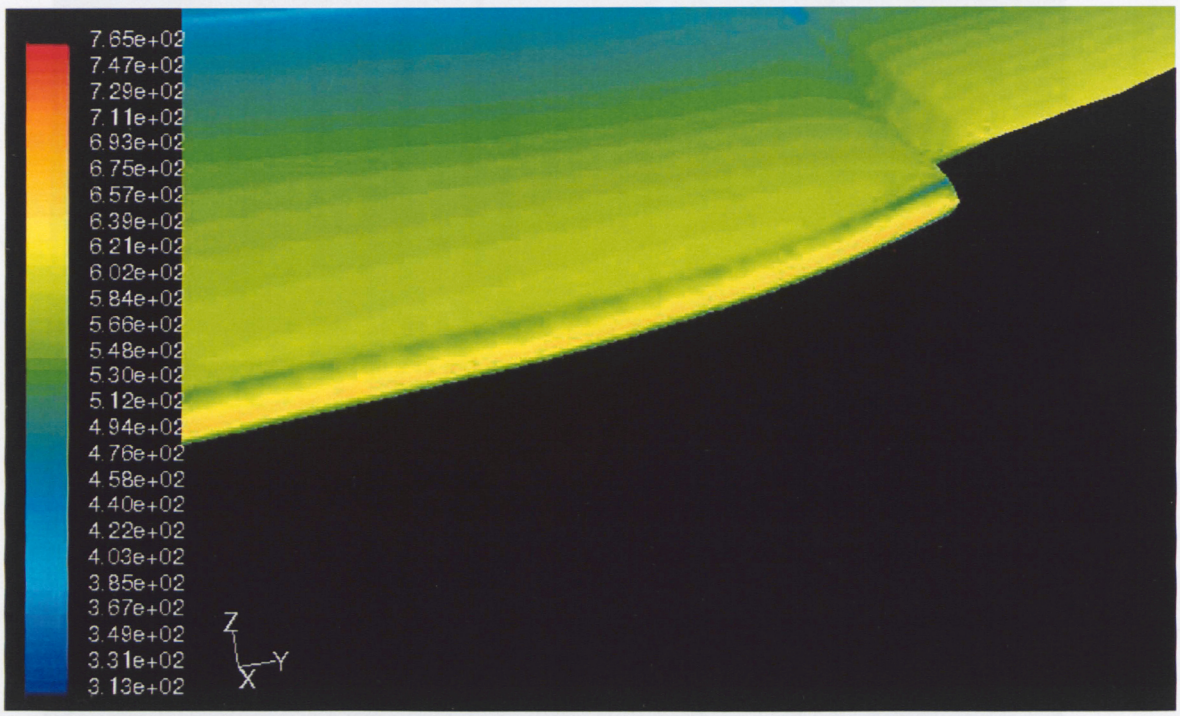

Figure 5.13 Surface pressure contours on trailing edge of 60° beveled trailing edge, negative 5° deflection.

The explanation of these phenomena is very simple. From figure 5.10 and 5.11, the drop in the pressure is clearly a result of the flow accelerating over the bevel and accelerating towards the trailing edge. The spike in the pressure at the trailing edge is the result of the flow having to suddenly change direction at the trailing edge, and the pressure force required to accomplish this causes the spike. This was first explained by the German mathematician M. Wilhelm Kutta in 1902 and is known in aerodynamics as the Kutta condition. The rapid change in surface pressure over the trailing edge modification is valid but has no bearing on the significant changes in the hinge moment.

The change in the hinge moment can be explained by examining the values of the pressure force acting on the elevon. The integral surface pressure forces acting on the elevon for the three negative deflection cases, as calculated by Fluent, are tabulated in table 5.12.

	Elevon Surface Pressure (lb/ft²)	% Difference
bwb05nd60be	241906	-7 %
bwbbl05nd	259316	NA
bwb05nd70be	246346	-5 %

Table 5.12 Comparison of elevon integral surface pressure for the baseline negative deflection case, 60° beveled trailing edge, and 70° beveled trailing edge, and the percent difference from the baseline case.

Table 5.12 shows that there is only a 7% difference in the surface pressure acting on the 60° beveled edge modification as compared to the baseline case, and only a 5% difference for the 70° beveled edge modification as compared to the baseline case. Yet this change in surface pressure results in a 112% and 88% reduction in the hinge moment for the 60° bevel and 70° bevel respectively. It is these losses in surface pressure at the trailing edge through the reduction in elevon surface area, coupled with the largest moment arm acting on the elevon, which result in the large change in the hinge moment.

One of the interesting features, from a design standpoint, found from this work is related to the hinge moments found for the negative deflection cases in table 5.7. The hinge moment, C_H, produced by the unmodified trailing edge during a negative deflection is a negative value. If, for the sake of this discussion, the elevon is considered to be an airfoil, then the negative hinge moment is the same as a negative pitching moment acting at the airfoil's leading edge. This negative moment causes the airfoil to pitch nose down. Returning to the elevon, this negative moment about the hinge line tends to resist the work done by the mechanism to deflect the elevon and return it to a stable position. This is a very important feature in a control surface, as this would tend to return the aircraft to a steady stable flight condition in the event of a failure in the mechanism used to deflect the elevon surface. In the case of the 60° beveled edge modification, the resultant hinge moment, although small, is a positive moment. Following the above thought process, this would cause a nose up pitch or, in the case of the elevon, would increase the deflection of the elevon. From a stability and control standpoint, these are not ideal conditions, as in the event of a control failure the elevon would continue to deflect, causing an increase in the nose down pitch of the aircraft. For the 70° beveled edge modification, the resulting hinge moment when the elevon is deflected 5° negative is a small negative hinge moment, which is the ideal case. The resulting hinge moments produced by the

beveled trailing edge modification in this work are small moments as compared to the baseline values. They may not seem significant, but the trend shows that more investigation is required to see if there is the possibility of hinge moment reversal at larger bevel angles, as well as various elevon deflection angles and aircraft angles of attack. If there are, this could pose a significant problem for engineers from a stability and control standpoint.

Chapter 6

Conclusions and Recommendations

6.1 Introduction

The work presented in this document is the culmination of computational research investigating the effects of beveled trailing edge modifications on the inboard elevon of a BWB aircraft. The BWB is a unique aircraft that has unique control requirements. The loss of the tail as compared to a conventional aircraft reduces the main moment arm used in the control of an aircraft's pitching moment. The solution is a larger than normal control surface which requires large rapid deflections. This large surface, combined with a short moment arm, puts large requirements on the elevon and resultant mechanism required to deflect it. The results of this work showed that, through the use of a beveled trailing edge, the hinge moment could be greatly reduced without adverse affects on the pitching moment and lift coefficient of the aircraft. The conclusions based on the results of this research are presented in section 6.2, followed by possible future research areas in section 6.3.

6.2 Conclusions

Conclusion 1:

A validation case was performed on a NACA 0012 airfoil with a 60° split flap. This case was used because it was similar to that of the current research investigating a deflected control

surface. The case used an unstructured grid and was run using Fluent's implicit coupled solver with an inviscid first order method. The values of C_L agreed within 10% for all angles of attack, and the values of C_M found agreed within 10% between ±8° angle of attack; however, the C_M values diverged at ±12° resulting in over 20% error. These results showed that the methodology used for this work is valid for determining C_L and C_M for the BWB at small angles of attack.

Conclusion 2:

The grid sensitivity work performed showed that the initial grid that used 3 million elements could be reduced to 1 million elements with less than a 2% loss in the solution accuracy. This allowed the reduction of computational run times from 1 week to 3 days.

Conclusion 3:

Due to geometric complexities around the deflected elevon, a fully structured grid capable of modeling viscous effects in the boundary layer region was only produced for the unmodified, un-deflected geometry. For the other cases, a fully unstructured grid was used.

Conclusion 4:

The results showed a sudden drop in surface pressure, followed by a spike in the pressure at the trailing edge for the modified geometries. These pressure changes are a result of the flow at the surface of the wing accelerating over the airfoil at the bevel and then decelerating at the trailing edge.

Conclusion 5:

The resultant changes in surface pressures were 5% and 7% for the negative deflected elevon with a 60° and 70° beveled geometry respectively, compared to the baseline case. This change in pressure force is due to the loss of elevon surface area at the trailing edge in the modified cases.

Conclusion 6:

The use of beveled trailing edges resulted in a maximum 112% reduction in the hinge moment for the negative deflection, a maximum of 77% reduction for the positive deflection case and finally a maximum of 16% reduction for the un-deflected cases. There was an average of 2% change in the aerodynamic performance of the aircraft with the use of the modifications.

Conclusion 7:

Of the two modifications investigated, based on the results obtained, the 70° beveled edge modification showed the best potential because of the stability and control characteristics of the moment values obtained and the resultant affects on the aerodynamic performance on the aircraft.

Conclusion 8:

Although drag results were presented in this work, the actual values obtained are in error by an order of magnitude as a result of running only inviscid solutions. The drag values obtained were presented in this work since all cases were run using the same inviscid model and used for strictly as a comparison between models in this work.

The current research shows that the flow occurring at the trailing edge of a control surface can greatly affect the hinge moments acting on the control surface without adverse affects on the complete aircraft's lift coefficient and pitching moment.

6.3 Future Research

Further development is required in the area of three-dimensional grid generation capable of modeling the viscous effects within the boundary layer, around complex geometries such as the one encountered in this research. Research conducted by NASA [36] investigated the use of unstructured grids on a high speed research vehicle with viscous effects included. The model had deflected control surfaces as in this research. However, the grid software used in the research was capable of building the grid outwards from the unstructured grid using what is called advancing front and

advancing layer methods (AFM and ALM). Most current unstructured grid methods use an advancing front method to produce their grids; however, through the combination of the advancing layer methods, thin layer viscous grid regions can be created. In these methods, individual grid layers are produced as the grid solver marches away from the surface [37]. The use of these methods with prismatic tetrahedral grid generation would allow for the creation of resolved boundary layer grids while also maintaining the advantages of unstructured grid generation. AFM/ALM methods have been used in several other research projects investigating turbulent flows and flows around flap systems [39, and 40]. Gridgen has the capability to produce extruded grids similar in method to the ALM method but is not as advanced as the methods in references [36, 37, 38, and 39]

Although modern computing power has allowed CFD engineers to create and run full 3D models, design optimization through an iterative process on realistic high Reynolds number flows is still limited by the time requirements for computational runtimes and grid generation. Currently, research is being performed investigating the accuracy of code developed to optimize airfoil geometry in 2D [40]. In reference [40] a Newton-Krylov algorithm is used to optimize the gap between an airfoil and flap. There is the possibility that this research could be applied to the trailing edge modification used in this work to find an optimized design in two dimensions and then build a 3D model based on the 2D research to see if the results agree. This could vastly cut down the work time by eliminating the need to build complex 3D grids for multiple beveled edge designs.

For the 60 degree bevel, the hinge moment calculated was a small positive value which caused a reversal of the hinge moment acting on the elevon. Although small, it does raise the possibility of larger hinge moment reversal values at increased bevels and various flight conditions. This could be problematic in terms of the stability and control of the aircraft and should be investigated further.

Appendix A

```
*********************************************
*       Code to take x, y, and z            *
*       Co-ordinate data and produce        *
*       A data file that is read by Gambit  *
*       To produce splined geometry         *
*                                           *
*       Written by: Sharman Perera and      *
*       Alexander Jackson                   *
*                                           *
*********************************************


#include <stdio.h>

main()
{
  double xval, yval, zval;
  int count=0, i, start, coord, j, k;

  printf("identifier name \"wingcomp\" new \n");
  printf("import iceminput \"/home/fluids/ajackson/thesis/bwb.data\"
vertex \n ");

  while((scanf(" %lf", &xval))!=EOF)
    {
      count=count+1;
      scanf(" %lf", &yval);
      scanf(" %lf", &zval);
    }
  printf("save\n");

  start=1;
  for (i=1; i<=28; i++){
    coord=start;
    for (k=1; k<=2; k++){
      printf("edge create nurbs ");
      if (k==2){
```

```
      coord=coord-1;
      }
      for (j=1; j<=57; j++){
      printf("\"vertex.%d\" ", coord);
      coord++;
      }
      printf("\n");
    }
    start=start+113;
  }
  printf("save\n");
}
```

Appendix B

Simulation Boundary Conditions

Mach number: 0.85

Altitude: 35,000 ft

Gauge Pressure: 497.956 lb/ft^2

Temperature: 393.854 $^\circ$R

Angle of Attack α : 3.75°

X-component of flow direction: 0.9978589

Y-component of flow direction: 0

Z-component of flow direction: 0.0654031

References

1.) PBS, "Chasing The Sun, Planes", http://www.pbs.org/kcet/chasingthesun/planes/wrightfly_1_po.html (2003)

2.) "List of Aircraft Used During The Vietnam War, B-47", http://www.farfromglory.com/b47.htm (2003)

3.) Boeing, "Image Center, 777", http://www.boeing.com/companyoffices/gallery/images/commercial/777200-01.html (2003)

4.) Bourges, F., "Jet Art, USAF, B2", http://kovy.free.fr/pages/planche7.html (2003)

5.) http://www2s.biglobe.ne.jp/~FlyWing/FlyingWing_Others.html (2003)

6.) AerospaceWeb.org "AerospaceWeb YB-49", http://www.aerospaceweb.org/aircraft/bomber/yb49/ (2003)

7.) Liebeck, R.H., "Design Of The Blended-Wing-Body Subsonic Transport", 2002 Wright Brothers Lecture, AIAA-2002-0002, 2002.

8.) Raymer, Daniel, P., "Aircraft Design: A Conceptual Approach Third Edition", American Institute of Aeronautics and Astronautics, 1999.

9.) Roman, D., Allen, J. B., Liebeck, R. H., "Aerodynamic Design Challenges Of The Blended-Wing-Body Subsonic Transport", AIAA-2000-4335, 2000.

10.) Roman, D., Gilmore, Richard, Wakayama, Sean, "Aerodynamics Of High-Subsonic Blended-Wing-Body Configurations", AIAA-2003-0554, 2003.

11.) Cameron, Douglas, Princen, Norman, "Control Allocation Challenges And Requirements For The Blended Wing Body", AIAA Guidance, Navigation, and Control Conference and Exhibit, August 2000, AIAA-2000-4539, 2000.

12.) Roman, D., "BWB Actuation Power", Internal Boeing Slide Presentation, April 13th 1999.

13.) Jones, Robert T., Ames, Milton B. Jr., "Wind-Tunnel Investigation of Control-Surface Characteristics, The Use of a Beveled Trailing Edge To Reduce The Hinge Moment of a Control Surface", NACA L-464, March 1942.

14.) Toll, Thomas A., "Summary of Lateral-Control Research", NACA Report No. 868, 1947.

15.) Phillips, William H., "Appreciation and Prediction of Flying Qualities", NACA Report No. 927, 1949.

16.) Sadoff, M., Matteson, Fredrick H., Van Dyke, Rudolph D. Jr., "The Effect of Blunt-Trailing-Edge Modifications on the High-Speed Stability and Control Characteristics of a Swept-Wing Fighter Airplane", NACA RM A54C31, May 26, 1954.

17.) Harrison, N., "Blended Wing Body Trailing Edge Device Design To Reduce Hinge Moment", Thesis Report, Ryerson University, April 6th 2000.

18.) Roman, D., "Trailing Edge Shaping to Reduce Device Hinge Moments", Internal Boeing Research Document, 2000.

19.) Perera, S., "Effect of a slat arm door on the wing efficiency of a commercial aircraft.", Ryerson University, Toronto, 2004

20.) Weatherill, N.P., "Grid Generation: Structured, Unstructured Or Both?", Computational Methods In Aeronautical Fluid Dynamics, Oxford Science Publications, 1990.

21.) Anderson, John D. Jr, "Computational Fluid Dynamics, The Basics with Applications", McGraw-Hill, New York, 1995.

22.) Gridgen User Manual Version 15, 2003.

23.) Vinokur, M., "On One-Dimensional Stretching Functions for Finite-Difference Calculations", NASA CR 3313, 1980.

24.) Spalart, P. R., Allmaras, S. R., "A One-Equation Turbulence Model For Aerodynamic Flows", AIAA paper 92-0439, 1992.

25.) Jones, B., "Viscous Grid Spacing Calculator", http://geolab.larc.nasa.gov/APPS/YPlus/ (2002)

26.) Tannehill, John C., Anderson, Dale A., Pletcher, Richard H., "Computational Fluid Mechanics and Heat Transfer Second Edition", Hemisphere Publishing, 1997.

27.) Thomas, P. D., Middlecoff, J. F., "Direct Control of the Grid Point Distribution in Meshes Generated by Elliptic Equations", AIAA 79-1462R, 1979.

28.) Thompson, Joe F., Thames, Frank C., Mastin, C. Wayne, "Boundary-Fitted Curvilinear Coordinate Systems for Solution of Partial Differential Equations on Fields Containing Any Number of Arbitrary Two-Dimensional Bodies" NASA CR-2729, July 1977.

29.) Hilgenstock, A., "A Fast Method For The Elliptic Generation Of Three-Dimensional Grids With Full Boundary Control" Numerical Grid Generation in Computational Fluid Mechanics 1988, ed. by Sengupta, S., et al, Pineridge Press Ltd., Swansea, UK, 1988, pp. 137-146.

30.) Tarhan, Erhan, Oktay, Erdal, Kaavsaoglu, Mehmet S., "Solution of Airfoil-Flap Configurations By Using Chimera Grid System", ICAS 2002 Congress, 2002.

31.) NASA Glen Research Center, http://www.grc.nasa.gov/WWW/wind/valid/nlrflap/grid.jpg

32.) Fluent 6.0 User Manual, 2001.

33.) Versteeg, H. K., Malalasekera, W., "An introduction to Computational Fluid Dynamics, The Finite Volume Method", Pearson Education Limited, England, 1995.

34.) Anderson, John D. Jr, "Fundamentals of Aerodynamics, Second Edition", McGraw-Hill, New York, 1991.

35.) Abbott, Ira H., "Theory of Wing Sections", Dover Publications Inc., New York, 1959.

36.) Ghaffari, Farhad, "Unstructured Grid Viscous Flow Simulation Over High-Speed Research Technology Concept Airplane at High-Lift Condtions", Langley Research Center, NASA/TP-1999-209718, November 1999.

37.) Frink, Neal T., Pirzadeh, Shahyar, Paresh, Parikh, "An Unstructured-Grid Software System For Solving Complex Aerodynamic Problems", Langley Research Center, NASA CP-3291, May 1995.

38.) Mathias, Donovan L., Roth, Karlin R., Ross, James C., Rogers, Stuart E., Cummings, Russell M., "Navier-Stokes Analysis of the Flow About a Flap Edge", Journal of Aircraft, Vol. 35, No. 6, November-December 1998.

39.) Frink, N. T., "Assessment of an Unstructured-Grid Method for Predicting 3-D Turbulent Viscous Flows", Langley Research Center, AIAA 96-0292, 1996.

40.) Nemec, M., Zingg, D. W., "A Newton-Krylov Algorithm for Complex Aerodynamic Design", 10th Annual Conference of the CFD Society of Canada, Conference Proceedings, June 2002.